NOTICE

The quality of this microform is heavily dependent upon the quality of the original thesis submitted for microfilming. Every effort has been made to ensure the highest quality of reproduction possible.

If pages are missing, contact the university which granted the degree.

Some pages may have indistinct print especially if the original pages were typed with a poor typewriter ribbon or if the university sent us an inferior photocopy.

Reproduction in full or in part of this microform is governed by the Canadian Copyright Act, R.S.C. 1970, c. C-30, and subsequent amendments.

AVIS

La qualité de cette microforme dépend grandement de la qualité de la thèse soumise au microfilmage. Nous avons tout fait pour assurer une qualité supérieure de reproduction.

S'il manque des pages, veuillez communiquer avec l'université qui a conféré le grade.

La qualité d'impression de certaines pages peut laisser à désirer, surtout si les pages originales ont été dactylographiées à l'aide d'un ruban usé ou si l'université nous a fait parvenir une photocopie de qualité inférieure.

La reproduction, même partielle, de cette microforme est soumise à la Loi canadienne sur le droit d'auteur, SRC 1970, c. C-30, et ses amendements subséquents.

ISBN 0-315-53843-0

FLUX CUTTING in SEMI-REVERSIBLE and IRREVERSIBLE TYPE II SUPERCONDUCTORS

A thesis presented to the University of Ottawa
in partial fulfillment of the requirements
for the degree of Master of Physics

John Sekerka
DEPARTMENT of PHYSICS, UNIVERSITY of OTTAWA
Ottawa, Ontario, Canada

ACKNOWLEDGEMENTS

I would like to express my gratitude to Dr. Marcel A. R. LeBlanc for his invaluable guidance, supervision, encouragement and inspiration provided throughout the stages of this project.

I would also like to thank the various members of the department, the professors, the support staff and especially the graduate students who made my tenure most enjoyable educationally and socially.

And finally I would like to thank my family.

ABSTRACT

Through extensive magnetization measurements the similarities and differences in the magnetic behaviour of a pair of type II superconductors, have been thoroughly delineated. A weak pinning (semi reversible) $PbIn$ specimen, exhibiting a partial Meissner effect, and an irreversible (with modest pinning) $PbBi$ specimen showing no Meissner effect, were studied. The samples were in the form of thin disks.

The evolution of the components of the magnetic moment of these rotating disk specimens was continuously monitored parallel and perpendicular to the applied magnetic field H_a, yielding curves of the magnetization $< M_x >$ and $< M_y >$ versus the angle of rotation θ. The samples were rotated about a central axis and bathed in various static magnetic fields directed parallel to the flat surfaces.

These rotational magnetization curves were analyzed using a phenomenological model developed by Clem, and also exploiting a modified version of an empirical model proposed by Boyer. The two approaches generated very similar behaviour, in good agreement with our observations. Reasons for this close correspondence between the theoretical predictions are identified.

A vast array of theoretical $< M_x >$ and $< M_y >$ vs θ curves were computed. The ratio of the critical current densities for flux cutting and depinning $j_{c//}$ / $j_{c\perp}$, was varied over a wide range. For each ratio, the predicted behaviour was investigated

for various H_a/H_*, where H_* is a parameter characterizing the pinning strength of a sample. In this theoretical survey, both the Bean and Kim approximations were introduced since these expressions constitute limits which bracket the spectrum of plausible dependence of j_c on the flux density B. Due to constraints of computing power and for economy of time, these calculations were performed using our model.

A comparison of the compilation of these theoretical results with our data confirm that the basic physical picture is correct. It is estimated that $j_{c//} \leq j_{c\perp}$ for the $PbIn$, and $j_{c//} \approx 2j_{c\perp}$ for the $PbBi$ sample. Both samples exhibit a dependence of j_c on B closer to the Bean than to the Kim expressions.

The flux cutting process is described macroscopically and the Clem phenomenological model is summarized. The crucial feature at the root of the phenomena, is the appearance and growth of a valley in the profile of the magnetic flux density as the rotation progresses. The Clem framework 'automatically' generates such a valley, thereby confirming its existence previously postulated on empirical grounds by Boyer.

As an addendum, a sampling of a large collection of related experimental observations is also presented. Here flux lines of a fixed orientation enter or leave a disk specimen which is permeated by a lattice of straight parallel flux lines, initially pointing along some direction θ with respect to the invading (or emigrating) magnetic flux.

Table of Contents

1 INTRODUCTION 1

1.1 Background 1

1.2 Framework of the Investigation 5

1.3 The Project 6

1.3.1 Choice of Materials 7

1.3.2 Choice of Method 8

2 EXPERIMENTAL SET UP 10

2.1 Introduction 10

2.2 Experimental Set up 13

2.2.1 Samples Employed 13

2.2.2 Sample Disk Assembly 14

2.2.3 Pickup Coil Assembly 16

2.2.4 Superconducting Solenoid 19

2.2.5 Calibration 20

3 STANDARD MAGNETIZATION CURVES 22

3.1 Introduction 22

3.2 Reversible Magnetic Behaviour 22

3.3 Irreversible Magnetic Behaviour 24
3.4 Parameters Classifying Irreversible Behaviour 26
3.5 The Meissner Effect 33
3.6 Experimental Results 35
3.6.1 Major Hysteris Curves 35
3.6.2 Catalogue of Standard Magnetization Curves 36

4 MAGNETIZATION CURVES OF ROTATING DISKS 41
4.1 Introduction 41
4.2 Description of the Observations 42
4.3 General Remarks 44
4.4 Graphical Compilation of the Observations 45

5 THEORETICAL ANALYSIS OF THE ROTATING DISK 54
5.1 Introduction 54
5.2 General Background 54
5.3 The Boyer Model 56
5.4 Flux Line Cutting 58
5.5 Evolution of the Boyer Valley 62
5.6 Our Ansatz 67
5.7 The Clem Phenomenological Model 68
5.8 Application of the Clem Model 70
5.9 Boyer Valley in the Clem Model 71
5.10 Comparison of the Models 73
5.11 Catalogue of Theoretical Curves 75
5.12 $< M_y >$ and $< M_z >$ from B(x) and α(x) Profiles 80

5.13 Theoretical H_* 81
5.14 Closing Remarks on the Theoretical Curves 83

6 INTERACTION OF TILTED FLUX LINES 87
6.1 Introduction 87
6.2 Framework of the Investigation 88
6.3 Comments on the Observations 90

List of Figures

1 Geometry of current densities. 11

2 Sample disk assembly. 15

3 Pickup coil assembly. 18

4 Schematic of the experimental set up. 19

5 Characteristic Magnetization Curves, for a semi-reversible sample. . 25

6 Characteristic Magnetization Curves, for an irreversible sample. . . . 25

7 Magnetization profiles across the width of the specimen. 27

8 Magnetization profiles (as pinning strength increases). 34

9 *PbIn* Magnetization Curves. 37

10 *PbBi* Magnetization Curves. 37

11 $T = 4.2\,K$, *PbBi* Magnetization Curves. 39

12 Annealed *PbBi*: Magnetization Curves. 39

13 $T < 4.2\,K$, *PbBi* Magnetization Curves. 40

14 *PbIn* Rotational Curves, for $H_a/H_* = 0.5$. 47

15 *PbIn* Rotational Curves, for $H_a/H_* = 1.0$. 47

16 *PbIn* Rotational Curves, for $H_a/H_* = 2.0$. 48

17 *PbBi* Rotational Curves, for $H_a/H_* = 0.5$. 48

18 *PbBi* Rotational Curves, for $H_a/H_* = 1.0$. 49

19 *PbBi* Rotational Curves, for $H_a/H_* = 2.0$. 49
20 *PbBi* ($T < 4.2\,K$) Rotational Curves, for $H_a/H_* = 0.5$. 50
21 *PbBi* ($T < 4.2\,K$) Rotational Curves, for $H_a/H_* = 1.0$. 50
22 *PbBi* ($T < 4.2\,K$) Rotational Curves, for $H_a/H_* = 2.0$. 51
23 Annealed *PbBi* Rotational Curves, for $H_a/H_* = 0.5$. 51
24 Annealed *PbBi* Rotational Curves, for $H_a/H_* = 1.0$. 52
25 Annealed *PbBi* Rotational Curves, for $H_a/H_* = 2.0$. 52
26 Maximum magnetization signal for *PbBi* and *PbIn*. 53
27 Angle of maximum magnetization signal for *PbBi* and *PbIn*. 53
28 Magnetic flux density profiles, $B_a < B_*$. 56
29 Magnetic flux density profiles, $B_a > B_*$. 57
30 Flux cutting sequence 59
31 Geometry of Parameters. 63
32 Evolution of $B, \alpha, E_{//}$ and $E_\perp$ profiles. 64
33 Model Comparison for $H_a/H_* = 0.5$ and $\gamma = 5$. 73
34 Model Comparison for $H_a/H_* = 1.0$ and $\gamma = 5$. 74
35 Model Comparison for $H_a/H_* = 2.0$ and $\gamma = 5$. 74
36 Rotational Curves for $H_a/H_* = 0.5$, $\gamma = 2.0$: Bean Approximation . 77
37 Rotational Curves for $H_a/H_* = 0.5$, $\gamma = 2.0$: Kim Approximation . 77
38 Rotational Curves for $H_a/H_* = 1.0$, $\gamma = 2.0$: Bean Approximation . 78
39 Rotational Curves for $H_a/H_* = 1.0$, $\gamma = 2.0$: Kim Approximation . 78
40 Rotational Curves for $H_a/H_* = 2.0$, $\gamma = 2.0$: Bean Approximation . 79
41 Rotational Curves for $H_a/H_* = 2.0$, $\gamma = 2.0$: Kim Approximation . 79
42 Maximum Magnetization Curves: the Bean Approximation. 84
43 Maximum Magnetization Curves: the Kim Approximation. 84

44 Angle of Maximum Magnetization: the Bean Approximation. 85
45 Angle of Maximum Magnetization: the Kim Approximation. 85
46 Flux line behaviour. 89
47 Trapped flux half cycle compilation curve for $PbBi$. 91
48 Selected individual case for $PbBi$. 91
49 Selected individual case for $PbBi$. 92
50 Trapped flux half cycle compilation curve for $PbIn$. 92
51 Selected individual case for $PbIn$. 93
52 Selected individual case for $PbIn$. 93
53 Trapped flux full cycle compilation curve for $PbBi$. 94
54 Selected individual case for $PbBi$. 94
55 Selected individual case for $PbBi$. 95
56 Trapped flux full cycle compilation curve for $PbIn$. 95
57 Selected individual case for $PbIn$. 96
58 Selected individual case for $PbIn$. 96

Chapter 1

INTRODUCTION

1.1 Background

The critical current density $j_{c\perp}$, for depinning of quantized flux lines in type II superconductors can be determined using the standard four probe technique. In this approach, a transport or conduction current fed through the sample via external leads from a 'power' supply is increased steadily until a voltage is detected along the specimen. The appearance of the latter is monitored by means of two separate leads attached to the sample and connected to a sensitive D.C. voltmeter. Several precautions are mandatory to ensure reliable readings. This method also presents certain inherent problems. Ohmic (joule) heating at the contacts between the current leads and the superconductor cannot be avoided and must be minimized. This contact heating becomes particularly troublesome in the range of low magnetic fields where the critical current I_c grows to considerable values. Indeed for a 'bulk' specimen of a strong pinning material, the critical current can attain levels from several hundred to a few thousand amperes [9].

For example, a 0.025 cm diameter wire of $NbTi$ at 4.2 K can carry about 800 Amps before any resistivity appears in the absence of an externally applied magnetic field. Power supplies capable of providing such large ripple-free and stable currents are quite expensive, hence not generally available. Even when these are available, the rapid consumption of liquid helium arising when such large currents are fed into a helium bath becomes an important consideration.

The critical current $I_{c//}$ for the onset of flux cutting can also be determined using the four probe arrangement. The two cases differ in that the externally applied magnetic field $\vec{H}_a$ is directed transverse to the conduction current when the focus is on $j_{c\perp}$, but is directed along the current flow for measurement of $I_{c//}$, hence $j_{c//}$. The problems just mentioned (contact heating, large current sources, rate of helium evaporation) are now magnified since generally $I_{c//} \gg I_{c\perp}$.

The procedure for extracting the dependence of $j_{c//}$ on the magnetic flux density B from the measurements of $I_{c//}$ vs H_a becomes progressively more complicated in the range of small H_a/H_{c2}. The difficulty here arises for two reasons. Firstly, the magnetic field H_I generated by the conduction current is perpendicular to I, hence perpendicular to $\vec{H}_a$ when the latter is oriented along $I_{c//}$. Thus the total magnetic field and the resultant magnetic flux density are not exactly directed along $I_{c//}$. In fact, the angle subtended by the total magnetic field $\vec{H}_t = \vec{H}_a + \vec{H}_I$ and the axis of current flow increases as H_a is made small and I_c becomes very large. Secondly, the configuration of current flow in these circumstances is fascinating but far from simple. Various observations show that the conduction current does not stream along the wire or ribbon sample, but adopts a spinning or circulating pattern, *i.e.* as I is impressed, a persistent azimuthally flowing component arises 'spontaneously' [32] – [34], [48] – [51]. By Maxwell's equation $\nabla \times \vec{H} = \vec{j}$, this

azimuthally circulating persistent current generates a magnetic field $\Delta H'$ which is directed along I, hence along H_a. As a consequence, the magnetic field along H_a inside the sample is modified by $\Delta H'$. The magnitude of this 'internal' contribution relative to the externally applied magnetic flux density can be quite significant [32] – [34]. In fact in the low field range of some materials, $\Delta H'$ has been observed to appreciably exceed H_a. Although most intriguing, this feature makes the analysis of $I_{c//}$ vs H_a data in terms of $j_{c//}$ vs B, a more difficult task than initially anticipated.

Many of the technical difficulties encountered in using the four probe technique to determine I_c vs H_a parallel and transverse, can be circumvented by exploiting magnetic measurements [9], [19], [21], [23], [24], [31], [35] – [38], [47], [52]. Further, this last method provides information on the magnetic response of the superconducting material to various changes of the applied magnetic field. In this approach, the evolution of the magnetic moment of the specimen is monitored as H_a and/or as the temperature T are varied. The magnetic moment can be determined, *(i)* using pick up coils in vibrating sample magnetometers, SQUID magnetometers and with integrating operational amplifiers, or *(ii)* mechanically using torque magnetometers and Gouy type balance magnetometers.

Since the magnetic moment of non-magnetic type II superconductors is due to macroscopic persistent currents flowing in the specimen, these data can be analyzed to yield $j_{c\perp}$ and $j_{c//}$ versus B. In most instances, the analysis is not straightforward and the results are not unambiguous since the interpretation of the data requires some model of the distribution of the persistent currents throughout the volume of the sample. As was pointed out previously, the analysis of four probe data is also subject to the same uncertainty.

The persistent currents are referred to as magnetization currents when they are

induced by a change in the externally applied field, and as transport or conduction currents when fed through the specimen via leads attached directly to an external current source. These two kinds of currents are not physically different, although the procedures for introducing them in the sample and the methods for monitoring their presence are different. In both sets of situations the analysis of the measurements to yield $j_{c\perp}$ and $j_{c//}$ vs B is straightforward only in the range of strong externally applied magnetic fields H_a, where the magnetic field generated by the currents is small compared with H_a. Under the latter circumstances, the currents can be considered to flow in a uniform field H_a. Consequently when the transport current attains the critical value I_c or the magnetic moment reaches a saturation value (identified by the envelope or limits of the magnetization curves), the currents are believed to fill the entire specimen and the data now readily yields accurate and unambiguous values for $j_{c\perp}$ or $j_{c//}$ vs H_a.

The four probe and the magnetic techniques offer alternative venues in obtaining data on the critical current densities in type II superconductors. In some instances both methods must be employed in order to obtain a complete and accurate picture of the configuration of the magnetic flux density and of the persistent currents in the specimen [11], [12]. In fact when H_a is directed along I in the low field range, information on the intricate patterns of current flow mentioned previously can only be obtained by simultaneously monitoring the magnetic moment which appears when the conduction current is applied and raised to $I_{c//}$ [32] – [34]. Further on this theme, the appearance of Meissner currents expelling magnetic flux from the superconductor (the Meissner effect) and their evolution with temperature can only be monitored using the magnetic method.

1.2 Framework of the Investigation

It is useful to outline the state of knowledge regarding the relative magnitude of $j_{c\perp}$ and $j_{c//}$ in type II superconductors prior to this investigation.

It seems to be well established from extensive critical current measurements that in strong pinning materials which can support large $j_{c\perp}$, such as $NbTi$, Nb_3Sn, $NbZr$ and $MoRe$, that $j_{c//}$ exceeds $j_{c\perp}$ by two or more orders of magnitude in the range where H_a approaches H_{c2}, and that $j_{c//}$ scales with $j_{c\perp}$ in that field range [9], [18], [25] – [27], [46].

The information concerning $j_{c//}$ on these materials in the range of low fields ($H_a \ll H_{c2}$), is sparse, sometimes less reliable and usually less clear cut. However the available results indicate that $j_{c//}$ exceeds $j_{c\perp}$ by factors approaching and straddling one order of magnitude [18], [25], [26]. A systematic investigation of magnetic behaviour in the flux cutting regime performed on three different materials (Nb, V, VTi) exhibiting modest pinning, shows that $j_{c//}$ scales with $j_{c\perp}$ in the range of low magnetic fields ($H_a \ll H_{c2}$) [6], [10].

Information in the literature on $j_{c//}$ and its ratio to $j_{c\perp}$ in weak pinning, hence semi-reversible, type II superconductors, is virtually non-existent. The two pertinent studies [26], [50] which have been reported present an incomplete picture of these quantities in $NbTa$.

The landscape is quite barren on the fundamental theoretical side. The problem of $j_{c//}$ has been investigated for an ideal, pinning free, hence reversible, material [8]. The subsequent calculations lead to a $j_{c//}$ which is much greater than any observed values [17].

On empirical grounds, LeBlanc and his graduate students [5] [20], [40] have

proposed and applied a simple double critical state model which has successfully accounted for most of the pertinent published observations [4], [6], [7], [10], [37]. Clem and his collaborators [13] – [17], [43] – [45] have developed a phenomenological theory which encompasses the double critical state picture as one of three possible scenarios. Consequently the Clem framework is considerably more powerful and versatile than the simple double critical state model. Unfortunately, it is also considerably more difficult to implement computationally. These models allow the generatation of a wide variety of critical current curves and magnetic behaviour of the spectrum of type II superconductors as the conduction current I and/or the externally applied magnetic field $\vec{H}_a$ are varied. The dependence of $j_{c//}$ and $j_{c\perp}$ on B and T serve as inputs. Conversely, using these models, information on $j_{c//}$ and $j_{c\perp}$ can be extracted from the measurements of $I_{c//}$ and $I_{c\perp}$, vs H_a and from the observations of the magnetic response of various materials.

In this thesis the empirical model and the Clem phenomenological framework will be outlined and exploited for the interpretation of experimental results.

1.3 The Project

It is clear from the preceding summary that the documentation on $j_{c//}$ in type II superconductors, particularly regarding its dependence on the pinning strength, hence on its variation with $j_{c\perp}$, is quite incomplete. Thus an area where the information is scant, namely the range of low fields ($H_a \ll H_{c2}$) and the behaviour where the pinning is weak and moderate, was investigated.

1.3.1 Choice of Materials

From a literature search two conventional type II superconductors $PbBi$ and $PbIn$, were identified which:

- exhibited the desired properties.
- could be readily prepared, machined and annealed in the laboratory.
- have a superconducting transition temperature T_c above 4.2 K.
- possess an upper critical field H_{c2} which is not excessive at 4.2 K.

For this project, the requirement that T_c exceed 4.2 K was paramount in order to minimize liquid helium consumption. The need to pump on the liquid helium in order to investigate a material where $T_c \leq 4.2\ K$ would not only introduce complications but appreciably augment the liquid helium consumption. This work was in progress when the high T_c superconductors were discovered. Investigations parallel to those described in this thesis are underway in our laboratory at 77 K, employing nitrogen as a coolant.

In general, the pinning strength of a given material can be modified by cold work (such as drawing a wire through a dye, extruding a sheet between rollers), fast neutron bombardment and thermal annealing. The latter method is clearly the most convenient and was adopted in this investigation. However, as will be discussed in chapter 3, only a modest reduction in the pinning strength of the $PbBi$ samples was achieved using this procedure.

It is well documented that $j_{c\perp}$, hence the pinning strength of type II superconductors grows as the temperature T is lowered below T_c. In fact $j_{c\perp}$ can be varied

from negligible near T_c , to a maximum for the given specimen at $T = 0$. However, all of the pertinent parameters, such as H_{c1}, H_{c2}, the penetration depth λ, the coherence length ξ, the thermodynamic critical field H_c, hence the condensation energy $\mu_0 H_c^2/2$, also vary with temperature. Consequently this manner of changing $j_{c//}$ and $j_{c\perp}$ is expected to be fruitful only if these two quantities differ in their dependence on T/T_c, hence their relationship to the basic parameters. This avenue was also explored. Unfortunately the available mechanical pump was inadequate to appreciably lower the temperature of the helium bath in the large dewars necessary to accommodate the experimental assembly.

As expected from previous studies the *PbBi* and *PbIn* samples differed appreciably in their relative pinning strength. The former exhibited moderate and the latter, weak pinning. Appropriate magnetic measurements on these two materials allowed the examination of the variation of $j_{c//}$ with respect to $j_{c\perp}$ in this region of the pinning spectrum at low H_a/H_{c2}.

1.3.2 Choice of Method

A variety of methods can be explored to establish configurations of persistent currents where a component $j_{//}$ of the total current density $\vec{j}$, is flowing parallel to the magnetic flux density.

As noted previously, this can be achieved by impressing a conduction current I along the sample immersed in a static magnetic field H_a directed along the current. Although in this arrangement the conduction current does not flow straight down the wire or ribbon, but forms a macroscopic whirlpool centered along the axis of the specimen. Consequently the magnetic moment which is generated parallel to I by this pattern of current flow, must be monitored by some magnetic measurement

in order that the data on $j_{//}$ and $j_{\perp}$ be complete. Thus in these investigations, the method of introducing the current via leads connected to an external source appears to offer no advantage and presents several disadvantages already enumerated.

Clearly if persistent currents are not fed into the sample via leads, they must be generated by inductive means. Since measurements of $j_{c//}$ as well as $j_{c\perp}$ are sought, the inductive procedure which is selected must ensure that the persistent currents are made to flow with a component parallel to B. Various simple schemes to accomplish this have been developed and investigated in our laboratory. In particular, this can conveniently be achieved by using a sample in the form of a disk which is slowly rotated in a stationary externally applied magnetic field H_a, directed parallel to the flat faces of the disk and perpendicular to the axis of rotation [5], [38]. Alternatively, the disk can be held stationary while the magnetic field $\vec{H}_a$ is rotated. This procedure is harder to implement and the phenomena are more difficult to monitor. The rotating disk arrangement also has the attractive feature that as the rotation proceeds, the evolution of the magnetic moment is in itself of much interest. The variety of behaviour which is encountered in these situations provides useful information for various applications. Further the phenomena observed shed light on the dynamics and interaction of flux lines in type II superconductors. The experimental arrangement and procedures are described in the next chapter.

Chapter 2

EXPERIMENTAL SET UP

2.1 Introduction

In this work persistent currents are induced to circulate in a disk of a type II superconductor by changing its orientation in a static externally applied magnetic field H_a, which is directed parallel to the flat faces of the disk and perpendicular to the axis of rotation. Since the diameter of the disk is large compared to its thickness, the demagnetization factor along $\vec{H}_a$ is negligible. The configuration of persistent currents which are generated in this manner flow with components both parallel and perpendicular to the magnetic flux density $\vec{B}$. These components are denoted as $j_{//}$ and $j_{\perp}$ respectively and their critical values $j_{c//}$ and $j_{c\perp}$.

To see why the rotation of the disk in a static $\vec{H}_a$ establishes patterns of circulating currents with components parallel and perpendicular to $\vec{B}$, it is perhaps easier to examine the equivalent situation where the disk is kept fixed while the magnetic field $\vec{H}_a$ rotates at a constant rate.

The rotating magnetic field can be expressed as:

$$\vec{H}_a = \vec{y}H_a sin\theta + \vec{z}H_a cos\theta \quad (1)$$

In this procedure the focus is set on an arbitrary increment $\Delta\theta = \theta_2 - \theta_1$. To fix ideas θ_1 and θ_2 are taken to lie in the range $0 < \theta < \pi/2$.

The increment $\Delta\theta$ causes the y component of $\vec{H}_a$ to increase an amount ΔH_y and the z component to decrease an amount ΔH_z. By Faraday's law of induction :

- the increase in the applied magnetic flux along $\vec{y}$ induces persistent currents which tend to oppose this increase, hence to circulate along $\vec{z}$ as shown in figure 1 a).
- simultaneously, the decrease in the applied magnetic flux along $\vec{z}$ induces a circulation of current along $\vec{y}$ which tends to oppose this decrease, as shown in figure 1 b).

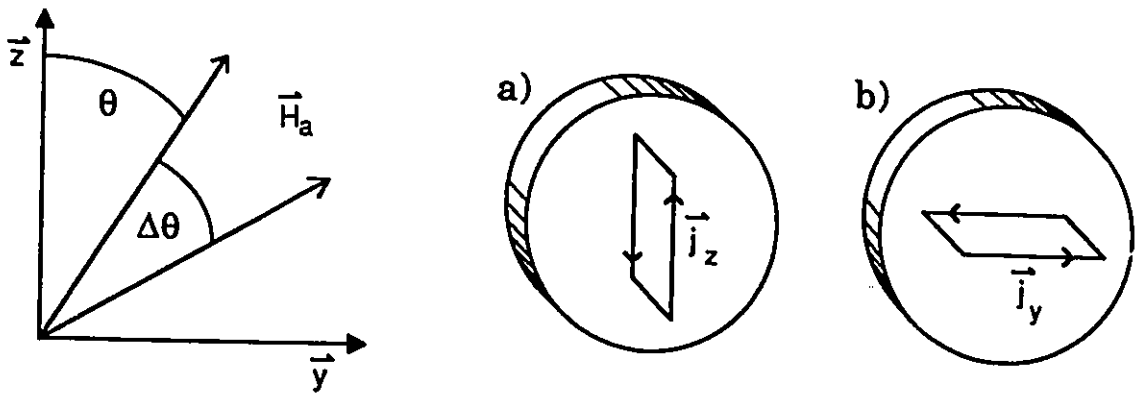

Figure 1: Geometry of current densities.

Of note is the fact that $\vec{j} = \vec{y}j_y + \vec{z}j_z$ along the flat faces of the disk will be directed approximately along H_a, thus possess a significant component parallel to H_a hence denoted as $j_{//}$.

One can focus on the depinning critical current $j_{c\perp}$ in the absence of $j_{//}$ by keeping the orientation of the disk fixed and varying the magnitude of H_a, but keeping its direction θ fixed. Here again, by Faraday's law of induction, persistent currents will be induced to circulate in the disk to oppose the entry or exit of the applied magnetic flux. If the specimen is isotropic, these induced currents will flow perpendicular to H_a. Measurements of the magnetic moment as H_a is applied and removed, yield information on $j_{c\perp}$. This is the standard magnetic method mentioned in the introductory chapter. Recall that a current $\Delta I = \vec{j} \cdot d\vec{s}$ circulating around an area 'A' constitutes an elementary magnetic dipole or magnetic moment :

$$\Delta\vec{\mu} = \vec{A}\,(\,\vec{j} \cdot d\vec{s}\,) \tag{2}$$

and,

$$\vec{\mu} = \sum \Delta\vec{\mu} \tag{3}$$

the vector sum or integral of these individual moments or dipoles, is the magnetic moment of the specimen. Thus :

$$\vec{M} = \frac{\vec{\mu}}{V} \tag{4}$$

is the magnetization or magnetic moment per unit volume where 'V' is the volume of the specimen.

In this set up, the evolution of the magnetic moment as, *(i)* $\vec{H}_a$ is varied in strength or *(ii)* the disk is rotated with $\vec{H}_a$ kept fixed, is continuously monitored using two orthogonal pickup coils which embrace the specimen.

Details on the samples, the experimental set up and procedures, are now provided.

2.2 Experimental Set up

2.2.1 Samples Employed

The disk samples prepared were made up of $PbBi$ and $PbIn$ respectively. A literature search showed that the former alloy exhibits appreciable hysteresis when quenched from the melt, hence possesses significant pinning strength. Further, annealing at a modest temperature over a relatively short period of time (a day or two) can substantially reduce the hysteresis, therefore diminish $j_{c\perp}$. From published reports, the $PbIn$ is known to show much less irreversibility (hysteresis) hence weak pinning after quenching from the melt. Furthermore pinning can be easily diminished by annealing this alloy at a modest temperature over a convenient time interval. Consequently these two alloys enable one to investigate the variation of $j_{c//}$ with $j_{c\perp}$ and the phenomenon of flux cutting in a region of the pinning spectrum which has been essentially unexplored to date. Both alloys have a transition temperature in the vicinity of 6 K, allowing study at 4.2 K, the temperature of liquid helium at atmospheric pressure. Pb, Bi and In of high purity are readily available and inexpensive. The constituent of these alloys with the highest melting temperature, Pb melts at an accessible $327\,^{\circ}C$. Thus homogeneous ingots are easily prepared due to the low melting points. The upper critical field H_{c2} at $4.2\,K$ is not excessively large ($\approx 10^4$ *Gauss*), allowing investigation over a wide fraction of H_a/H_{c2} without difficulty.

Large ingots were prepared by mixing slivers or cuttings of the constituents in the desired proportions, namely $Pb_{(0.45)}Bi_{(0.55)}$ and $Pb_{(0.46)}In_{(0.54)}$. The mixtures were sealed in evacuated quartz tubing, melted at $400\,^{\circ}C$ and periodically shaken

while at this temperature during a frame of a few hours. The $PbBi$ molten ingot was then quenched by transfering the container to the ambient air. The $PbIn$ ingot was cooled gradually to $100\,°C$, annealed at this temperature for twenty-four hours, then cooled gradually to the ambient temperature by turning off the furnace.

Disks of 19 mm diameter and 0.8 mm thickness were then cut on a metal lathe from the ingots. One of the $PbBi$ disks was sealed under vacuum and annealed for twenty-four hours at $120\,°C$.

2.2.2 Sample Disk Assembly

Each disk is held rigidly in place by a delryn support. This assembly is wound (bifilarly) with a single layer of 38 gauge enamelled manganin wire for heating purposes (see figure 2). This allows for destruction of previous magnetic history of the sample by heating above T_c, thereby ensuring that every measurement in any chosen magnetic field H_a is started with a 'clean slate'. Furthermore, the signal observed upon heating to T_c provides a final measure of the magnetic moment existing in the specimen at this juncture (independent of possible electronic drift). This procedure serves as an important check on the data. A bifilar noninductive, winding arrangement ensures that adjacent turns of the wire carry current flowing in the opposite direction, thus avoiding any net magnetic field and net magnetic moment generated by the heater. Since the manganin wire is nonmagnetic (develops no magnetization in the applied field H_a), it does not contribute a background signal. A layer of epoxy is painted on the heater coil to keep it firmly in place. This support in turn, is placed between two brass disks with thin mylar spacers (0.025 mm) on each side of the sample. The mylar provides additional electrical and thermal insulation between the heater and the brass disks. Shafts perpendicular

to the surfaces of the brass disks serve as the axis of rotation and as contact points for heating purposes.

Electrical contacts are made by soldering the two heater wire leads to the separate brass disks. This enables heating of the sample by feeding current via the brass disks. Sliding metallic contacts pressed against each shaft feed the current assembly from the 'outside'. A delryn ring epoxied between the brass disks unites the assembly, which can easily be rotated in liquid helium.

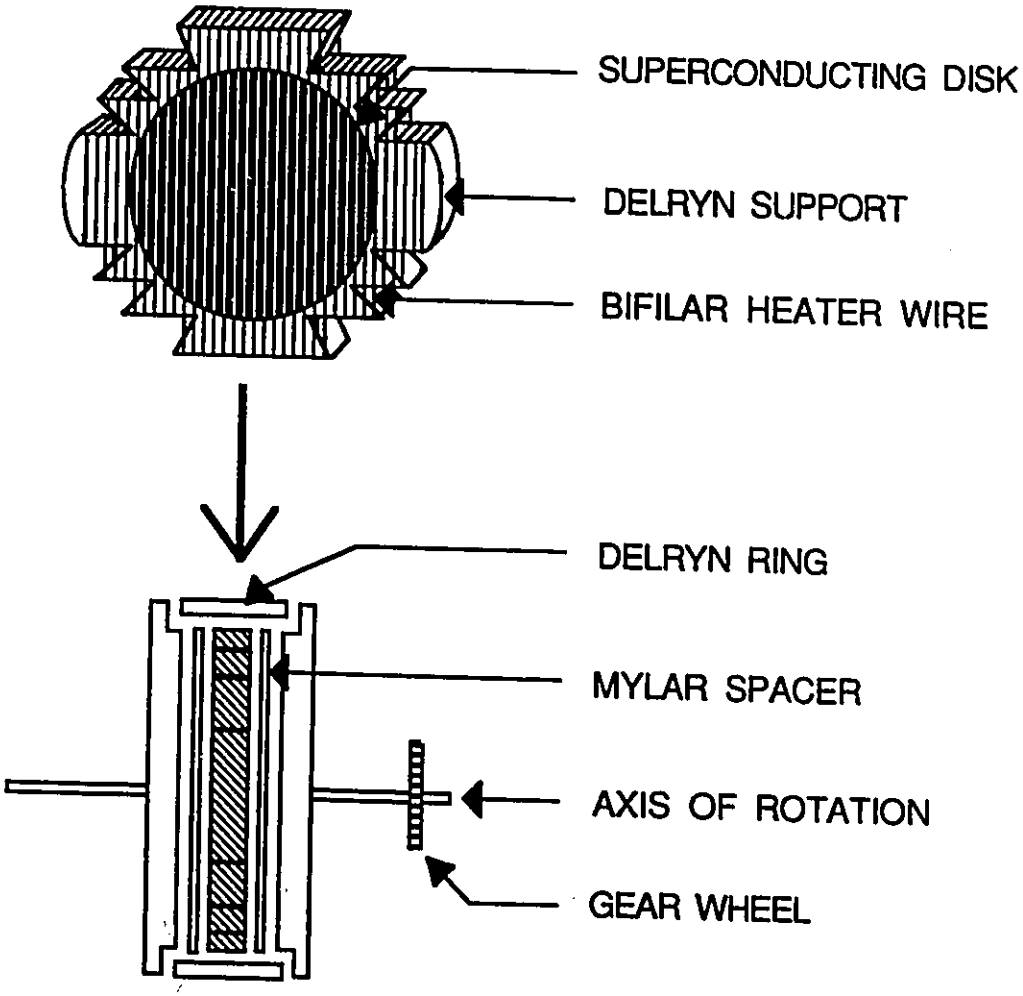

Figure 2: Sample disk assembly.

The entire assembly can be rotated by turning the axle of the brass disks via a toothed wheel mounted on one of the shafts. This is achieved by a worm gear system which is driven by a long stainless steel shaft. The shaft extends outside of the top plate attached to the Helium dewar and is in turn coupled with the shaft of a ten turn helipot which rotates in unison with the disk. A constant applied voltage to the helipot potentiometer provides a signal proportional to the angle through which the sample disk is rotated.

2.2.3 Pickup Coil Assembly

The evolution of the magnetic moment of the disk specimen is monitored via pickup coils. The rotating disk assembly is encompassed by a set of two orthogonal pickup coils which are fixed in place and orientation. They embrace the magnetic flux threading the sample in directions parallel and perpendicular to the externally applied magnetic field. The direction of $\vec{H}_a$ is denoted as the z axis. The disk is positioned with its flat surfaces in the y-z plane, thus the axis of rotation and the width of the sample are directed along the x axis. For assembly purposes each coil consists of two halves, which are joined physically and electrically around the disk assembly. Each portion contains 8,500 turns of 48 Gauge formvar insulated copper wire (see figure 3).

The pickup coils monitor the evolution of $< B_z >$ and $< B_y >$, the spatial averages over the thickness of the disks of the $\vec{z}$ and $\vec{y}$ components of the magnetic flux density $\vec{B}(x)$ which is permeating the sample. The corresponding components of the magnetization are denoted as $< M_z >$ and $< M_y >$.

Since there is no externally applied magnetic field along the y axis in this set

up, the general relationship:

$$< B_y > = \mu_o H_y + \mu_o < M_y > \tag{5}$$

simplifies to :

$$< B_y > = \mu_o < M_y > \tag{6}$$

Therefore, in this case these two physical quantities are equivalent and interchangeable.

Although it is frequently easier to visualize the physical behaviour of type II superconductors in terms of magnetic flux and the magnetic flux density permeating them, it is experimentally more convenient to measure $< M_z >$ instead of $< B_z >$. Consequently, the standard procedure removes (electronically) the contribution of the applied magnetic flux from the measurements by means of a bucking coil which responds to variations of H_a, but does not sense the magnetic field of the sample. The bucking coil is connected in series opposition to the 'main' coil which embraces the sample. The area-turn product of copper wire is carefully adjusted so that the combined arrangement is balanced and yields no net signal when H_a is varied *(i)* in the absence of the specimen or, *(ii)* with a nonmagnetic superconducting specimen in place, but in the normal state. Thus :

$$\mu_o < M_z > = < B_z > - \mu_o H_a \tag{7}$$

is monitored simultaneously with :

$$< B_y > = \mu_o < M_y >$$

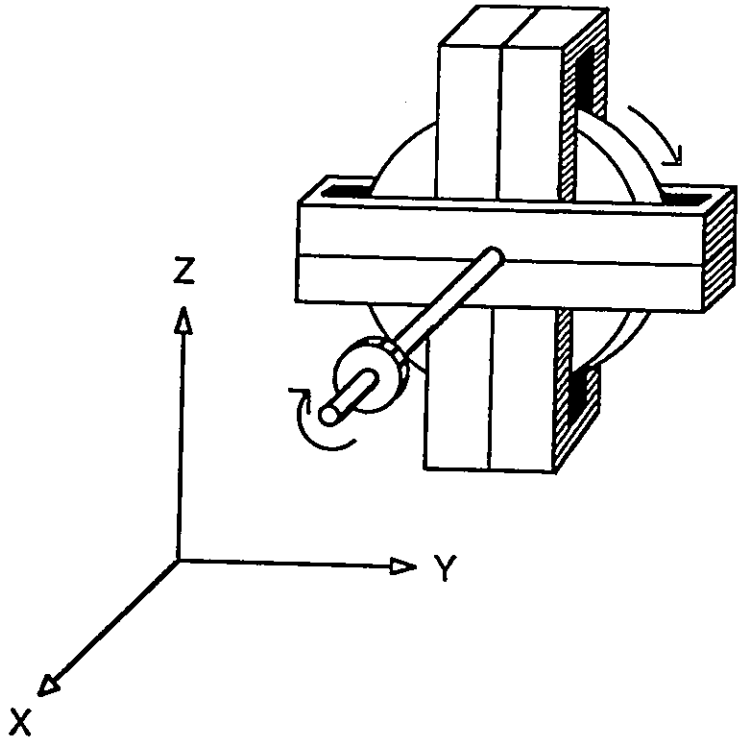

Figure 3: Pickup coil assembly.

Each of the two pickup coils separately feeds an amplifier-integrator system (Par Model 215), each driving the Y axis of an X – Y recorder. Thus it is possible to simultaneously and continually monitor $< M_x >$ and $< M_y >$ as, *(i)* H_a is varied, thereby tracing out standard magnetization curves, and *(ii)* the disk is rotated with H_a fixed. In the former instance, the X axis is driven by a signal proportional to the applied magnetic field, which is generated by a voltage drop across a shunt placed in the circuit. In the latter circumstance, the X axis is driven by a signal proportional to the angle of rotation θ of the disk, which is generated by a constant voltage across a potentiometer.

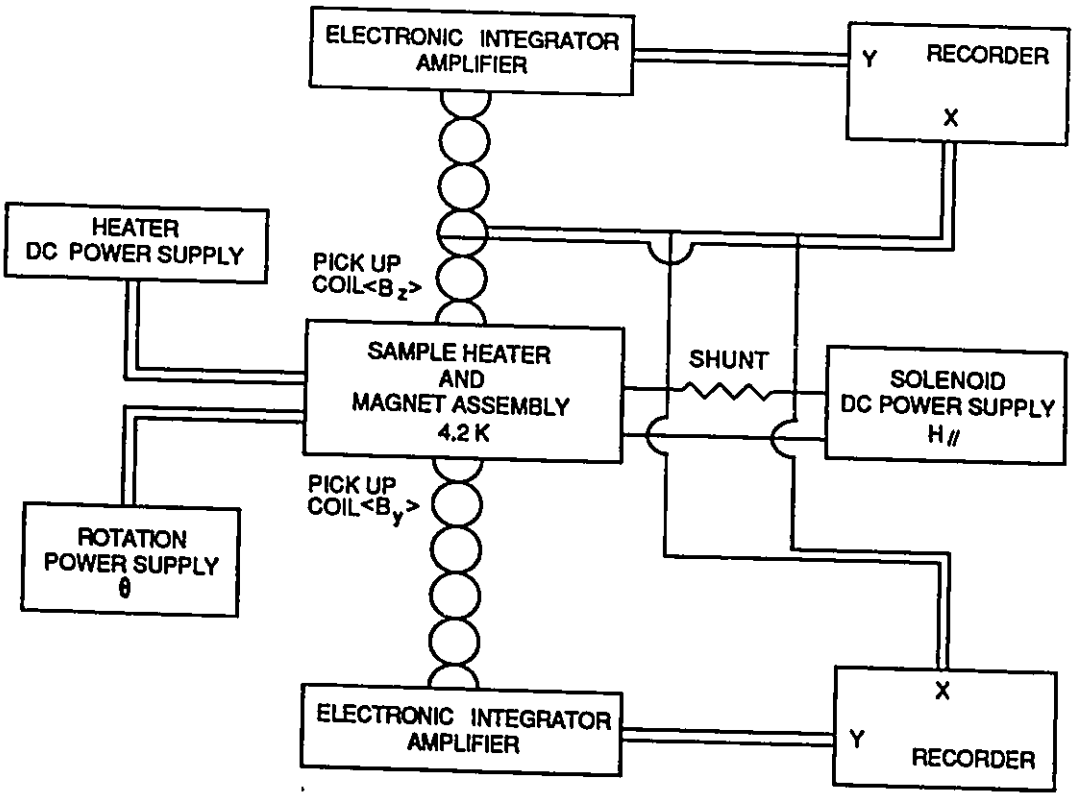

Figure 4: Schematic of the experimental set up.

2.2.4 Superconducting Solenoid

The bucking and pickup coil assembly (including the sample-heater system and rotation mechanism) fit snugly in a delryn support cylinder. This in turn is mounted tightly inside a $NbTi$ superconducting magnet, which provides the applied magnetic field $\vec{H}_z$. The magnet has an 18 cm length, 4 cm outer diameter, 3 cm inner diameter, and is wound with 0.4 mm diameter formvar insulated, multifilamentary $NbTi$ wire. The solenoid is much longer than the sample and thus is able to generate

a homogeneous axial field over the area of the disk. The applied magnetic field is estimated to be homogeneous within 1% over the dimensions of the disk sample. The operating solenoid used throughout generates 741 Gauss/Ampere. The magnetic field is ripple free since the superconding solenoid is energized by a battery driven transistorized power supply and can be stabilized to $\leq 0.1\%$ over the duration of most measurements.

The current fed to the superconducting coil flows through a standard shunt. The voltage across this shunt drives the X axis of the $X - Y$ recorders when it is desired to monitor the evolution of the magnetic moment of the sample versus H_a. A sensitive digital voltmeter connected across the shunt also allows the current flowing through the solenoid to be monitored to an accuracy of four significant figures.

2.2.5 Calibration

The $< M_z >$ signals from the pickup coils are calibrated on the assumption that perfect shielding against the entry of H_a occurs under application of magnetic flux to the virgin state in the range $H_a < H_{c1}$. The response is perfectly diamagnetic (linear) in this region because the penetration of the magnetic flux is restricted to the penetration depth $\lambda \approx 10^{-5}$ cm, which is minute when compared to the dimensions of the disk (half thickness: $X = 4 \times 10^{-2}$ cm). Virgin is defined as the state of the sample when it has become superconducting by cooling in the absence of a magnetic field from $T \geq T_c$ to some $T < T_c$. In this work, and in many investigations, the presence of the earth's magnetic field is negligible.

The $< B_y > = \mu_o < M_y >$ data is calibrated against $< M_z >$ by rotating an arbitrary residual magnetic moment (remanent trapped flux) of the superconducting

disk from the z to the y direction. Magnetic flux is trapped in the superconductor by either, *(i)* subjecting it to a sweep of magnetic field H_a of magnitude well above H_{c1} or, *(ii)* letting the disk become superconducting in a static field H_a (which may be greater or less than H_{c1}) by cooling from T_c to the ambient temperature. In both procedures, it is imperative that H_a be reduced to 0 (*i.e.* the earth's field or less), before the disk is rotated since, as shall be seen later, flux cutting that is generated by rotation when $H_a \neq 0$ will lead to the release of some of the trapped flux and also affect the alignment and distribution of flux with respect to the disk.

Sinusoidal curves of $\mu_o < M_y > = < B_y >$ and $\mu_o < M_x > = < B_x >$ are mapped out as the superconducting disk (with trapped flux) is rotated. The $< M_x >$ signal maps out a cosine while the $< M_y >$ signal generates a sine curve as the rotation of the trapped magnetic moment proceeds from the z axis through the y axis, then toward the negative z direction and so on. The amplitudes of the two resulting sinusoidal curves display the same magnetic moment. Since $< M_x >$ is known from the standard calibration indicated previously, the calibration of $< M_y >$ follows.

The distance between the maxima and minima of the sine and cosine curves traced out on the X − Y recorders serves to calibrate the X signal versus θ, the angle through which the disk is rotated.

Chapter 3

STANDARD MAGNETIZATION CURVES

3.1 Introduction

Information on the pinning of flux lines in type II superconductors, hence on the critical current density $j_{c\perp}$ for depinning, can be conveniently obtained from standard magnetic measurements.

3.2 Reversible Magnetic Behaviour

Since there is no flux line pinning in the ideal (reversible) type II superconductor, then $j_{c\perp} = 0$. Consequently the magnetic behaviour and the magnetization curve, are quite simple and history independent. As H_a is raised from zero, the specimen exhibits perfect screening against the entry of the applied magnetic flux, until H_a attains H_{c1}. Therefore $< M >= H_a$ in this range because $< B >= 0$. The effective

shielding current diminishes with H_a from its maximum at H_{c1} to negligible at H_{c2} as flux lines nucleate at the surface, penetrate and distribute uniformly inside the specimen. If H_a is lowered in intensity from any arbitrary value $0 < H_a < H_{c2}$, the magnitude of the persistent screening surface current (denoted as the Meissner current) adjusts to remain in equilibrium with H_a, with no change occurring in its diamagnetic, field opposing, sense of circulation. Although a considerable amount of flux is exiting from the sample as H_a is decreased towards H_{c1},the surface screening current makes no attempt to retain the escaping flux. On the contrary, by its growth, the Meissner current contributes to the release of this magnetic flux. This is a lesser known and less publicized aspect of the fascinating Meissner effect in type II superconductors.

When the specimen is allowed to cool from T_c to the final temperature T in any chosen field $H_a < H_{c2}$, the density of flux lines in the material and the net Meissner current circulating at the surface, adjust to yield the same magnetic moment that is observed when H_a is applied from zero at constant T. Consequently flux lines are expelled from the sample and the Meissner current grows in strength as T is decreased from T_c. This is a second, better known, manifestation of the Meissner effect. Conversely flux lines enter as the Meissner current diminishes while T is raised to T_c when $H_a > H_{c1}(T)$.

Although the physics involved in the behaviour of the ideal type II superconductor is extremely intriguing and intricate, the locus of $< M >$ vs H_a at constant T is now well known and straightforward, displaying a 'triangular' shape with a readily identified H_{c1} and H_{c2}, the only two parameters required for its complete characterization.

3.3 Irreversible Magnetic Behaviour

In non ideal (irreversible) materials, pinning sites impede the migration of flux lines. Thus the magnetic response is irreversible and the magnetization curves show hysteresis. As a consequence, the locus of $< M >$ versus H_a is now very complicated and the magnetic response depends on previous magnetic/thermal history in the superconducting state. The identification of H_{c1} is no longer straightforward. The importance of this parameter dwindles as pinning (hence $j_{c\perp}$) grows in magnitude.

In a non ideal material, a variety of magnetic moments (both diamagnetic and paramagnetic in sign and spanning a wide range of magnitudes), can be generated. This is in sharp contrast to the case of an ideal material, where a unique magnetic moment exists with a specific configuration of circulating currents and magnetic flux for a chosen $H < H_{c2}$ and $T < T_c$. (A magnetic moment is said to be diamagnetic when $< B > < \mu_o H_a$ and paramagnetic when $< B > > \mu_o H_a$, although the material is non-magnetic in the normal state). For selected H and T, numerous distinct configurations of magnetic flux and persistent currents can yield a magnetic moment with the same magnitude and sign. It is therefore mandatory in the investigation of the magnetization curves of these materials, that the path followed in the $H-T$ plane be recorded. Figures 5 and 6 display (schematically) the evolution of $< M >$ versus H_a as observed in weak and strong pinning type II superconductors when these specimens are subjected to certain prescriptions of particular importance.

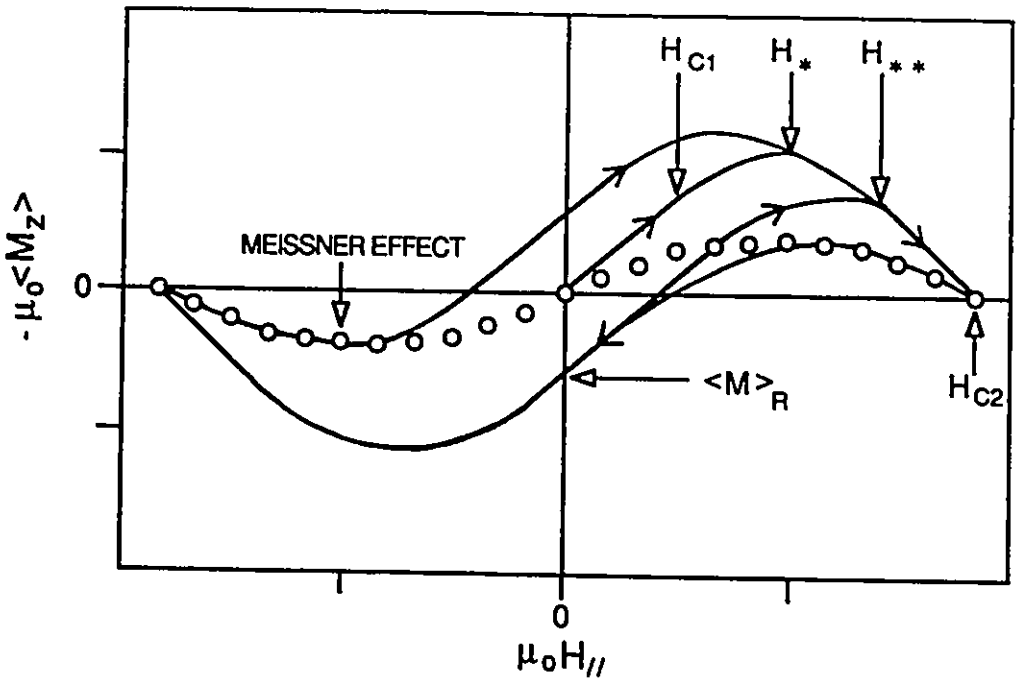

Figure 5: Characteristic Magnetization Curves, for a semi-reversible sample.

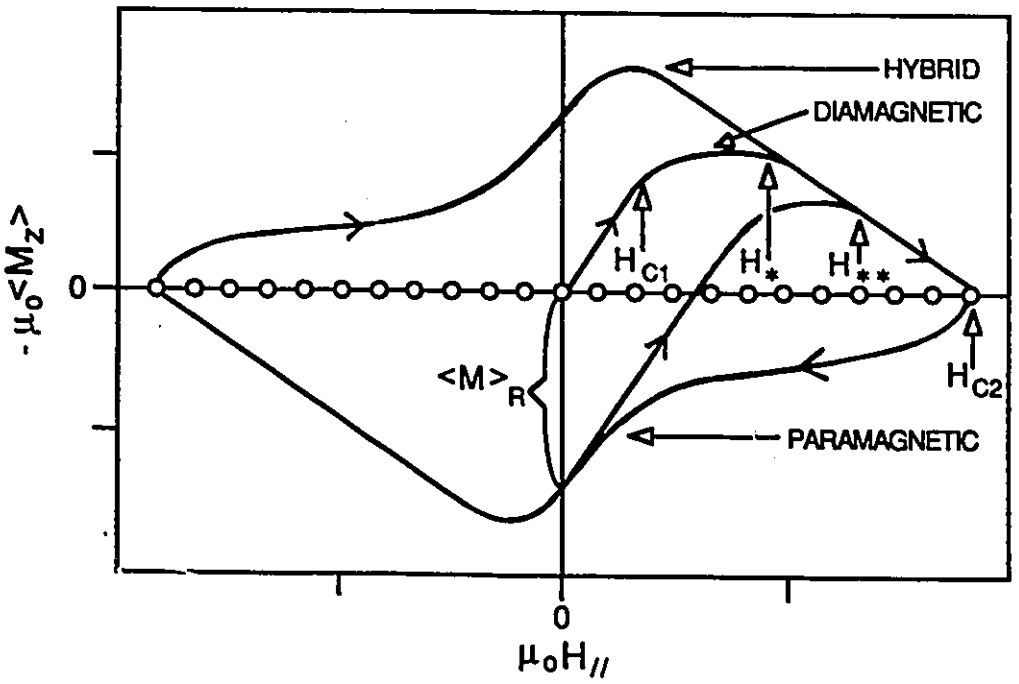

Figure 6: Characteristic Magnetization Curves, for an irreversible sample.

Since a typical full cycle hysteresis loop generated by swinging H_a between H_{max} and $-H_{max}$ is symmetric about the $H_a = 0$ axis, only two of the quadrants will be displayed (for economy of space) in all subsequent figures.

The concept of the critical state density $j_{c\perp}$ for the persistent currents appearing in the volume of the material (where the sense of the circulation of $j_{c\perp}$ is governed by the laws of electromagnetic induction), together with the picture of an equilibrium Meissner current flowing at the surface, provide a framework for a qualitative and quantitative account of the variety of behaviour.

From inspection and analysis of data as displayed in figures 5 and 6, one can assess, *(i)* the role played by pinning, *(ii)* the magnitude of $j_{c\perp}$, *(iii)* its dependence on B, and *(iv)* the variation of the Meissner current with H_a. Such a detailed analysis is not within the scope of this thesis. It will suffice for our purpose to indicate various features which can be explored to gauge and classify the degree of irreversibility.

3.4 Parameters Classifying Irreversible Behaviour

Starting with $H_a = 0$ and the specimen in the virgin state (*i.e.* no magnetic flux of either polarity threading the sample), the initial application of H_a is seen to induce a persistent flux shielding, surface current and $< B >$ remains zero until H_{c1} is attained as in the ideal case. When H_a exceeds H_{c1}, the magnitude of $< M >$ can continue to rise since persistent currents of density $j_{c\perp}(B)$ are induced in the bulk or volume of the specimen. (The succession of profiles sketched in figure 7 a) may assist in visualizing the sequence of events).

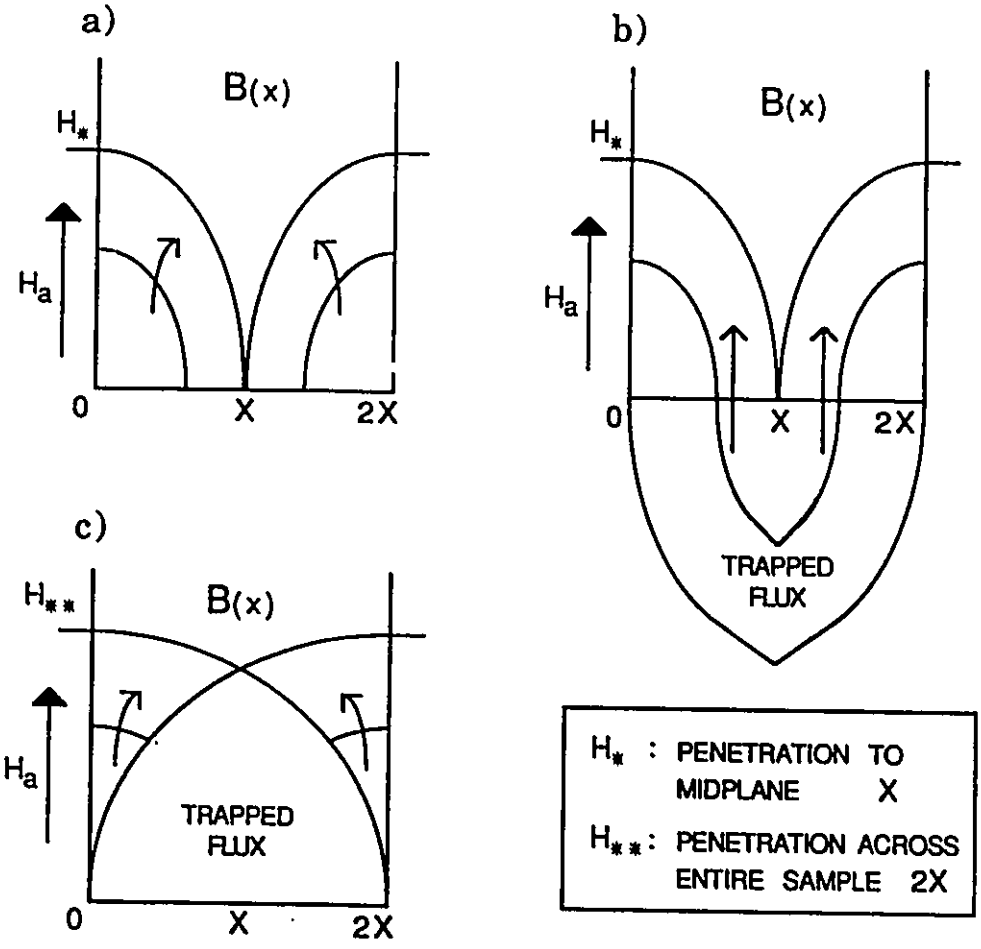

Figure 7: Magnetization profiles across the width of the specimen.

The increase in $< M >$ vs H_a ceases to be linear, and the onset of the deviation from linearity indicates that H_{c1} has been reached.

As the rise in H_a continues, the magnetic flux (in the form of flux vortices) penetrates deeper into the body of the specimen, advancing from the two surfaces (situated at $x = 0$ and $x = 2X$ in figure 7). Eventually the two migrating flux fronts meet at the midplane of the disk sample. At this point, the entire specimen is saturated (filled) with circulating persistent current, where the local density $j_{c\perp}$

may depend on the local magnitude of the flux density $B(x)$. We note that by Maxwell's equation :

$$\nabla \times \vec{B} = \mu_o \vec{j} \tag{8}$$

and the critical state concept; any region where a gradient in the magnetic flux density exists, is correspondingly occupied by a persistent current density $j_{c\perp}$.

The sweep in H_a required for magnetic flux front to penetrate to the midplane, hence, to fill the specimen with induced persistent currents, is of special interest and serves as a useful parameter to characterize and compare non ideal type II superconductors. This first full penetration field is denoted as H_*. Since there is no magnetic probe or sensor situated at the midplane of the solid specimen to inform one that the advancing flux front has arrived at that position, the experimental determination of H_* evidently presents a problem. Indeed the locus of $< M >$ vs H_a as the magnetic field is initially applied, shows no distinguishing feature as this benchmark is traversed.

Various procedures have been developed for the determination of this quantity. It is sufficient here to note that H_* can be measured (as illustrated in figures 5 and 6) by monitoring the field H_a where the magnetization curve labelled hybrid merges with the initial diamagnetic curve. The physical basis for this identification emerges from a comparison of the sequence of B profiles sketched in figures 7 a) and b). The latter displays a sequence of configurations of magnetic flux density generated as H_a is varied from a large value of one polarity, through zero and finally to a large value of the opposite polarity. As H_a swings between zero and H_* in this process, the specimen contains flux lines of the original polarity in the vicinity of the midplane and flux lines of the new polarity adjacent to the surface. The interface between these two regions migrates inward as H_a moves from 0 to H_*. The resultant

configurations are termed hybrid since they contain a mixture of two 'species' of flux lines. One species consists of flux lines directed along $\vec{H}_a$ in the outer volume, while the other has flux lines in the interior directed against $\vec{H}_a$.

Another useful quantity in the characterization and comparison of hysteretic type II superconductors is denoted as H_{**}. This parameter is related to, *(i)* H_*, *(ii)* the maximum remanent (residual) magnetic moment (trapped flux) and, *(iii)* the critical conduction current I_c. The exposition of all of these features is beyond the scope of this introduction. One of the procedures for measuring H_{**} is depicted in figures 5 and 6, and the corresponding sequence of B profiles, in figure 7 c). Starting with a maximum (saturation) amount of trapped flux in the specimen at zero applied field, H_a is impressed in the previously applied direction. The field H_a where the locus of $< M >$ meets the initial diamagnetic curve identifies H_{**}. It is noted from figure 7 c) that the initial and final B profiles map out a continuous distribution across the entire width of the specimen. This is also the configuration which is generated when a conduction current $I = I_c$ is made to flow in a hysteretic type II superconductor.

H_* and H_{**} readily provide useful information on $j_{c\perp}$ in the corresponding range of H_a and on the dependence of $j_{c\perp}$ on B in that range. It follows from Maxwell's equation for planar geometry $\partial B/\partial x = \mu_o j_\perp$, and the critical state model (incorporating the presence of a reversible surface Meissner current) that :

$$< j_{c\perp} >_* = \frac{\left(H_* - I^*_{eq}\right)}{X} \tag{9}$$

where I^*_{eq} (Amps/unit length) is the reversible diamagnetic (Meissner) surface current in equilibrium with $H_a = H_*$, and $< j_{c\perp} >_*$ is the spatial average of $j_{c\perp}$ over the range $0 < H < (H_* - I^*_{eq})$.

Also :

$$< j_{c\perp} >_{**} = \frac{\left[H_{**} - (I_{eq}^{**} + < j_{c\perp} >_{*} X)\right]}{X} \tag{10}$$

where I_{eq}^{**} is the Meissner current in equilibrium with $H_a = H_{**}$. Here $< j_{c\perp} >_{**}$ is the spatial average of $j_{c\perp}$ over this range $(H_{*} - I_{eq}^{*}) < H < (H_{**} - I_{eq}^{**})$.

It is a major challenge to accurately determine I_{eq} vs H_a from the experimental data when $H_a > H_{c1}$. Theoretical calculations of I_{eq} vs H_a are complicated and in principle, valid only when T is near T_c. Consequently various analytic empirical approximations have been proposed. In particular, the simple relation :

$$I_{eq} = \frac{H_{c1}^2}{H_a} \tag{11}$$

is frequently exploited in the range $H_{c1} < H \ll H_{c2}$. From inspection of equations 44 and 45 we note that the role of I_{eq}, hence the importance of its accurate determination, recedes as the pinning is made stronger and H_{*} (or H_{**}) overwhelm the contribution of I_{eq} (I_{eq}^{*} or I_{eq}^{**}).

The maximum residual (or remanent) magnetization denoted as $< M >_R$ and generated by trapping a saturation amount of magnetic flux (see figure 7 c)) is another useful measure of the pinning strength in the low field range, hence $j_{c\perp}$ in this range. The maximum flux may be trapped by, *(i)* applying and removing a sufficiently large magnetic field $H_a > H_{**}$ at constant $T < T_c$, or *(ii)* cooling the specimen from T_c to T in an arbitrary field $H_a > H_{*}$, which is then reduced to zero. The first procedure was followed in these measurements.

Also of special interest in the characterization of non-ideal type II superconductors are $< M >_{*}$ and $< M >_{**}$, the magnetizations at H_{*} and H_{**} respectively.

The measurements of these various parameters for the samples explored are compiled in the following table.

	$Pb_{.46}In_{.54}$ T = 4.2 K	$Pb_{.45}Bi_{.55}$ T = 4.2 K	$Pb_{.45}Bi_{.55}$ T = 3.0 K	$Pb_{.45}Bi_{.55}$ ANNEALED
H_* (Gauss)	157	1015	1148	822
H_{C1}	119	345	402	296
$<M>_R$	16	477	528	411
$<M>_*$	102	335	425	279
H_{**}	162	1400	1560	1101
$<M>_{**}$	92	245	310	301

Table 3.1: Experimental parameters.

For simplicity, the superconducting disk can be visualized as an infinite slab of thickness $2X$. Thus the magnetization along H_a (viewed as a superposition of magnetic dipoles $\Delta\mu = A\Delta I$, where A is the area embraced by the element of current ΔI), can be written as :

$$< M >= \pm \left[\frac{1}{X} \int_0^X j_{c\perp}(X - x)dx \right] - I_{eq} \tag{12}$$

where $\Delta I = j_{c\perp}dx$ and $A = XY$. The geometric factor YZ cancels out since $< M >= \mu/XYZ$ by definition. $j_{c\perp}$ is taken as negative when flowing in a field opposing (diamagnetic) sense, and positive when circulating in a flux retaining sense.

Alternatively, focusing on the spatial average of the magnetic flux density $< B >= \mu_o H_a + \mu_o < M >$ permeating the disk, for planar geometry :

$$< M >= \pm \left[\frac{1}{X} \int_0^X dx \int_0^x j_{c\perp}(x')dx' \right] - I_{eq} \tag{13}$$

Note that $I_{eq} = H_a$ when $H_a < H_{c1}$, hence $I_{eq} = 0$ when $H_a = 0$.

Usually simple, physically plausible, analytic expressions are postulated for

$j_{c\perp}$ vs B, and their validity is tested by integrating equations 12 and 13, and comparing the calculated and observed $< M >$ values.

Two simple approximations are frequently exploited in these calculations and are enshrined in the literature. The Bean-London approximation [2], [3], [39] states that $j_{c\perp}$ is independent of B :

$$j_{c\perp} = \alpha_B \tag{14}$$

Conversly the Kim-Anderson approximation [1], [28] – [30] states that $j_{c\perp}$ is inversely proportional to B :

$$j_{c\perp} = \frac{\alpha_K}{B} \tag{15}$$

Here α_B and α_K are temperature dependent coefficients which characterize the pinning strength of the specimen. Theoretical considerations also indicate that these expressions also define the limits or extremes on the possible range of dependence of $j_{c\perp}$ on B. Consequently, it is useful to map out the behaviour predicted by these two approximations. This approach will be followed in the analysis of the observations. The two expressions mentioned will be referred to as the Bean and Kim approximations for brevity.

Equations 14 and 15 imply an infinite H_{c2}, hence apply when $H_a < H_{c2}$. The role of H_{c2} is introduced in an approximate manner, by adding a factor $[1-(B/B_{c2})]$ on the right hand side in equations 14 and 15 :

$$j_{c\perp} = \alpha_B \left(1 - \frac{B}{B_{c2}}\right) \tag{16}$$

$$j_{c\perp} = \frac{\alpha_K}{B} \left(1 - \frac{B}{B_{c2}}\right) \tag{17}$$

3.5 The Meissner Effect

As noted earlier, the flux expulsion (Meissner effect) magnetization observed upon cooling from T_c to T in a stationary H_a in ideal type II superconductors, coincides with the magnetization appearing when H_a is increased from zero with T fixed. These data cease to overlap when pinning comes into play. As pinning increases in strength, the magnitude of the diamagnetic response grows as witnessed by the rise in the parameters H_* and H_{**} relative to H_{c1}, while the magnitude of the Meissner magnetization shrinks. Eventually the Meissner effect disappears. This can be readily understood qualitatively.

In type II superconductors, the Meissner effect results from an imbalance between, *(i)* the mutual repulsion of parallel flux lines, and *(ii)* the magnetic pressure exerted by the external field on the flux lines. The equilibrium between these opposing forces is reached when the flux line density in the material has decreased below the applied magnetic flux density $B_a = \mu_o H_a$. When $H_a < H_{c1}$, the equilibrium is reached only when the flux lines have all repelled each other from the specimen. The expulsion of flux lines from a type II superconductor in response to their mutual repulsion is increasingly impeded by the pinning forces as the temperature is lowered below T_c. Consequently the equilibrium that ensues is mainly one between these opposing driving forces in the body of the specimen. The absence of the Meissner effect therefore indicates that the pinning forces are sufficiently powerful to imprison all of the flux lines in the sample. Conversely, the occurence of a Meissner effect indicates relatively weak pinning and an ideal Meissner effect is the signature of zero pinning. Thus the ratio of the Meissner magnetization to H_{c1} serves as a gauge of pinning strength. This gauge is of limited value since it ceases

to operate once the pinning is sufficiently strong that it negates the manifestation of the Meissner effect.

The equilibrium between the mutual repulsion of the flux lines and their interaction with the externally applied field is also responsible for the second mode or manifestation of the Meissner effect, namely the growth in the magnitude of the diamagnetic moment as H_a is decreased from H_{c2} to H_{c1}. In pinning free materials, $< M >$ vs H_a is independent of previous history and the magnetization curve with H_a decreasing is identical to that for H_a increasing, which in turn overlaps with the plot of the magnetization developing during cooling in any chosen H_a. It is noteworthy that there exists a range of weak pinning in type II superconductors where there is overlap between, *(i)* the locus of $< M >$ vs H_a decreasing, and *(ii)* the plot of $< M >$ appearing during cooling in H_a. This behaviour is shown schematically in figure 5 and exhibited by our *PbIn* specimen (see figure 9). This behaviour arises because the mutual repulsion of the flux lines, although opposed by the pinning forces, is sufficiently strong to dislodge and expel flux lines over the entire cross-section of the specimen as it cools from T_c (see figure 8 a)).

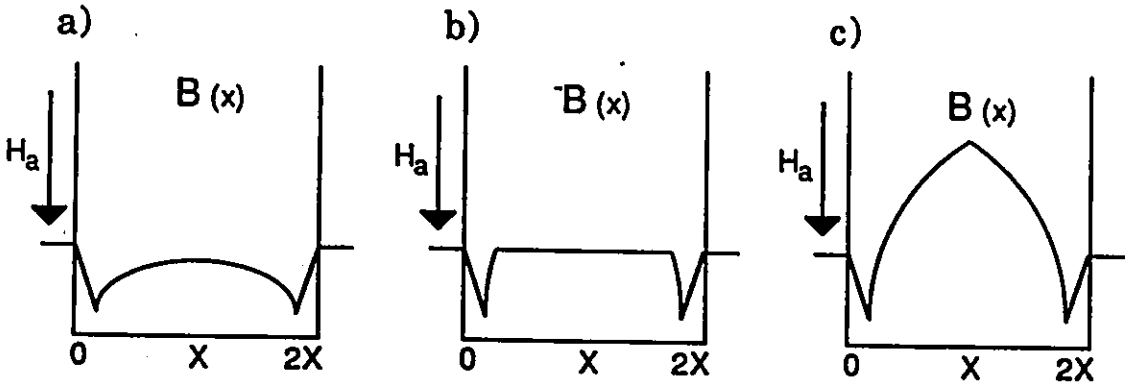

Figure 8: Magnetization profiles (as pinning strength increases).

As pinning strengthens, the volume in which the flux expulsion takes place becomes more and more restricted to a shrinking annular region in the vicinity of the surface (see figure 8 b)). In this sense the Meissner effect becomes a surface phenomenon and exhibits a 'size' dependence. Comparison of the B profiles displayed in figures 8 b) and c), explains why the return (H descending) curve deviates from the flux expulsion (cooling) data as the pinning grows. Eventually with stronger pinning, no flux expulsion occurs and the return curve lies entirely in the lower (positive) quadrant.

3.6 Experimental Results

3.6.1 Major Hysteris Curves

Since pinning opposes *(i)* the entry of flux lines into the superconducting volume, and *(ii)* any release or exit of flux lines already permeating these materials, it is not surprising that the magnetization curves for increasing and decreasing H_a, diverge more and more as pinning grows. Consequently as pinning is made stronger, the separation increases between the upper and lower branches of $< M >$ vs H_a curves as H_a is cycled back and forth between $+H_{c2}$ and $-H_{c2}$. This contrast in magnetic response is shown schematically in figures 5 and 6, and emerges from a comparison of the measurements on the *PbBi* and *PbIn* samples displayed in figures 9 through 13.

The outermost curves are referred to as the envelope of the major hysteresis loop. At any juncture, a reversal in the sense of the sweep of H_a will cause the locus of $< M >$ to move from one branch of the envelope to the other, if allowed

to proceed over a sufficiently great magnitude. Of particular interest is the reversal of the sense of the sweep of H_a as it swings through zero. The expression 'half cycle' refers to hysteresis loops where the sign (direction or polarity) of H_a does not change as it is cycled between zero and H_{c2}. The expression 'full cycle' denotes the major hysteresis loop, where H_a swings between + and $-H_{c2}$.

Regardless of whether H_a changes sign during swings which cause $< M >$ to traverse from one branch of the envelope to the other, *(i)* ΔH_a^c, the magnitude of the sweep in H_a required to accomplish this, and *(ii)* $\Delta < M >_c$, the magnitude of the change in the magnetization which is then observed, both provide important and complementary information on $I_{c\perp}$, hence $j_{c\perp}$ vs B. These features are examined in some detail in the thesis of G. Gandolfini [22].

3.6.2 Catalogue of Standard Magnetization Curves

Figures 9 through 13 display the measurements of the major elements of the $< M >$ vs H_a curves, as well as the flux expulsion (Meissner effect) data for the *PbBi* and *PbIn* samples. For economy of space, the data for each case is displayed in two quadrants only. As illustrated schematically in figures 5 and 6, a four quadrant display of the magnetization curves is redundant since the information is duplicated. Several important parameters (benchmark values) extracted from these curves are listed in Table 3.1.

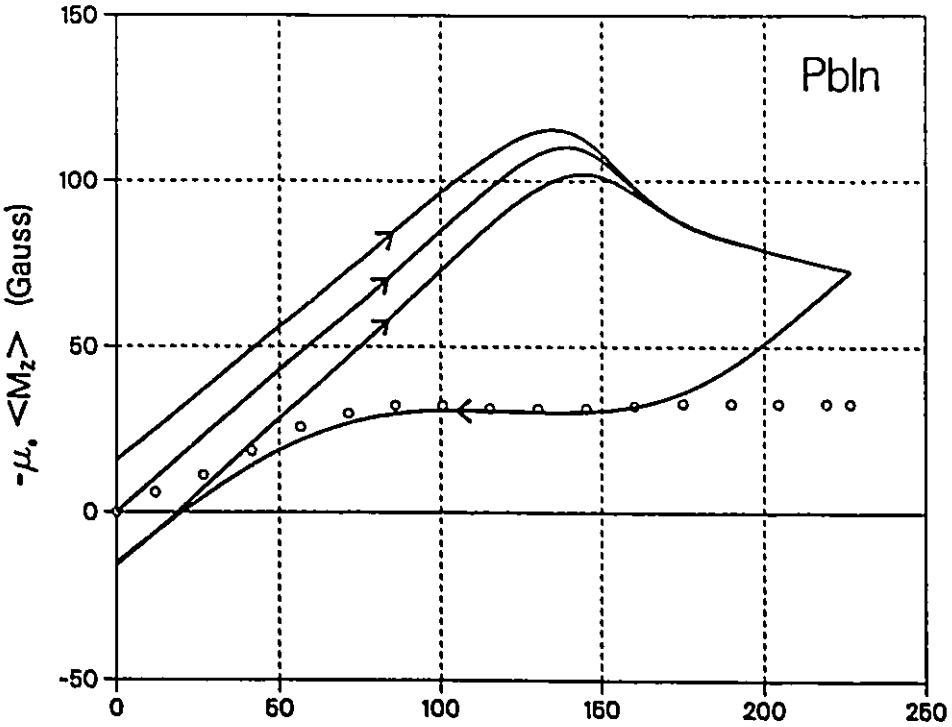

Figure 9: *PbIn* Magnetization Curves.

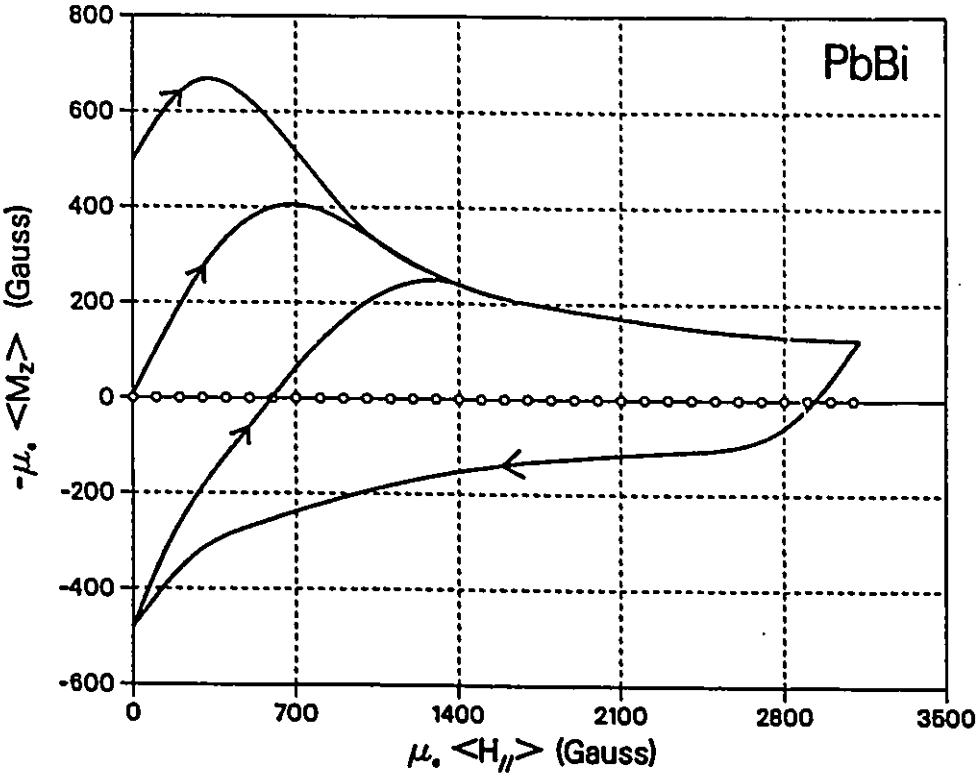

Figure 10: *PbBi* Magnetization Curves.

The behaviour of the *PbIn* sample should be compared with any of the families of *PbBi* data curves. For convenience the former and one of the latter are juxtaposed on page 37. It may also be helpful to refer to the schematic curves displayed in figures 5 and 6. This comparison reveals that the hysteresis (hence the pinning) is considerably more pronounced in *PbBi* than in *PbIn*. Indeed, the behaviour of the latter is described as semi-reversible since, *(i)* the curve of $< M >$ vs H_a descending, lies in the diamagnetic regime except for a display of unimpressive flux trapping in the very low field region, and *(ii)* an appreciable Meissner effect is observed when the specimen is cooled from T_c to $4.2\ K$ in various static H_a. By contrast, the 'return' $< M >$ vs H_a curve for the *PbBi* sample, crosses over and remains in the paramagnetic (flux trapping) region, and no Meissner effect is observed within the accuracy of the detecting system ($\Delta < M > \leq 1\ Gauss$).

The three sets of families of data curves for the *PbBi* disk are displayed in figures 11, 12 and 13) for ease of comparison. Inspection reveals that, *(i)* only a modest reduction in the pinning strength in this material was achieved by annealing the sample at $120\,°C$ for 24 hours, and *(ii)* only a modest increase in the pinning strength was achieved by reducing the temperature from $4.2\ K$ to $T \approx 3.0\ K$ (the best that was accomplished with the available mechanical pump and the various heat leaks into the large dewar).

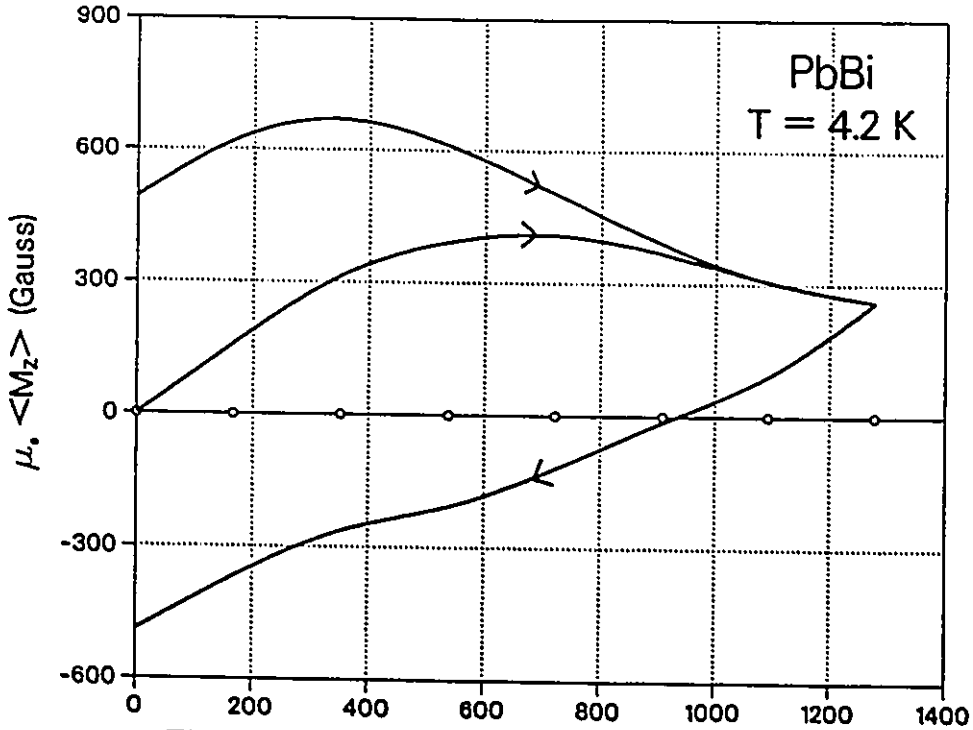

Figure 11: $T = 4.2$ K, *PbBi* Magnetization Curves.

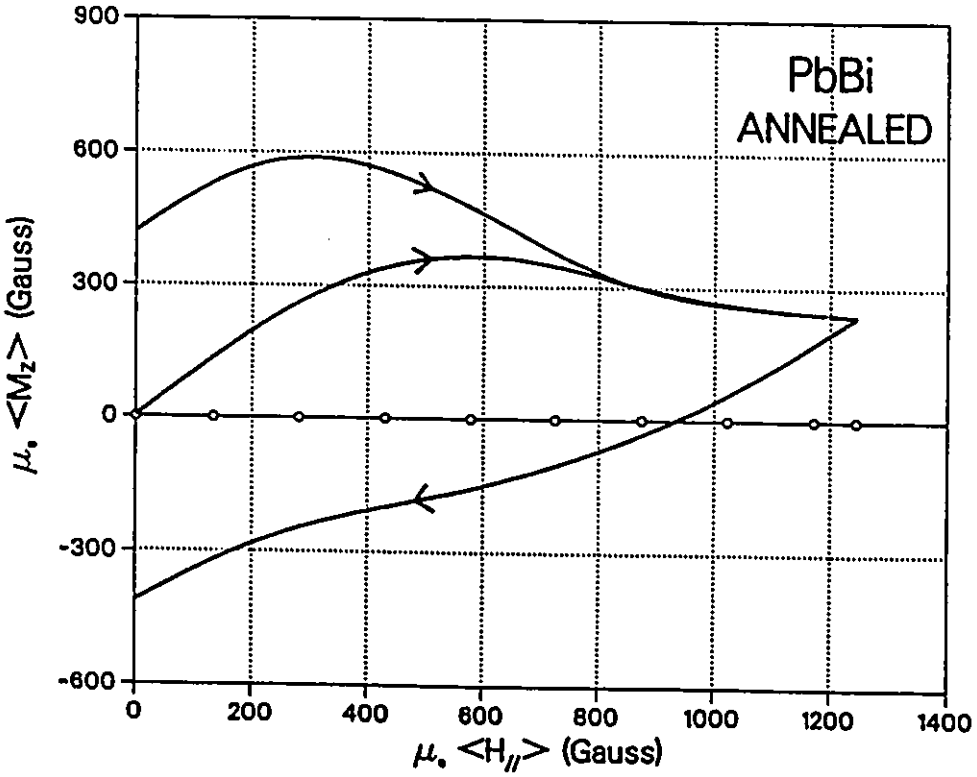

Figure 12: Annealed *PbBi*: Magnetization Curves.

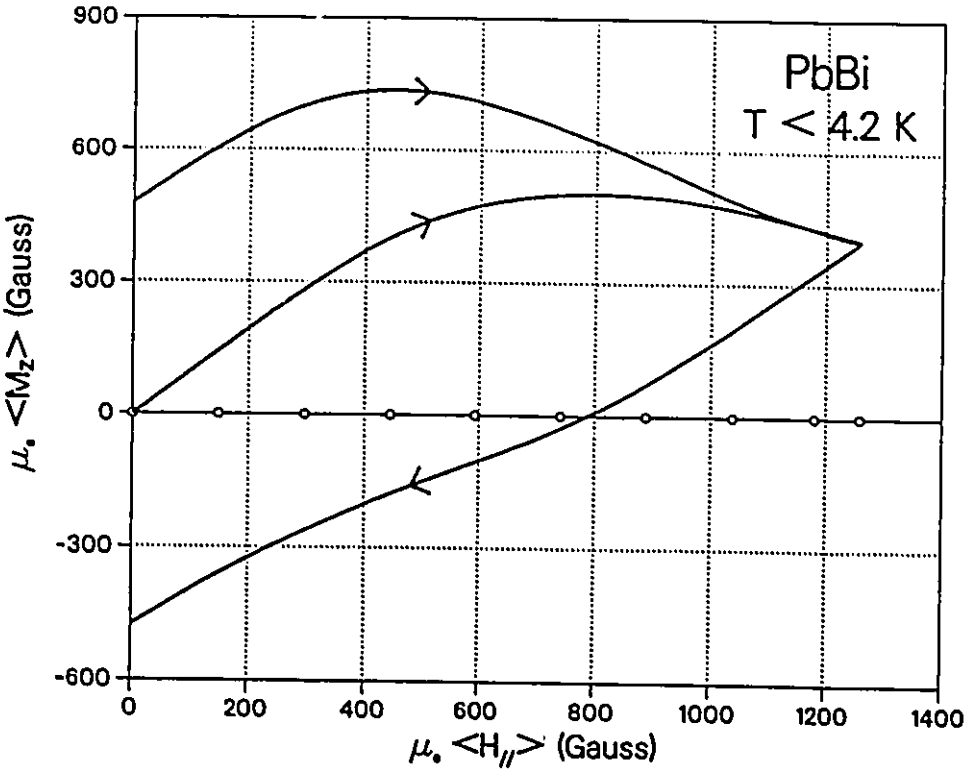

Figure 13: $T < 4.2\,K$, *PbBi* Magnetization Curves.

It was also carefully verified whether the samples are isotropic. This was accomplished by comparing the magnetization curves (such as displayed in figures 9 and 10) measured with H_a directed along any arbitrary diameter of the disk with that observed with the disk having been rotated (in the virgin state) through 30°, 60° and 90° with respect to the original setting. The corresponding magnetization curves overlapped within experimental accuracy indicating that the specimens were indeed isotropic.

Now equipped with complete information on the relative pinning strength of the materials, the flux cutting behaviour is explored and thereby obtaining insight into $j_{c//}$ in the low field range.

Chapter 4

MAGNETIZATION CURVES OF ROTATING DISKS

4.1 Introduction

The preceding chapter fully documented the major magnetizations curves of the *PbBi* and *PbIn* samples. The effect of pinning on their magnetic response to changes of magnetic field and temperature has been characterized. Their ranking in the hierarchy of irreversible behaviour has been carefully established. The next step is to investigate and compare the behaviour of magnetic flux and persistent currents in these two materials with different pinning properties, when the disk specimens undergo slow rotation in static magnetic fields $\vec{H}_a$.

Under these circumstances, the current density $\vec{j}$, induced by the rotation of the disk, flows with a component $j_{//}$ along $\vec{H}_a$, consequently along the local flux line density. When the current density $j_{//}$ exceeds a critical value $j_{c//}$, the flux lines (along which $j_{//}$ is flowing) undergo a process called 'flux line cutting'. This process

plays a crucial role in the rotation of flux lines in type II superconductors and is therefore responsible for the changes occurring in the direction of the magnetic flux density in these materials. In this chapter observations of these phenomena are presented. In the following chapter these ideas will be exploited to account for the recorded behaviour.

4.2 Description of the Observations

To ensure a simple and well defined initial configuration of the magnetic flux in the specimen, the disk was first cooled from T_c to 4.2 K in a selected static field $\vec{H}_a$ (along the z axis) which was kept fixed in magnitude and direction during the measurement. Any flux expulsion which occurred during the cooling stage was carefully recorded. The evolution of $< M_y >$ and $< M_z >$, the y and z components of the magnetization of the disk were simultaneously monitored as the disk was slowly rotated. The rate of rotation was kept at approximately one revolution per ten seconds. The observed behaviour is independent of the rate of rotation. This was verified by changing (increasing and decreasing) the rate by factors of three, and also by proceeding incrementally instead of continuously.

An illustrative sampling of the observations is displayed in figures 14 through 25. The structure of the curves of $< M_y >$ and $< M_z >$ vs θ evolves in a similar manner for both the *PbBi* and the *PbIn* samples as H_a is increased. The development of the various features appears to scale with respect to the first full penetration field H_*, discussed in some detail in the previous chapter. It is of interest to recall that $H_* = < j_{c\perp} > X$ is also a good measure of the pinning strength of the specimen. Consequently, H_a, $< M_y >$ and $< M_z >$ have been normalized to the corresponding

H_* for each sample reported in chapter 3 and listed in table 3.1. The scaling with respect to H_* will be seen to follow naturally in the model which is proposed and developed in chapter 5.

Examination of the compilation of $< M_y >$ and $< M_z >$ vs θ curves reveals three distinct modes of behaviour encountered in the response of both the *PbBi* and *PbIn* to rotation:

- For $H_a/H_* \geq 2.0$, the locus of $< M_y >$ and $< M_z >$ rises monotonically to a plateau where it subsequently remains as the rotation continues.

- Over an intermediate range of H_a/H_* the locus of $< M_y >$ and $< M_z >$ rises monotonically, tracing out a peak before descending from this summit to a plateau where it remains as the rotation proceeds.

- In the range of small magnetic fields $H_a/H_* < 1$, the behaviour encountered appears quite intricate. Here $< M_y >$ and $< M_z >$ vs θ display damped oscillatory motion relative to a growing baseline. This pattern (with a 2π periodicity) may span several cycles. The number of cycles increases as H_a/H_* is chosen smaller. Subsequently, $< M_y >$ and $< M_z >$ trace out sinusoidal curves (also with a 2π periodicity) about a steady baseline. The magnitude of the baseline grows with H_a/H_*, while the amplitude of the sinusoidal component superimposed on the baseline diminishes and vanishes with increasing H_a/H_*.

A simple model, which fully accounts for all of this rich variety of phenomena, was first proposed by Boyer [5], [7]. This model suggested that the rotation of the disk with respect to $\vec{H}_a$ causes a valley to appear in the vicinity of the surface in the configuration of the magnetic flux permeating the disk. The way the depth and

breadth of this valley evolves as the rotation proceeds is crucial and is reexamined in the next chapter where the results are interpreted. In this chapter the focus is on compiling, examining and cataloging the observations.

4.3 General Remarks

Of note is the fact that the magnetic moment which evolves along the z axis (along $\vec{H}_a$) is diamagnetic, *i.e.* $< B_z >$ decreases below $B_a = \mu_o H_a$. This is to be expected since any rotation of the disk up to $\theta = 180°$ will tend to turn the flux lines permeating the disk, away from the z axis. The sign of the magnetic moment along the y axis is undetermined since there is no applied magnetic field in this direction. The positive sign is arbitrarily chosen for $< M_y >$ and $< M_z >$ is displayed in the same quadrant for ease in comparison of the relative magnitudes of these coexisting components of the total magnetization.

The baseline for the $< M_z >$ vs θ curves of the *PbIn* sample should be shifted vertically upwards by the magnitude of the Meissner effect (flux expulsion) magnetization which occurred during cooling in the selected H_a and is displayed in figure 9, of chapter 3. This background contribution to $< M_z >$ was removed for ease of comparison of the evolution of $< M_z >$ vs θ for the *PbIn* specimen with the *PbBi* which showed no Meissner effect.

Significant contrasts emerge from comparison of the behaviour of *PbBi* and *PbIn*, while the three sets of measurements for *PbBi* are quite similar. In particular, at $H_a/H_* = 2.0$, $|< M_z >| > < M_y >$ for the *PbIn* sample (see figure 16), whereas the opposite is encountered for *PbBi* (see figure 19). This dramatic difference is emphasized in the compilation of all the sets of data.

4.4 Graphical Compilation of the Observations

The choice of focus is on, *(i)* $< M_y >_{Max}$ and $< M_z >_{Max}$, the magnitude of the maxima traced out by the locus of $< M_y >$ and $< M_z >$ vs θ, and *(ii)* $\theta_{y(Max)}$ and $\theta_{z(Max)}$, the angles where these maxima appear. As noted above, in the range of $H_a/H_* \geq 2.0$, the maximum of $< M_y >$ and $< M_z >$, and the corresponding plateau are identical. $< M_y >_{Max}$ and $< M_z >_{Max}$, the maxima observed for $< M_y >$ and $< M_z >$ as the rotation took place, are plotted versus the various static H_a/H_* in figure 26. The corresponding angles $\theta_{y(Max)}$ and $\theta_{z(Max)}$, where these maxima appear, are plotted versus $H_a/H*$ and are displayed in figure 27. For completeness, the $< M_z >_{Max}$ of *PbIn* is displayed with and without the Meissner effect contribution to this component of the magnetization (see figure 26).

In our view, the salient features which emerge from the families of observations displayed in figure 26 (in arbitrary order) are the following :

- The height of the summits in the displays of the $< M_y >_{Max}$ and $< M_z >_{Max}$ for *PbBi* are comparable, whereas $< M_z >_{Max}$ is consistently much larger than $< M_y >_{Max}$ throughout the entire range of H_a/H_* for *PbIn*. Seen in another equivalent perspective, the the former intersect, while the latter do not.

- Although all of the sets of data are normalized to the corresponding H_* (a pinning parameter), the curves of $< M_y >_{Max}$ and $< M_z >_{Max}$ for *PbBi* lie well above that for the *PbIn* specimen.

- The summit of $< M_y >_{Max}$ for $PbBi$ occurs at a much larger value of H_a/H_* than that for the summit of $< M_x >_{Max}$, namely 1.4 versus 0.7. In contrast, the summits of $< M_y >_{Max}$ and $< M_x >_{Max}$ for $PbIn$ occur at comparable values of H_a/H_*, namely ≈ 0.7.

- The summits of $< M_x >_{Max}$ for $PbBi$ occurs in the vicinity of the summits of $< M_y >_{Max}$ and $< M_x >_{Max}$ for $PbIn$, all in the vicinity of $H_a/H_* \approx 0.7$.

The major aspects which emerge from inspection of figure 27 are the following :

- For the $PbIn$ specimen, the plot of $\theta_{x(Max)}$ (the angle of rotation for the generation of $< M_x >_{Max}$) vs H_a/H_*, shows a pronounced peak. No trace of such a peak is found in the corresponding data for the three sets of measurements on $PbBi$.

- $\theta_{y(Max)}$ is always appreciably smaller for the $PbIn$ specimen than for the $PbBi$.

It is now gratifying to present our model and show that it reproduces the overall structure of these intricate data curves and all of the salient features which have just been enumerated simply by varying the ratio of $j_{c//}$ to $j_{c\perp}$.

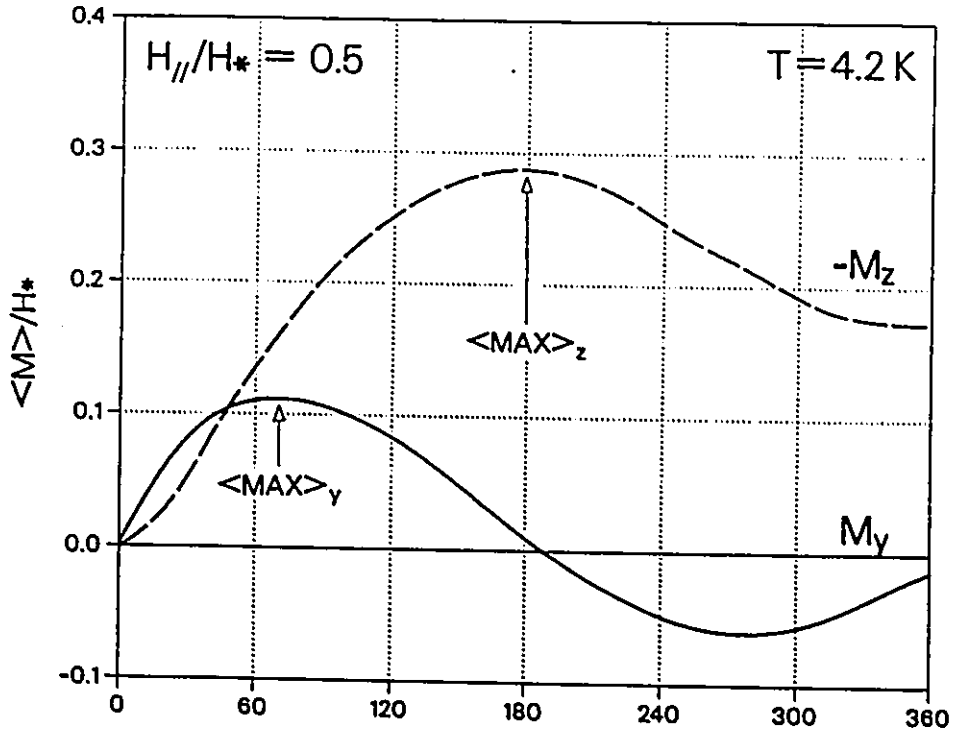

Figure 14: *PbIn* Rotational Curves, for $H_a/H_* = 0.5$.

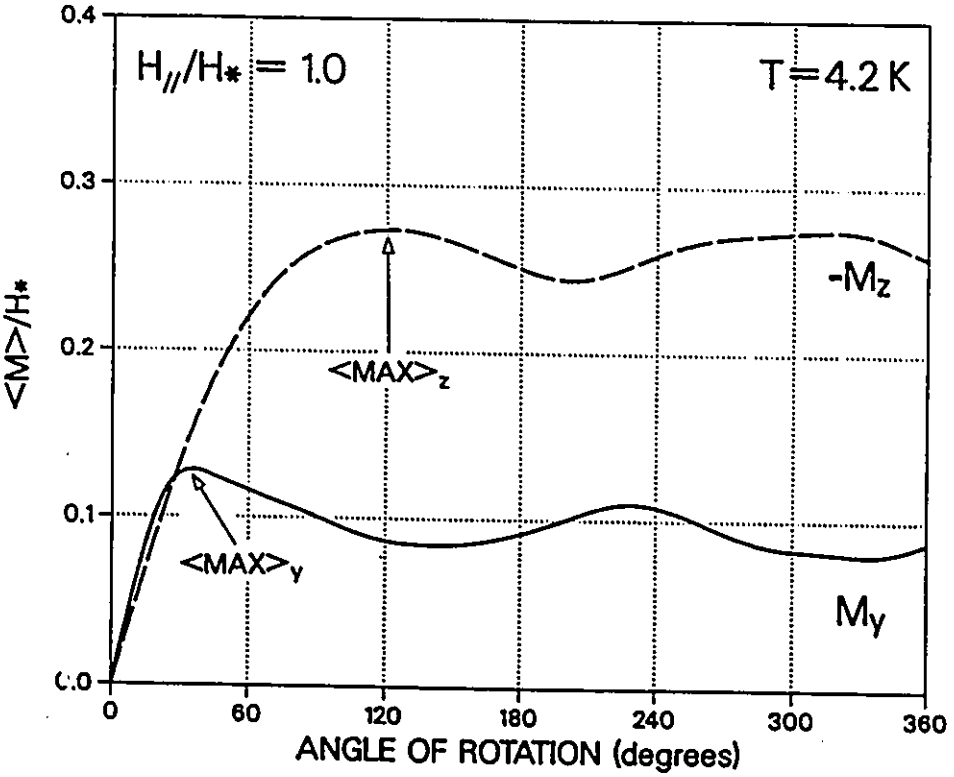

Figure 15: *PbIn* Rotational Curves, for $H_a/H_* = 1.0$.

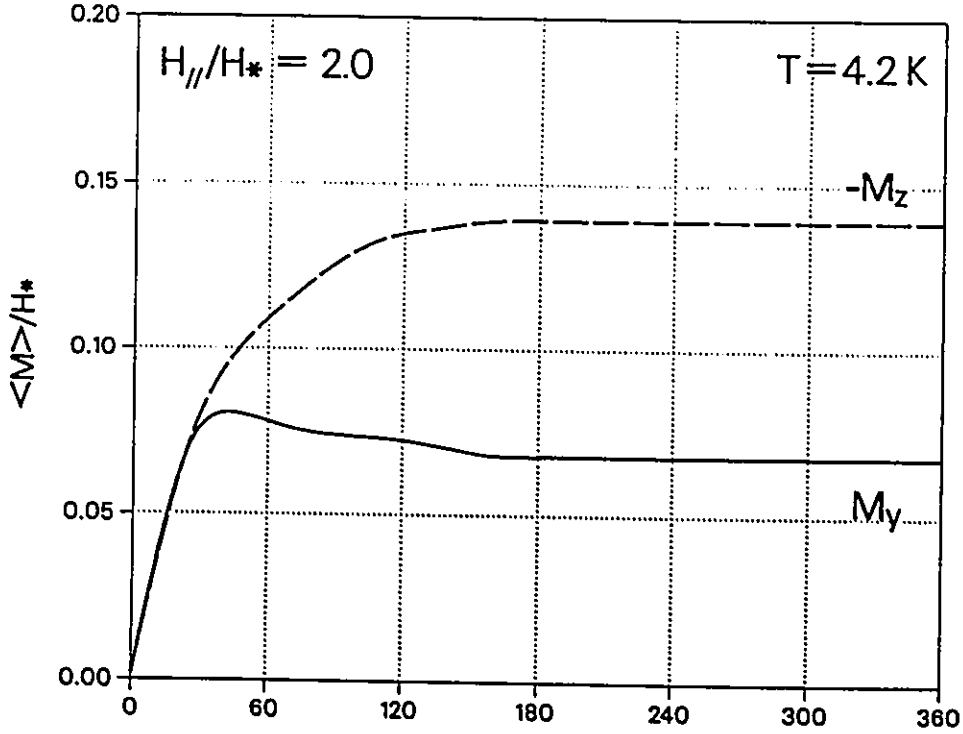

Figure 16: *PbIn* Rotational Curves, for $H_a/H_* = 2.0$.

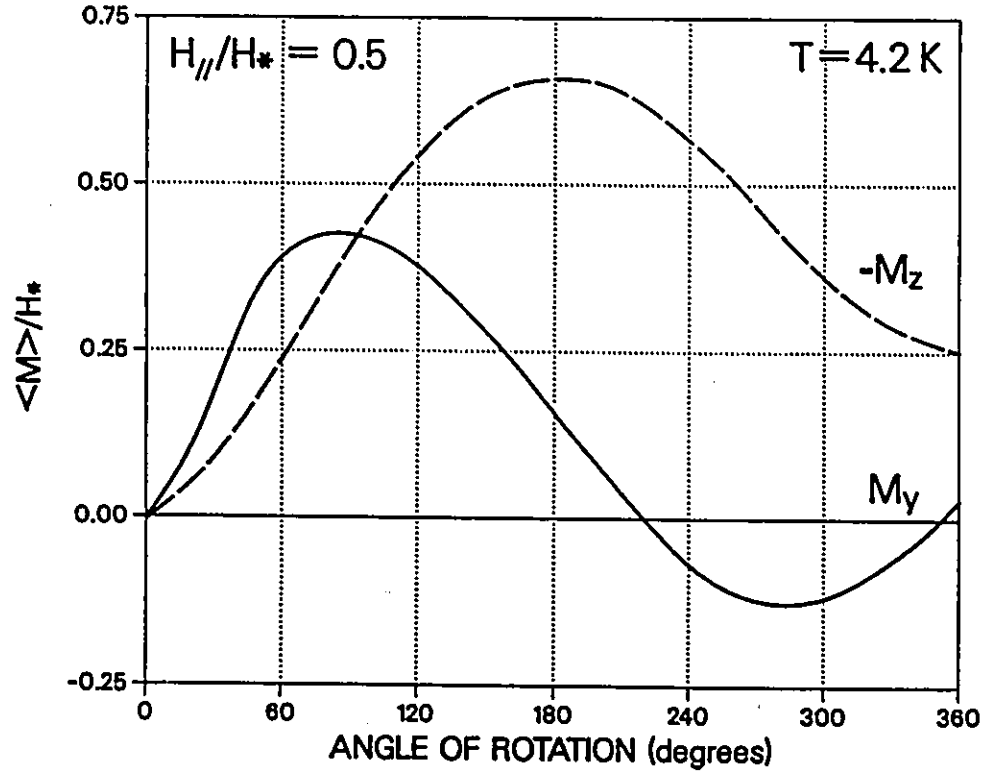

Figure 17: *PbBi* Rotational Curves, for $H_a/H_* = 0.5$.

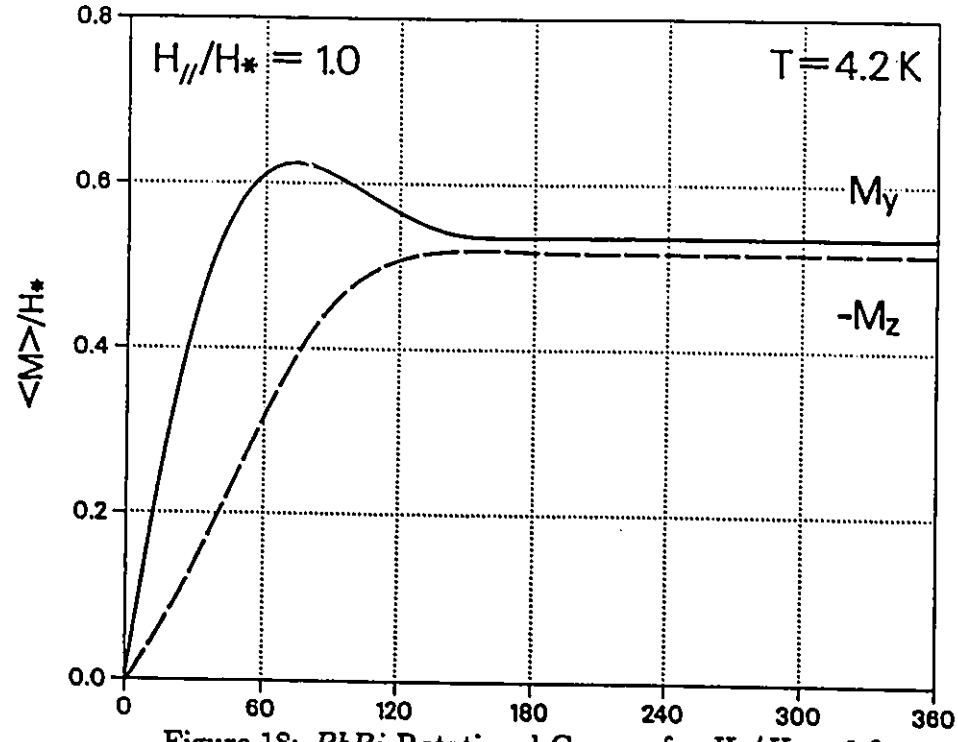

Figure 18: *PbBi* Rotational Curves, for $H_a/H_* = 1.0$.

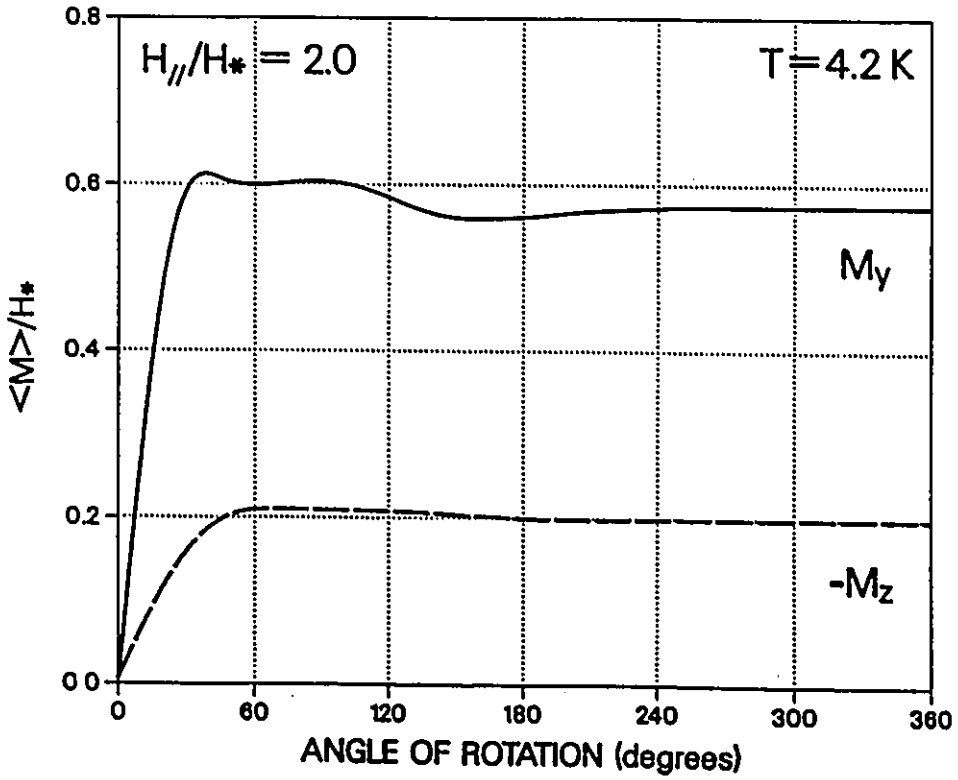

Figure 19: *PbBi* Rotational Curves, for $H_a/H_* = 2.0$.

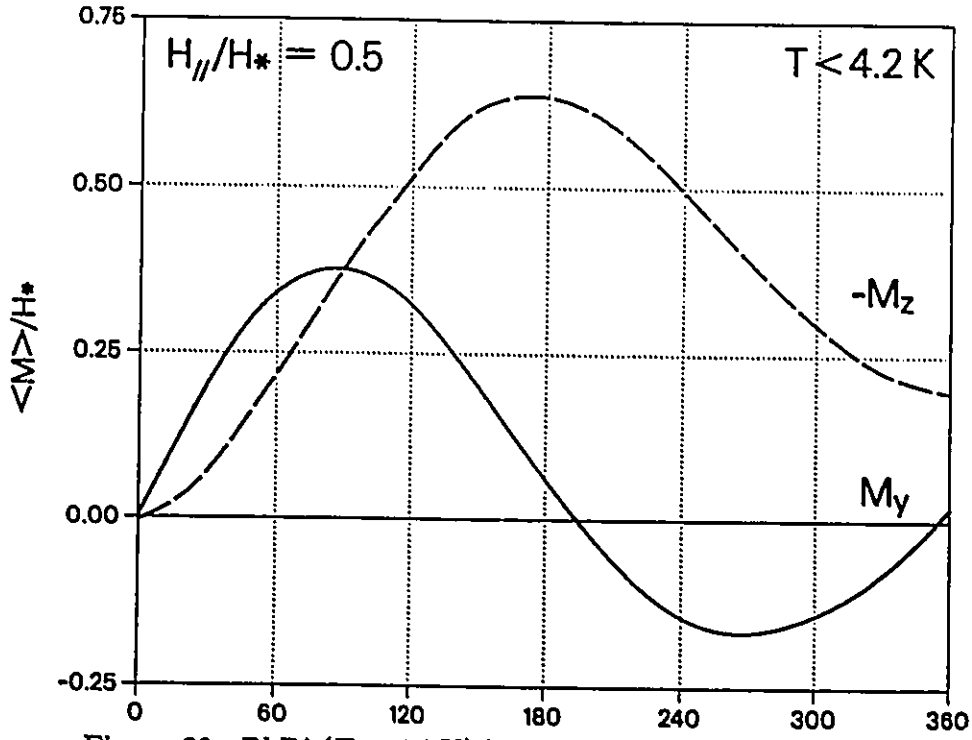

Figure 20: *PbBi* ($T < 4.2K$) Rotational Curves, for $H_a/H_* = 0.5$.

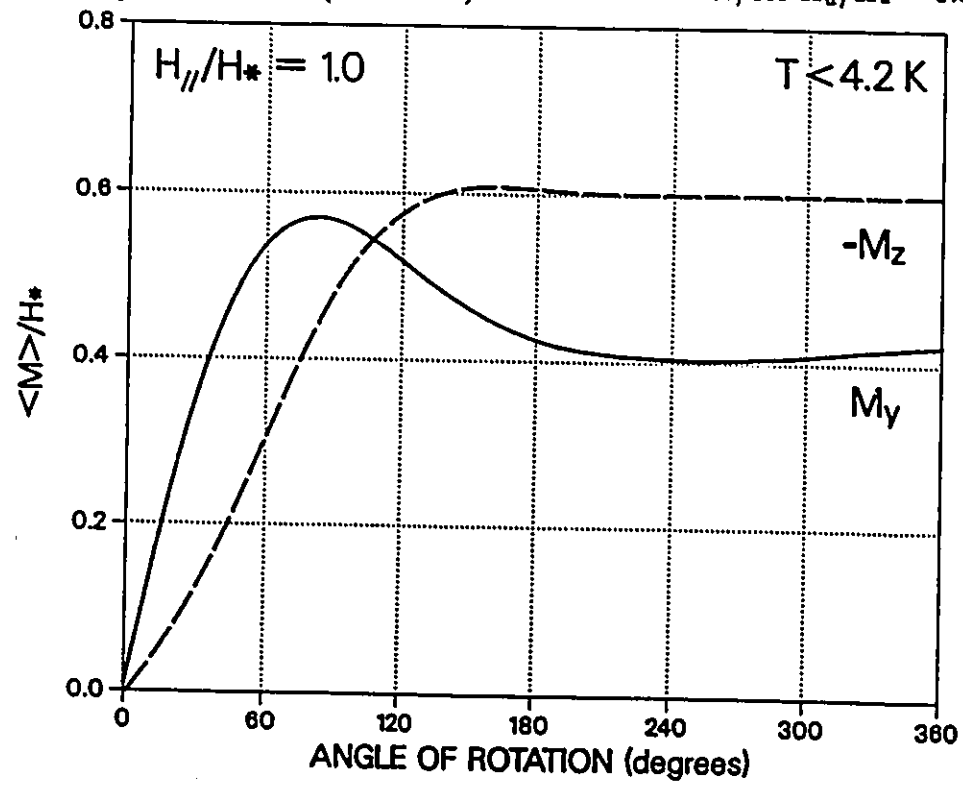

Figure 21: *PbBi* ($T < 4.2K$) Rotational Curves, for $H_a/H_* = 1.0$.

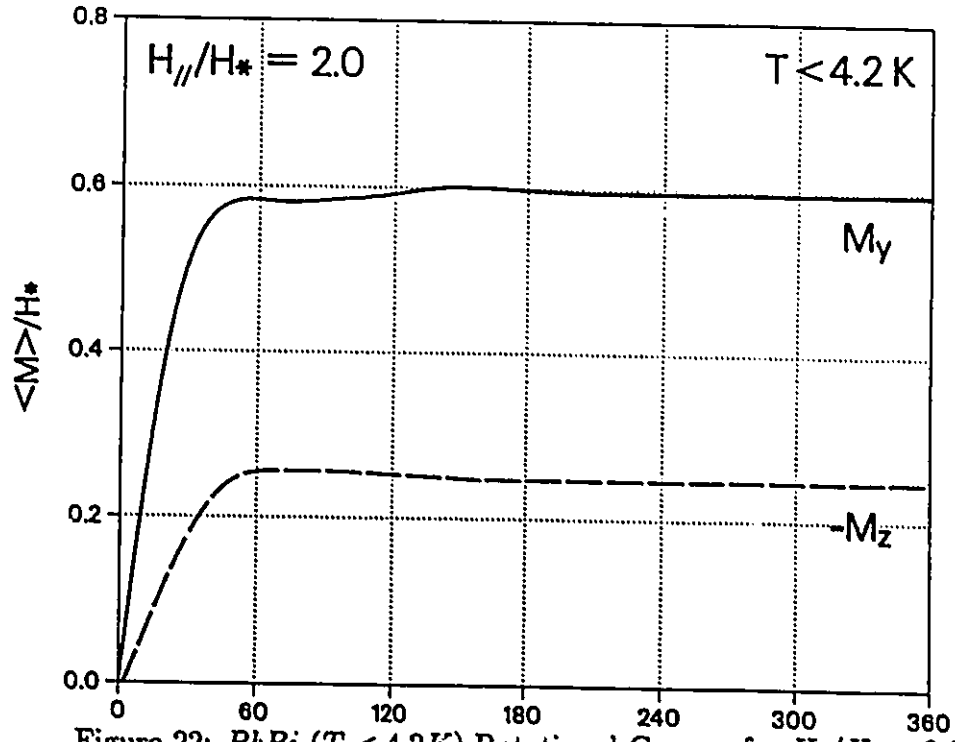

Figure 22: *PbBi* ($T < 4.2K$) Rotational Curves, for $H_a/H_* = 2.0$.

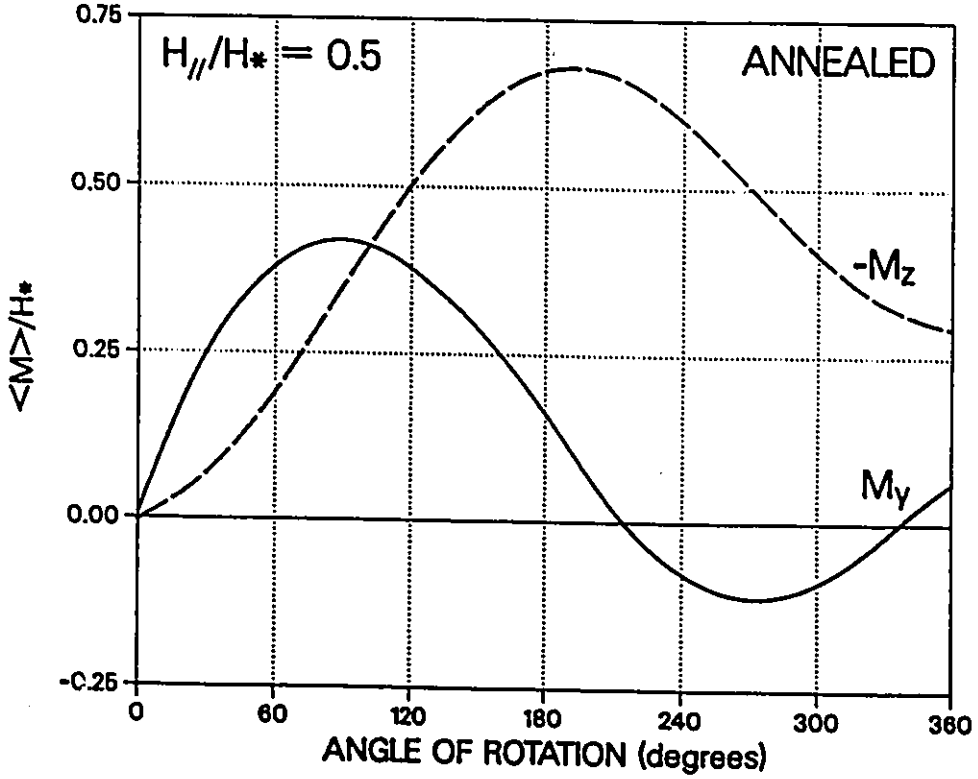

Figure 23: Annealed *PbBi* Rotational Curves, for $H_a/H_* = 0.5$.

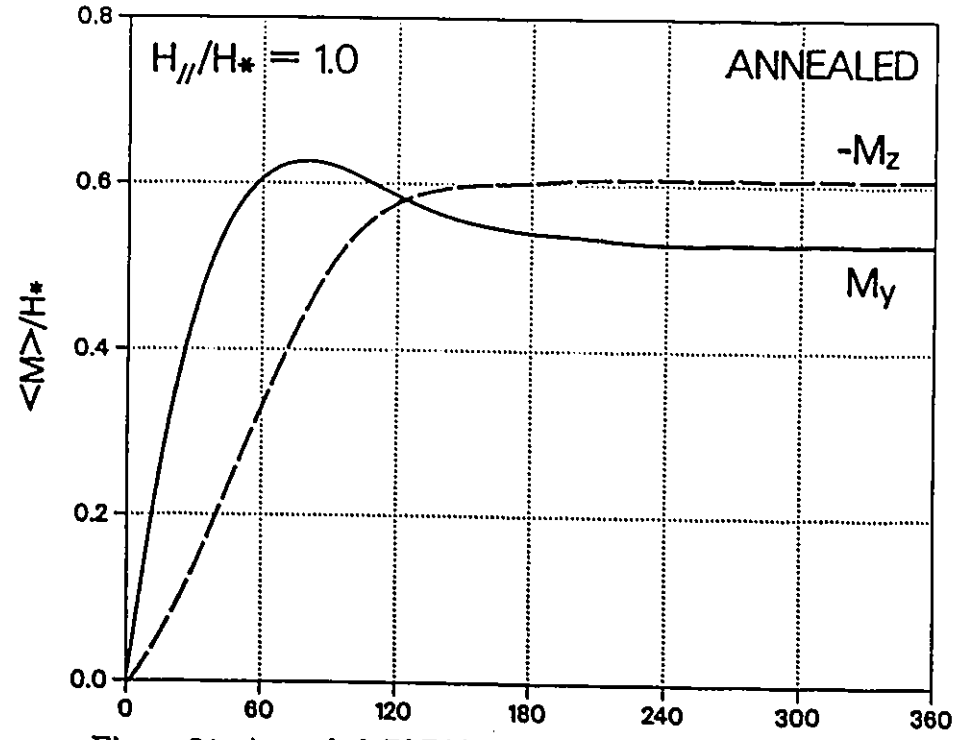

Figure 24: Annealed *PbBi* Rotational Curves, for $H_a/H_* = 1.0$.

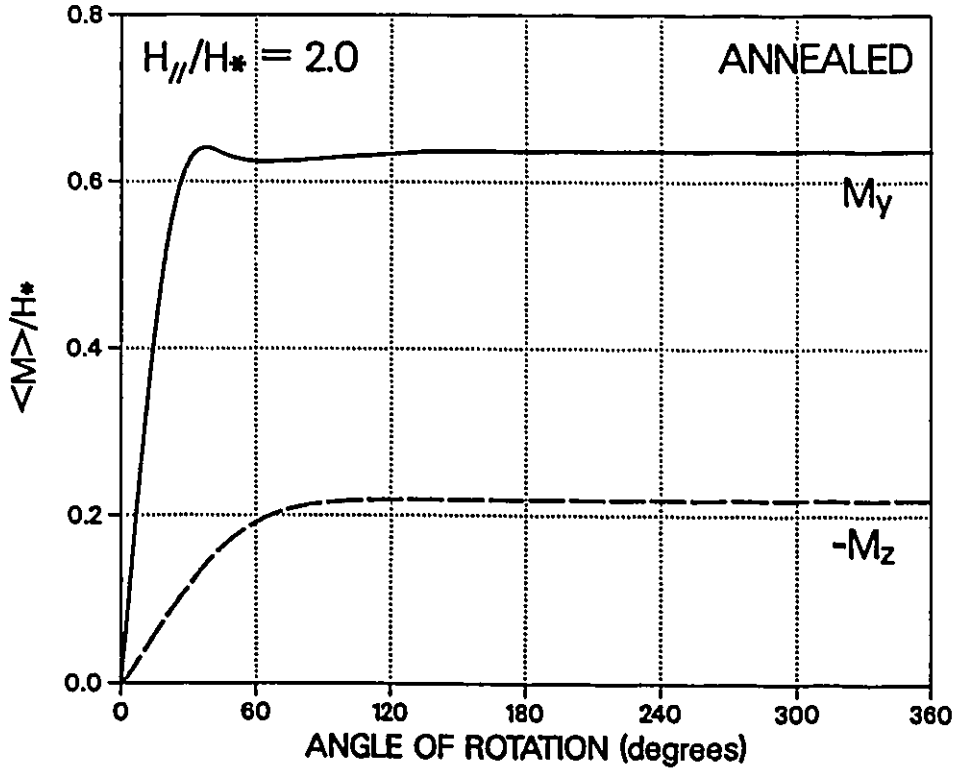

Figure 25: Annealed *PbBi* Rotational Curves, for $H_a/H_* = 2.0$.

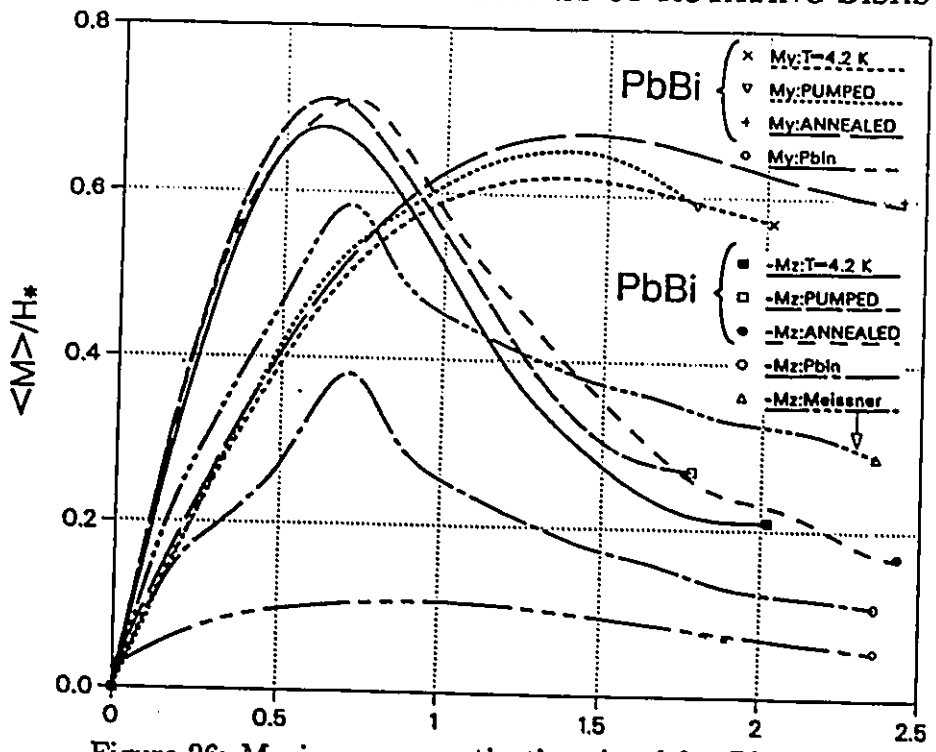

Figure 26: Maximum magnetization signal for *PbBi* and *PbIn*.

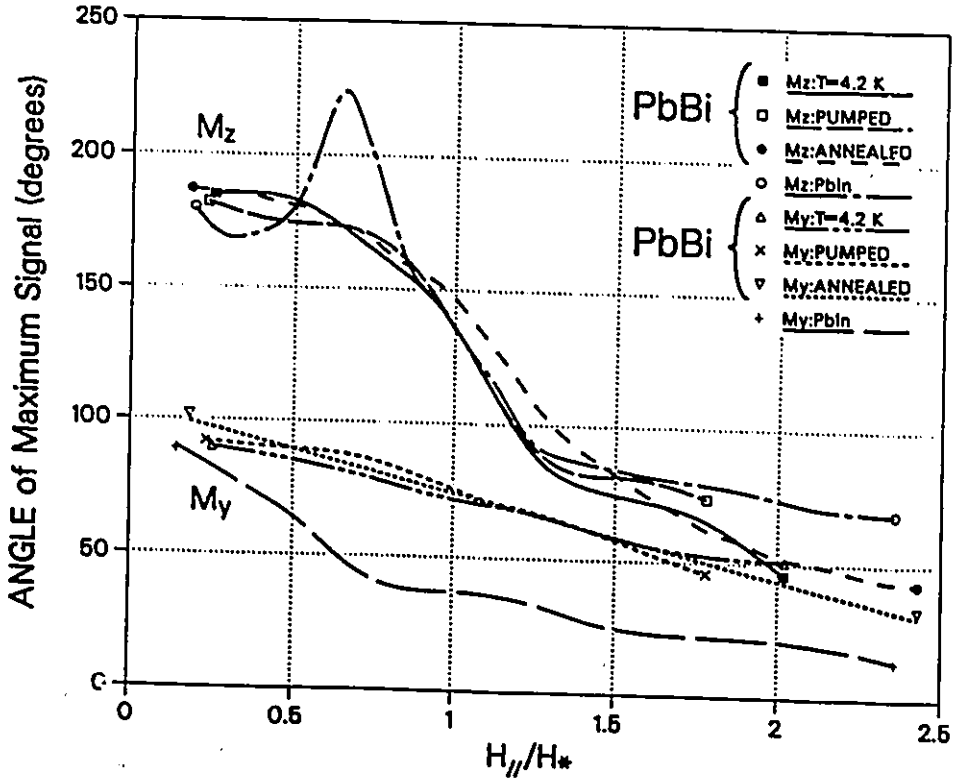

Figure 27: Angle of maximum magnetization signal for *PbBi* and *PbIn*.

Chapter 5

THEORETICAL ANALYSIS OF THE ROTATING DISK

5.1 Introduction

To understand the observations reported in the previous chapter, it is perhaps easier to focus on the flux lines and visualize the evolution of their spatial arrangement in the disk, instead of portraying patterns of induced persistent currents. The electric currents and the magnetic fields are related by Maxwell's equation $\nabla \times \vec{B} = \mu_o \vec{j}$. A detailed picture of one quantity leads to an understanding of the other.

5.2 General Background

It is useful to outline the behaviour expected for a simple extreme situation. Consider a disk where the flux lines are tightly bound to the metallic lattice (having infinite pinning strength), undergoing rotation in a static $\vec{H}_a$. Let the magnetic

flux density in the disk be uniform and equal to the externally applied magnetic induction $|\vec{B}_a|$. Since the magnetic flux ϕ_M, rotates rigidly in unison with the disk, the integrated signals $S_z = \int_0^t \epsilon_z dt$ and $S_y = \int_0^t \epsilon_y dt$, from the orthogonal pick up coils embracing the disk, correspond to $\phi_z = \phi_M(1 - \cos\theta)$ and $\phi_y = \phi_M(1 - \sin\theta)$. Here ϵ_z and ϵ_y denote the emf generated in the respective pick up coils. ϕ_z and ϕ_y, are the z and y components of the magnetic flux, and θ is the angle of rotation. Thus undamped sinusoidal signals with a periodicity of 2π would be observed.

The physical situation envisaged must satisfy the classical boundary conditions on the continuity of $\vec{H}$ across the surfaces of the sample, which for simplicity is regarded as having an infinite diameter, hence viewed as an infinite slab. As the rotation proceeds, a persistent current must flow along the surface of the infinite disk whose surface current density can be written as :

$$\vec{K}_s = -\vec{y}H_a \sin\theta - \vec{z}H_a(1 - \cos\theta) \tag{18}$$

The picture that has just been developed presents a serious problem in the range $H_{c1} < H_a < H_{c2}$ since surface currents of such magnitudes have never been observed in type II superconductors. Further, such surface currents would be difficult to justify theoretically.

Although plausible in the low field range $0 < H_a \leq H_{c1}$, this picture is not in harmony with experimental results. Experimentally, the sinusoidal oscillations initially decay in amplitude to a steady state behaviour. In the steady state, sinusoidal oscillations of diminished amplitude are superimposed on a fixed 'bias' level. Boyer [5], [7] put forward a simple but crucial idea to account for this behaviour and other related features of the observations.

5.3 The Boyer Model

Boyer proposed that, as the rotation of the sample proceeds, a valley develops and grows adjacent to each surface, in the profile of the magnetic flux density. The evolution of this valley during rotation, is displayed schematically in figures 28 and 29.

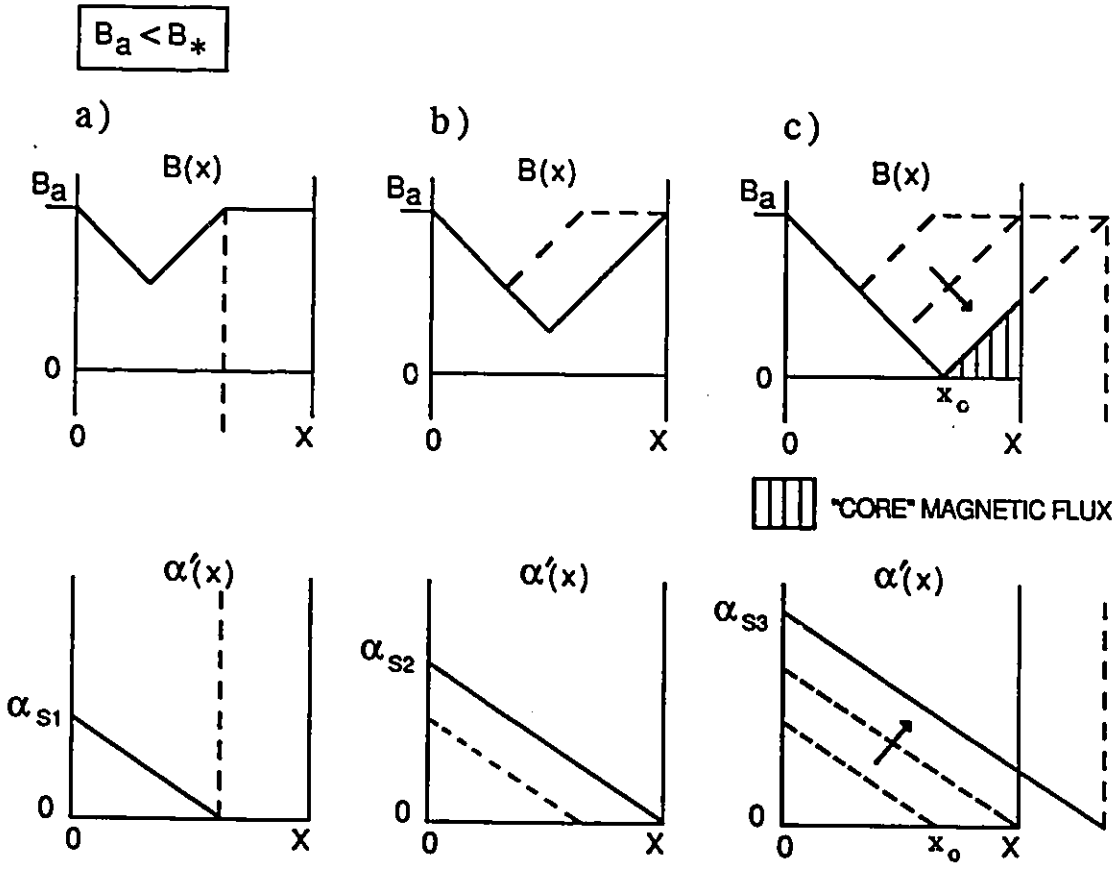

Figure 28: Magnetic flux density profiles, $B_a < B_*$.

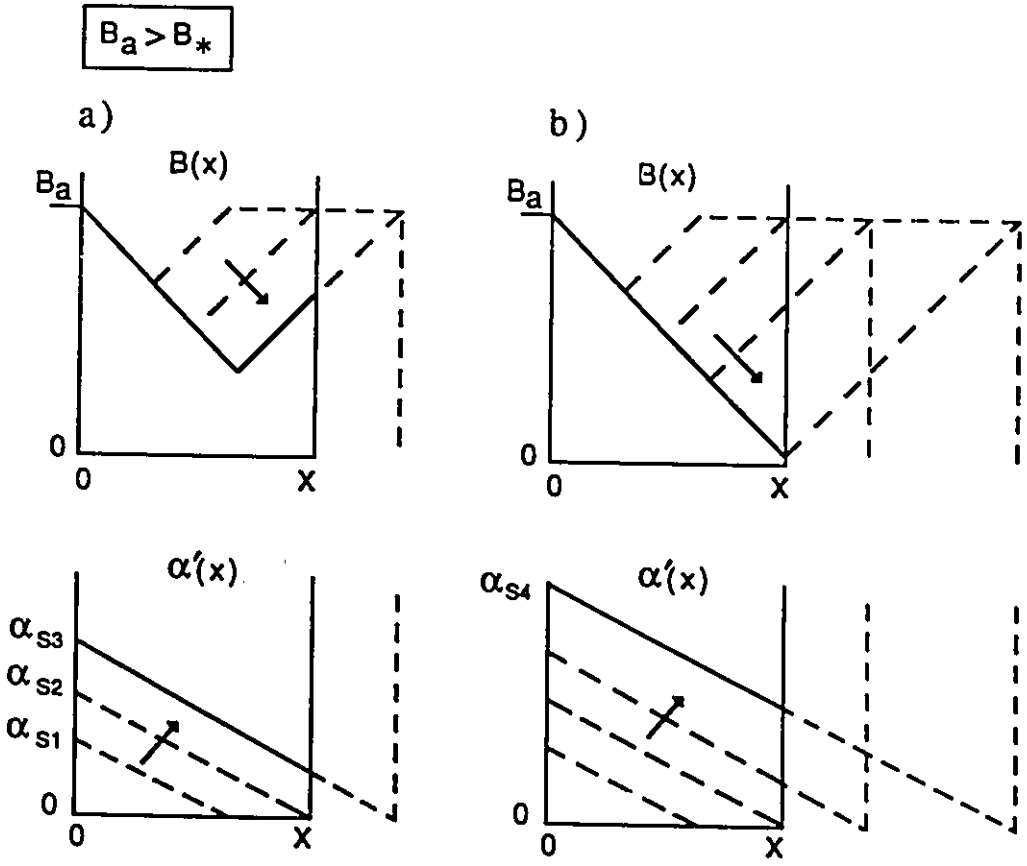

Figure 29: Magnetic flux density profiles, $B_a > B_*$.

Only one half of the width of the specimen is shown in these sketches since the configurations are symmetric with respect to the midplane ($x = X$) of the infinite disk. Also for simplicity, a possible surface current is ignored.

When $H_a < H_*$, the flux density at the bottom of the valley eventually diminishes to zero at some distance x_0, between the surface and the midplane. The distance x_0 will depend on H_a and the slope of $H(x) = B(x)/\mu_0$, hence on $j_{c\perp}$ since by Maxwell's equation $j_{c\perp} = -dH/dx$. Once the bottom of the valley reaches

$B = 0$, the flux permeating the volume between x_0 and the midplane becomes isolated from the outside world. Regardless of its pinning strength, the flux contained in the region will rotate rigidly in step with the disk. It is this core of magnetic flux which is responsible for the low amplitude sinusoidal oscillations of 2π periodicity. The 'background' signals on which the oscillations are superimposed, arise from the configurations of the magnetic flux in the 'shoulders' of the valley (*i.e.* the outer region $0 < x < x_0$).

Clearly in this picture, when $H_a > H_*$, the bottom of the valley descends to a finite magnetic flux density at the midplane of the disk. Under these circumstances no core region is established. Consequently no 'core oscillations' can occur when a steady state configuration is achieved, in accordance with observations.

The picture proposed by Boyer was considered quite revolutionary at the time. Magnetic flux must disappear or be removed in order that the valley may develop. At first glance, it appears that for this to happen the flux lines must migrate out of the specimen against the magnetic flux gradient adjacent to the surface. This disagreed with the prevailing concepts. Clem and his collaborators [8], [13] – [17], [43] – [45] however, showed subsequently that the mechanism of flux line cutting will cause magnetic flux to be consumed and create such valleys in the flux density profile. These ideas are now outlined.

5.4 Flux Line Cutting

The reader is referred to figure 30 which outlines the sequence of events developed in the process of flux cutting.

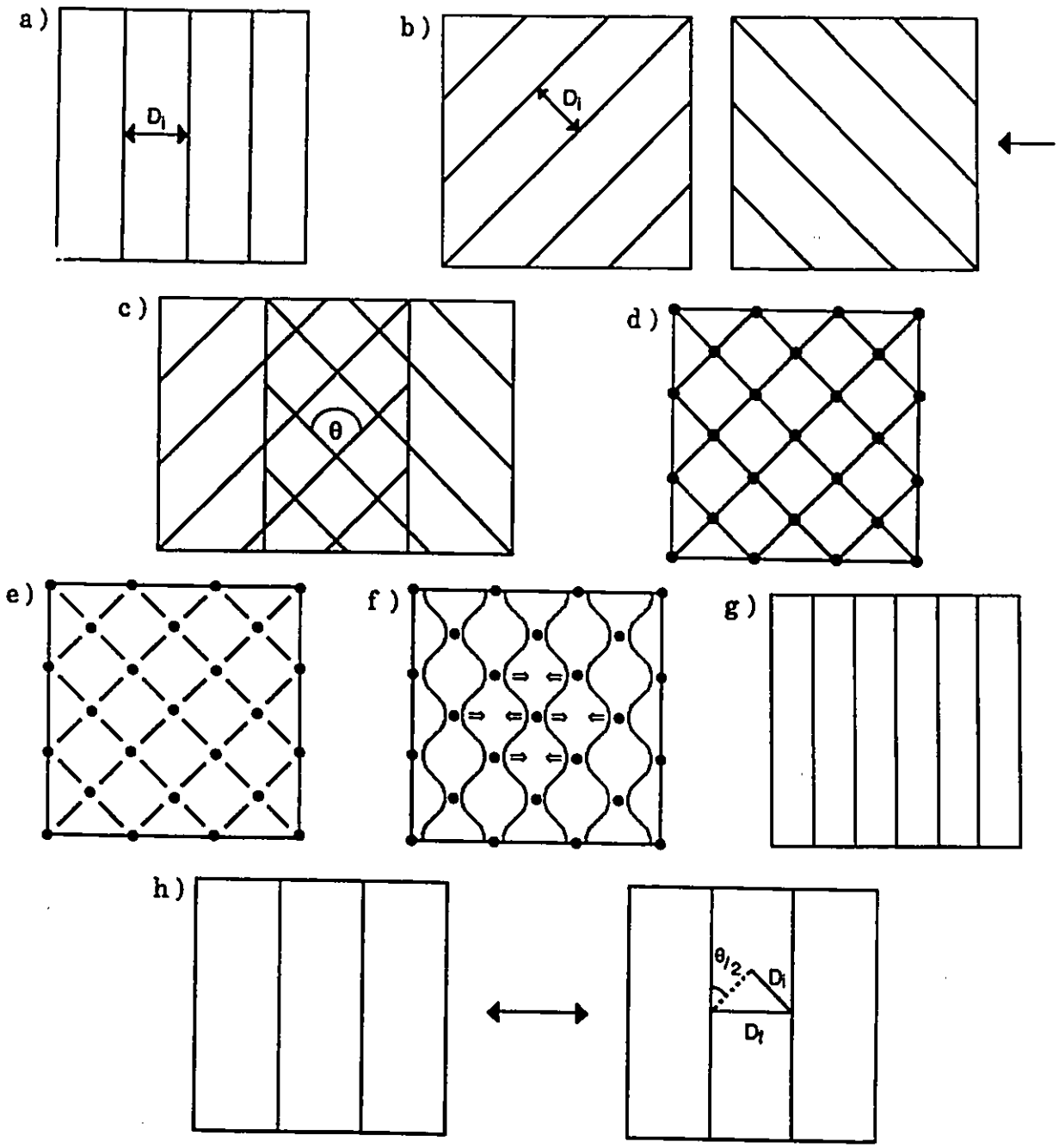

Figure 20: a) Flux lines exist along H_a. b) Sample is rotated and a new series of flux lines is introduced. c) Two planes of vortices merge. d) Cross joining at intersection points. e) Separation at intersection points results in zigzag vortices. f) Vortices straighten. g) Resulting densely packed vortices. h) Two identical planes separate.

The flux line density is taken to be uniform initially and consists of straight parallel quantized flux lines. Since the behaviour is identical at both boundaries, only one of the two surfaces of the disk will be scrutinized. Of specific interest is the sheet of flux lines adjacent to the surface and initially parallel to $\vec{H}_a$. The latter is kept fixed in magnitude while the angle θ (subtended by an arbitrary diameter of the disk and $\vec{H}_a$), is increased. As was indicated earlier, the laws of electromagnetic induction and the continuity of $\vec{B}$ and $\vec{H}$ require that, as the rotation takes place, a persistent current appears along the surface with a component parallel to the sheet of flux lines.

Eventually, at some critical angle θ_c, hence at a critical current density $j_{c//}$, a new sheet of flux lines of density $B = \mu_o H_a$, will nucleate at the surface of the disk. The new and the 'old' sheet of flux lines are sketched side by side in figure 30 b). The new sheet should be visualized as existing a distance Δx above the old one. The former is aligned along $\vec{H}_a$, and the angle subtended by the two sheets is θ_c.

Brandt et al [8], Clem and Yeh [17] have shown that at a critical angle θ_c, the mutual repulsion between parallel sheets of flux lines has vanished. These sheets now experience an attractive interaction which is illustrated in figure 30 c). The two sheets move towards each other under the influence of their mutual attraction, making contact at points of intersection. At these 'points', the flux lines temporarily fuse and form doubly quantized regions (see figure 30 d)). The resulting regions are energetically expensive and this state of affairs cannot persist. Consequently the union breaks up with a segment from the new sheet now attached to a segment from the old sheet as shown schematically in figure 30 e). This process where two lattices of flux lines intersect and cross join is called flux line cutting, or vortex reconnection.

The immediate result of this process is a dense sheet of zig zag flux lines as depicted in figure 30 f). This zig zag configuration is energetically unfavorable and the pattern straightens out to reduce the line tension energy. The ensuing densely packed sheet of lines shown in figure 30 g), separates into two adjacent sheets due to mutual repulsion. These occupy the same volume initially taken up by the two sheets in figure 30 b). These sheets are displayed again side by side in figure 30 h), but in three dimensions, one should be visualized as adjacent to the surface and the other existing deeper inside the material.

It is important to note that D_f the final separation between the flux lines in the resulting two sheets is larger than the original separation D_i, although the total number of flux lines is conserved. The situation just described leads to :

$$D_f = \frac{D_i}{\cos(\theta/2)} \quad . \tag{19}$$

Now the sheet of flux lines closer to the surface is oriented at an angle $\theta = \theta_c/2$ with respect to $\vec{H}_a$. Thus $j_{//} < j_{c//}$, and mutual repulsion expels this sheet from the disk. The magnetic flux density $B = B_a$ existing initially (figure 28 a)) has been reduced by the sequence of events just described, to $B_a \cos(\theta/2)$ along the surface. The sheet of flux lines which remains adjacent to the surface also subtends an angle $\theta = \theta_c/2$ with respect to $\vec{H}_a$, but exists in equilibrium since it also subtends an angle $\theta_c/2$ with respect to the lattice of flux lines in the interior of the disk. As a consequence the repulsive force which they exert is diminished.

After a subsequent incremental rotation $\Delta\theta = \theta_c/2$, the process just described will repeat. Further, the process will incrementally propagate inwards since after the second full flux cutting sequence, the next nearest neighbour sheet of flux lines subtends an angle $\theta = \theta_c$ relative to that existing along the surface. A 'valley' will thus be gouged into the lattice of flux lines by the process of flux line cutting.

According to Clem et al, flux cutting consumes magnetic flux but conserves the total number of flux lines. The straightening or shortening of the flux lines (see figure 30 f)) is the mechanism responsible for this disappearance of magnetic flux. In another perspective, one can visualize that the transverse components of the flux lines have undergone mutual annihilation as the configuration evolved from that depicted in figure 30 d) to that depicted in 30 g).

The simple idea proposed by Boyer, that a valley appears and grows in the flux density profile as the disk is rotated, thus acquired legitimacy and a detailed explanation. The Boyer picture is now explored quantitatively and mathematically to account for the observations.

5.5 Evolution of the Boyer Valley

It must be emphasized that the essential ingredient in the qualitative description of the phenomena under rotation is the appearance and expansion of a valley in the profile of magnetic flux density. This will be labelled as the Boyer valley. The physics which govern the growth and structure of this valley is now explored.

For simplicity, the possible existence of a persistent current density $\vec{K}_s$ is temporarily ignored. Consequently the magnetic flux density is regarded as continuous, both in magnitude and orientation across the surface of the disk. Stated mathematically, $\vec{B}(x=0) = \mu_o \vec{H}_a$ and $\mid \vec{B}(x=0) \mid = \mid \mu_o \vec{H}_a \mid$.

Let x_v denote the distance between the surface of the disk and the bottom of the adjacent valley and x_b, the distance of the interior limit of the valley from the adjacent surface. Also for convenience, only the valley between the surface of the the disk situated at $x = 0$ and its midplane situated at $x = X$ will be explored.

The use of the words left and right will always refer to this valley.

Pursuing concepts current at the time, previous workers in our laboratory (Boyer, Cave and Fillion) considered that the flux line lattice occupying the volume between the bottom of the valley and the midplane ($x_v < x < X$), to have rotated rigidly with the disk. Consequently the flux lines in this region are directed at an angle θ, the angle through which the disk is rotated with respect to $\vec{H}_a$.

At this juncture Maxwell's equation $\nabla \times \vec{B} = \mu_o \vec{j}$ is introduced in the coordinate system of the magnetic flux density $\vec{B}(x)$, instead of the laboratory framework of reference. For planar geometry, Maxwell's equation reads :

$$\frac{dB}{dx} = -\mu_o j_\perp \tag{20}$$

and

$$B\frac{d\alpha}{dx} = \mu_o j_{//} \tag{21}$$

where α denotes the direction of the local magnetic flux density (the flux lines) with respect to the z axis (see figure 31).

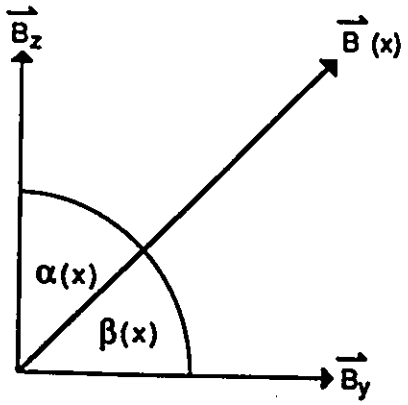

Figure 31: Geometry of Parameters.

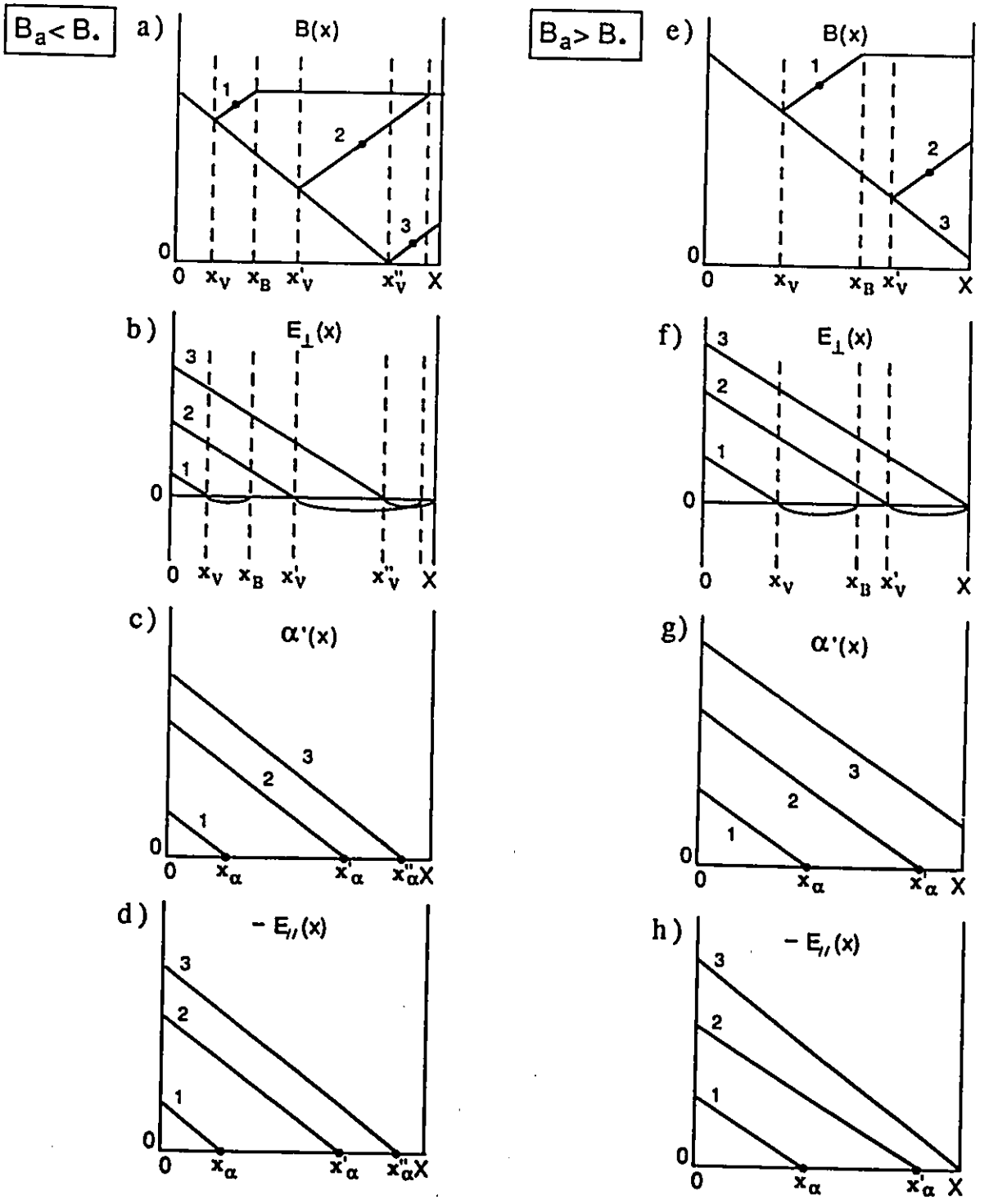

Figure 32: Evolution of $B, \alpha, E_{//}$ and $E_{\perp}$ profiles.

Thus, $j_{//} = 0$ to the right of x_v since the flux lines are all taken to have the same direction $\alpha = \theta$ in this volume. Further, in order that the right hand slope of the valley migrate inwards (see figure 28), it is necessary that the flux lines (which need to be removed) be transferred to the left of x_v. For this to occur in the context of the critical state idea, the current density $j_\perp$, must infinitesimally exceed $j_{c\perp}$ (the critical current density for depinning). Since the flux lines removed from the right and transferred to the left of x_v (the valley bottom), were thought to be ejected from the disk, they must also migrate across the region $0 < x < x_v$, hence surmount pinning obstacles.

Thus $j_\perp$ must also infinitesimally exceed $j_{c\perp}$ in this region. For these reasons, equation 20 now reads :

$$\frac{dB}{dx} = -\mu_o j_{c\perp} \tag{22}$$

throughout the valley.

Boyer et al assumed that the flux lines to the left of x_v did not rotate rigidly with the disk, but lagged behind it nonuniformly with the spatial variation of orientation from $\theta = 0$ to $\alpha = \theta$ spanning the region $0 < x < x_v$. Consequently, the angle between adjacent sheets of flux lines is assumed critical, thus $j_{//} = j_{c//}$, and equation 21 reads :

$$B\frac{d\alpha}{dx} = \mu_o j_{c//}. \tag{23}$$

Regarding $B(x)$ and $j_{c//}(B(x))$ as already specified, this expression governs the direction of the flux line distribution (the $\alpha(x)$ profile). In the sketches presented (such as figure 28), it is more convenient to depict $\alpha'(x)$ instead of $\alpha(x)$ where :

$$\alpha'(x) = \theta - \alpha(x) \tag{24}$$

Recall that θ is the angle through which the disk has been rotated. Thus at the surface $\alpha_S = \alpha'(0) = \theta$.

In brief, Boyer et al stipulated that, *(i)* the flux lines were simultaneously undergoing depinning ($j_\perp \geq j_{c\perp}$) and cutting ($j_{//} \geq j_{c//}$) on the left hand side of the valley, and *(ii)* only depinning on the right hand slope of the valley with $j_{//} = 0$, hence $\alpha'(x) = 0$ in that region. Using the terminology subsequently proposed by Clem et al, the left hand side of the valley is labelled a flux cutting–transport zone (CT zone), and the right hand slope, a pure flux transport zone (T zone).

Exploiting the picture just described and introducing simple analytic expressions for $j_{c\perp}(B)$ and $j_{c//}(B)$ in equations 22 and 23, Boyer [5], [6] and Cave [10] reproduced all of their wide assortment of observations surprisingly well both qualitatively and quantitatively. Application of this model also showed good agreement with our data.

However Clem has correctly pointed out that as the evolution of the valley takes place, the electric field $\vec{E}_\perp(x)$, generated transverse to the flux line density $\vec{B}(x)$, will be directed opposite to $\vec{j}_\perp(x)$ in some portions of the left hand side of the valley. This is not physically plausible since it implies that, in these regions where the 'wrong' sign occurs, energy is being generated instead of dissipated.

It can be argued that the appropriate condition which needs to be satisfied is the classical requirement that the angle ψ subtended by the total electric field :

$$\vec{E} = \hat{\alpha} E_{//} + \hat{\beta} E_\perp \tag{25}$$

and the total current density :

$$\vec{j} = \hat{\alpha} j_{//} + \hat{\beta} j_\perp \tag{26}$$

must be less than 90°, ensuring that energy is being dissipated rather than created. Here, $\hat{\alpha}$ and $\hat{\beta}$ are unit vectors parallel and perpendicular to $\vec{B}$ (see figure 31). $E_{//}$ is the electric field parallel to $\vec{B}$. However, calculations show that under some

circumstances the Boyer ansatz leads to violations of this more general criterion, in some small segments of the left hand side of the valley. The Boyer stipulation that the right hand slope of the valley is a pure transport zone where $j_{//} = 0$ ($\alpha(x) = \theta$) must therefore be regarded only as a useful approximation.

5.6 Our Ansatz

In light of the foregoing objection, feature of the Boyer model which causes the problem of the wrong sign for $E_\perp$ in some region, is amended. Qualitative considerations indicate that this problem can be eliminated by a shift of the interface between the CT and the T zones towards the interior of the disk along the right hand slope of the valley. It was elected to place this interface at the inner edge of the shoulder of the valley, thus completely eliminating the T zone. Our ansatz constitutes a possible extreme solution.

Calculations show that this stipulation does indeed diminish the frequency of the violations of the sign rule for $E_\perp$ with respect to $j_\perp$, and reduces the size of the forbidden zones when violations occur. Thus our ansatz appears to be an improvement on that of Boyer. Since it occasionally leads to violations of the sign requirement, it cannot be considered the correct answer and must also be viewed as a convenient and useful approximate solution. The sequences of $B(x)$ and $\alpha'(x)$ profiles which occur in this approach are depicted schematically in figures 28 and 29. It is stressed that in our picture, the entire valley shows a simultaneous occurrence of flux cutting ($j_{//} > j_{c//}$) and flux transport or depinning ($j_\perp > j_{c\perp}$), while in the Boyer framework the flux cutting was confined solely to the left hand slope of the valley.

5.7 The Clem Phenomenological Model

Clem and his collaborators have developed a detailed phenomenological model to account for the magnetic phenomena and critical current behaviour in type II superconductors. Features which are required for our analysis and have not been mentioned in this thesis are now explored.

Firstly, the Maxwell-Faraday equation :

$$\nabla \times \vec{E} = -\frac{\partial \vec{B}}{\partial t} \tag{27}$$

is formulated in the coordinate frame of the magnetic flux density. Thus for planar geometry, equation 27 now reads :

$$\frac{\partial B}{\partial t} = -\frac{\partial E_{\perp}}{\partial x} - E_{//}\frac{\partial \alpha}{\partial x}, \qquad \text{and} \qquad B\frac{\partial \alpha}{\partial t} = \frac{\partial E_{//}}{\partial x} - E_{\perp}\frac{\partial \alpha}{\partial x} \tag{28}$$

where $E_{//}$ and $E_{\perp}$ denote the components of the electric field parallel and perpendicular to $\vec{B}(x)$. These electric fields are generated when the magnitude and/or the orientation of $\vec{B}(x)$ change.

The classical requirement that $E_{\perp}(x)$ and $E_{//}(x)$ be continuous must be satisfied by the solutions to equation 28. Further, Clem stipulates that wherever an electric field appears :

$$E_{//}j_{//} > 0, \qquad \text{and} \qquad E_{\perp}j_{\perp} > 0 \tag{29}$$

since flux cutting and flux displacement separately dissipate energy. This requirement is more stringent than the standard exigency that, in a dissipative system, $\vec{E}$ and $\vec{j}$ subtend an angle less than 90°.

A boundary condition that the electric field must vanish at the midplane of the disk, is introduced by symmetry. Stated mathematically, this reads :

$$E_{//}(x = X) = 0, \qquad \text{and} \qquad E_{\perp}(x = X) = 0 \tag{30}$$

The model envisages and allows three types of active regions.

- **Pure Flux Transport Zones (T zones)**, where :

$$j_\perp \geq j_{c\perp}, \quad 0 \leq j_{//} < j_{c//}, \quad E_\perp j_\perp > 0, \quad \text{and} \quad E_{//} = 0.$$

  In this type of zone, the flux lines experience depinning and displacement only. The magnetic flux density will increase (decrease) with time if a net flux is entering (leaving) the region. It is stressed that a current density $j_{//}$ can exist in a T zone, but that $j_{//}$ must be less than $j_{c//}$. This will occur when a region where the flux lines are not unidirectional ($\alpha(x)$ is not uniform), is allowed to expand (to decompress). The latter situation was examined in some detail by Lorrain et al [40].

- **Pure Flux Cutting Zones (C zones)**, where :

$$j_{//} \geq j_{c//}, \quad 0 \leq j_\perp < j_{c\perp}, \quad E_{//} j_{//} > 0, \quad \text{and} \quad E_\perp = 0.$$

  In this zone the magnetic flux density diminishes with time as flux is consumed by flux line cutting. Perhaps more vital is the fact that in a C zone, a current density $j_\perp$ can exist provided that $j_\perp < j_{c\perp}$. Thus subcritical gradients of magnetic flux density can occur in active regions of type II superconductors. This is an important and novel element in the perspective on these materials, and constitutes a radical departure from the previously accepted framework. Prior to the work of Clem, it was generally believed that $j_\perp$ had to equal or exceed $j_{c\perp}$ whenever the flux configuration was undergoing any changes.

- **Flux Cutting and Flux Transport Zones (CT zones)**, where both processes are simultaneously taking place, hence :

$$j_\perp \geq j_{c\perp}, \quad j_{//} \geq j_{c//}, \quad E_\perp j_\perp > 0, \quad \text{and} \quad E_{//} j_{//} > 0.$$

This type of zone had been assumed to exist by LeBlanc and his collaborators and constituted a pillar of the empirical double critical state model which they proposed and explored.

For completeness, inactive (inert or static) regions can exist where currently no flux migration or flux cutting is taking place. Persistent currents generated during previous activity may be present in such a (now) dormant region. Thus here :

$$0 < j_{\perp} < j_{c\perp}, \quad 0 < j_{//} < j_{c//}, \quad E_{\perp} = 0, \quad \text{and} \quad E_{//} = 0.$$

5.8 Application of the Clem Model

The Clem phenomenological model is now applied to our specific physical situation. Starting with the initial conditions prescribed, the Boyer valley emerges as the solution to Maxwell's coupled equations 20, 21, and 28, which satisfies the physical constraints (which constitute the fabric of the model).

Perez-Gonzales and Clem [45] have pursued a numerical diffusion method to determine the correct sequence of $B(x)$ and $\alpha(x)$ profiles. The relaxation to a satisfactory steady state after each increment of θ, requires several thousand iterations and is beyond our computational capacity. A simpler, perhaps less accurate approach was adopted, which had been developed and successfully exploited by Fillion [20].

In this latter scheme the sequences of $B(x)$ and $\alpha(x)$ profiles (as the Boyer valley evolves) are first assumed to be critical $j_{c\perp}$ and $j_{c//}$ configurations. The profiles of $E_{\perp}(x)$ and $E_{//}(x)$ which ensue from this sequence are computed and examined in the context of the constraints that $E_{\perp} j_{\perp} > 0$ and $E_{//} j_{//} > 0$ must prevail in order that this solution be acceptable. The latter exercise can be incorporated in the

computer program. Subsequently the program prescribes incremental modifications to the profiles until the appropriate constraints are satisfied. This procedure is expedited by solving the appropriate set of coupled equations from the six applicable statements (*i.e.* equations 20 – 23 and 28).

Noting that when a pure cutting zone (C zone) is required, equation 28 must then read :

$$\frac{\partial B}{\partial t} = -E_{//}\frac{\partial \alpha}{\partial x}, \quad \text{and} \quad B\frac{\partial \alpha}{\partial t} = \frac{\partial E_{//}}{\partial x} \tag{31}$$

since $E_\perp = 0$. Similarly when a pure transport zone (T zone) emerges as the appropriate solution for a portion of the profiles, equation 28 must read :

$$\frac{\partial B}{\partial t} = -\frac{\partial E_\perp}{\partial x} \quad \text{and} \quad B\frac{\partial \alpha}{\partial t} = \frac{\partial E_{//}}{\partial x} \tag{32}$$

since $E_{//} = 0$.

Further, in this approach the $B(x)$ and $\alpha(x)$ profiles evolve as the orientation of the disk (θ) is incremented. Hence :

$$\frac{\partial B}{\partial t} = \frac{\partial B}{\partial \theta}\frac{d\theta}{dt} \quad \text{and} \quad \frac{\partial \alpha}{\partial t} = \frac{\partial \alpha}{\partial \theta}\frac{d\theta}{dt} \tag{33}$$

The $d\theta/dt$ term in equations 28, 31 and 32, cancels out since $E_\perp$ and $E_{//}$ scale linearly with this term.

As indicated earlier, simple, physically meaningful analytic expressions for $j_{c\perp}(B)$ and $j_{c//}(B)$ are introduced in these computations.

5.9 Boyer Valley in the Clem Model

The features which emerge from the computations are now outlined.

The events described occur as the rotation of the disk progresses and hence as the Boyer valley evolves, expands and fills the half width of the disk (see figure 32).

First, a narrow C zone appears along the right hand slope of the Boyer valley adjacent to the summit. After an initial expansion, this C zone shrinks and vanishes. The maximum extent of this C zone encompasses only a small fraction of the side of the valley. This C zone becomes a more pronounced feature as H_a/H_* is chosen larger, although this structure is never dominant in the 'landscape'.

After the C zone has vanished, a T zone arises in that same region of the Boyer valley. This T zone expands down the right hand slope of the valley. Two sets of situations must now be considered.

- When $H_a < H_*$, the bottom of the valley descends to the horizontal axis ($B = 0$) and no further changes occur subsequently. *i.e.* a quasi steady state configuration is attained. At this juncture, the T zone has grown to occupy about half of the right hand slope of the valley, hence only a small fraction of the landscape (see figure 32 a)).

- When $H_a > H_*$, the outer boundary of the T zone (denoted as x_α) lies about half way along the right slope of the valley when the valley fills the entire available space symmetrically (see figure 32 e)). Subsequently as the right hand slope of the valley shrinks in size and vanishes, the gap between x_v and x_α diminishes correspondingly, and the T zone (squeezed in the narrow space between x_α and X) also diminishes in extent. The T zone vanishes when the bottom of the valley reaches the midplane and the right hand slope ceases to exist ($x_v = x_\alpha = X$). At this juncture, a quasi steady state is established with the disk occupied by a CT' zone. It is important to note that throughout the events just described, the active region of the specimen (hence the remainder of the volume of the valley) comprises of a CT zone.

5.10 Comparison of the Models

A major point emerges from the previous chronicle. The sophisticated and elaborate Clem phenomenological model yields a sequence of $B(x)$ and $\alpha\,(x)$ profiles, which overall do not differ appreciably with those that follow from our simple ansatz.

This similarity in behaviour is even more dramatic when the final product of these two perspectives is compared. This close correspondence is illustrated in figures 33, 34 and 35 when displaying curves of $< M_y >$ and $< M_z >$ vs θ generated by these two models for $H_a/H_* = 0.5$, 1.0 and 2.0, hence below, at and above the appropriate benchmark. It is evident from inspection how close the corresponding curves for the two models lie and indeed often overlap.

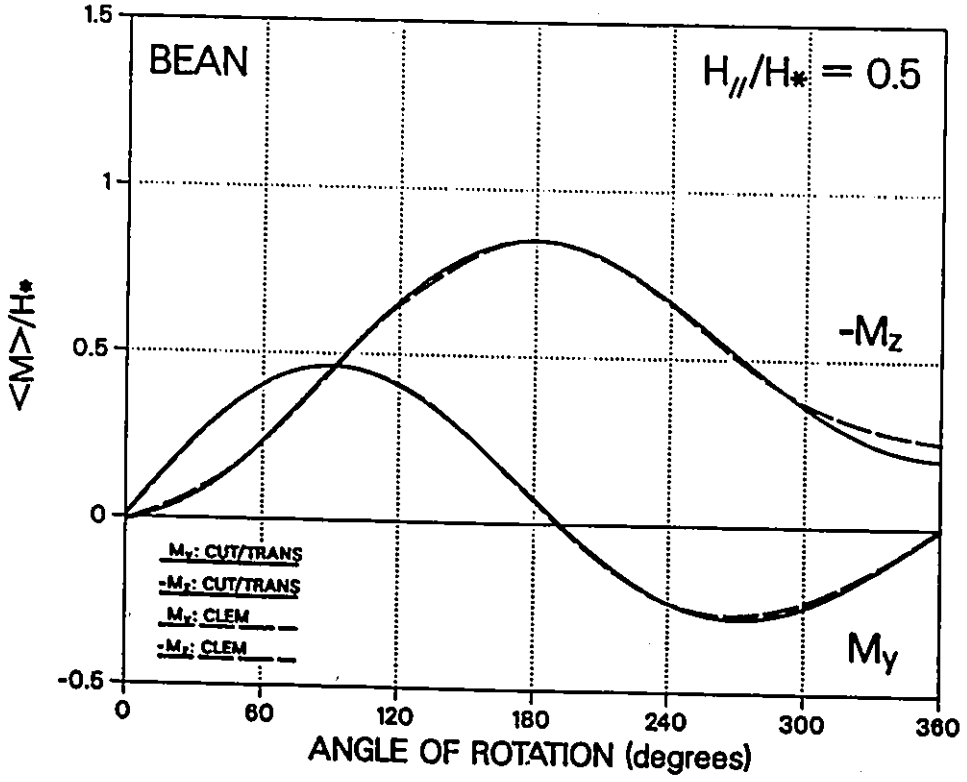

Figure 33: Model Comparison for $H_a/H_* = 0.5$ and $\gamma = 5$.

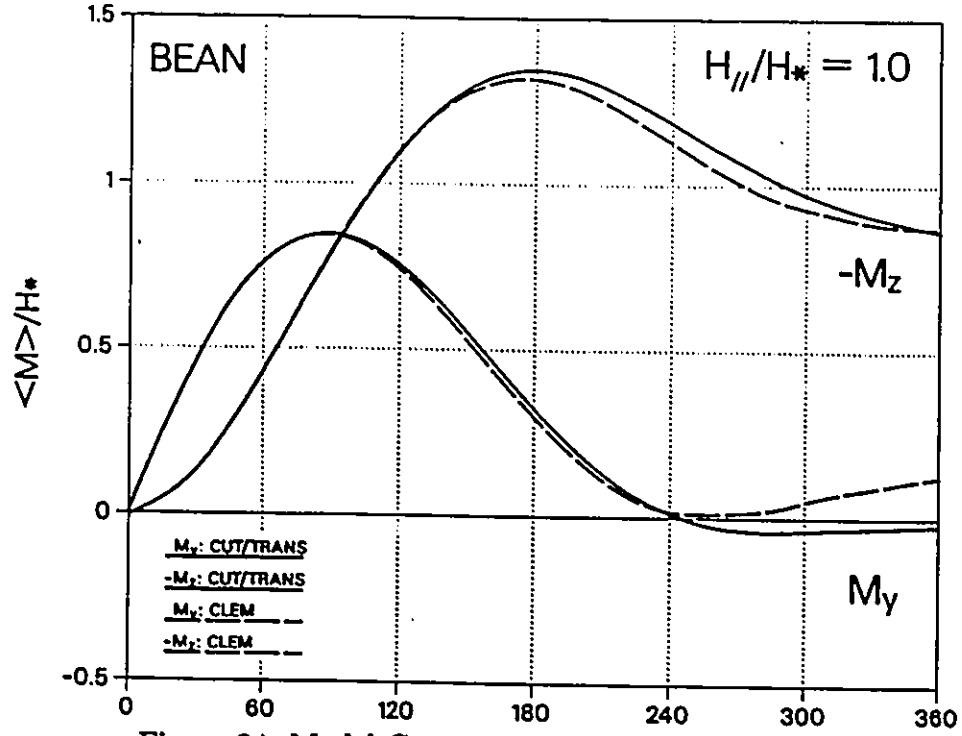

Figure 34: Model Comparison for $H_a/H_* = 1.0$ and $\gamma = 5$.

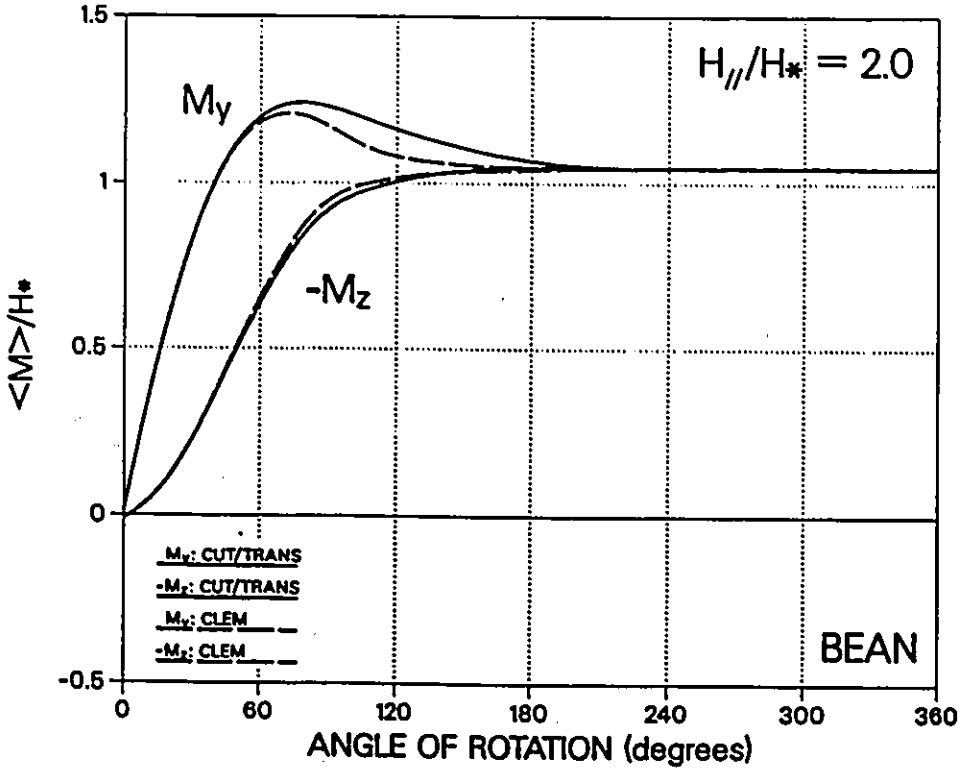

Figure 35: Model Comparison for $H_a/H_* = 2.0$ and $\gamma = 5$.

In view of the fact that the predictions of the Boyer ansatz do not differ appreciably from that generated by our assumption, it is not surprising that our approach yields results which correspond closely to the results of the Clem model. This agreement ensues because in the Clem model, x_v (the outer boundary of the T zone) migrates from the position arbitrarily assigned to it in our model to that chosen by Boyer. Further, when $H_{//} > H_*$, all three choices converge to the same final configuration (where $x_a = x_v = X$) when the quasi steady state is attained. The specimen is not entirely filled by a CT zone in all three models.

The driving and dominant feature in the three interpretations of the phenomena is the Boyer valley. This feature is generated by the physical constraints in the Clem model whereas it is empirically introduced in Boyer's model and in our analysis.

It should be stressed that the computer time and the personal effort demanded by the implementation of the Clem model dwarfs that which is required in the pursuit of our ansatz by several orders of magnitude.

Since the end results appear not to differ significantly, the Clem framework is set aside and our model is used to pursue and compile an extensive survey of the full panorama which beckons exploration.

5.11 Catalogue of Theoretical Curves

Since our ansatz yields results in very good agreement with the predictions of the Clem model, it was deemed useful to use our framework for an extensive survey of a vast domain encompassing a variety of cases. An enterprise of this magnitude exploiting the Clem model would not be feasible with our resources of time and computing power.

Firstly, it is important to explore the effect of varying the relative magnitudes of $j_{c//}$ and $j_{c\perp}$ on the expected phenomena. Secondly it is of great interest to examine the influence of extreme forms for the dependence of $j_{c//}$ and $j_{c\perp}$ on B in the behaviour.

As noted earlier, the Bean ($j_c = \alpha_B$) and Kim ($j_c = \alpha_K/B$) approximations bracket the range of plausible dependences of j_c on B (here H_{c2} is taken as infinite). Following established procedures in the calculations, a linear dependence is introduced on the upper critical field with a factor $(1-(B/B_{c2}))$.

Since there is some evidence that in any given specimen, $j_{c//}$ and $j_{c\perp}$ exhibit a similar dependence on B, behaviour where identical forms for $j_{c//}$ and $j_{c\perp}$ operate, was the choice of focus.

Consequently a spectrum of behaviour was explored where :

$$j_{c\perp} = \alpha_B\left(1-\frac{B}{B_{c2}}\right), \qquad \text{and} \qquad j_{c//} = \gamma\alpha_B\left(1-\frac{B}{B_{c2}}\right) \tag{34}$$

referred to as the Bean combination (or Bean for brevity), and :

$$j_{c\perp} = \frac{\alpha_K}{B}\left(1-\frac{B}{B_{c2}}\right), \qquad \text{and} \qquad j_{c//} = \frac{\gamma\alpha_K}{B}\left(1-\frac{B}{B_{c2}}\right) \tag{35}$$

a combination labelled as Kim for brevity. Thus :

$$\gamma = \frac{j_{c//}}{j_{c\perp}} \tag{36}$$

is a scaling parameter for these two critical currents.

The behaviour predicted using both the Bean and Kim approximations was examined for a range of γ extending from 0.5 to 10.

Figures 36 through 41 illustrate the evolution of $< M_y >$ and $< M_z >$ vs θ generated by our model for the Bean and Kim cases when $H_a/H_* = 0.5$, 1.0 and 2.0, while $\gamma = 2.0$.

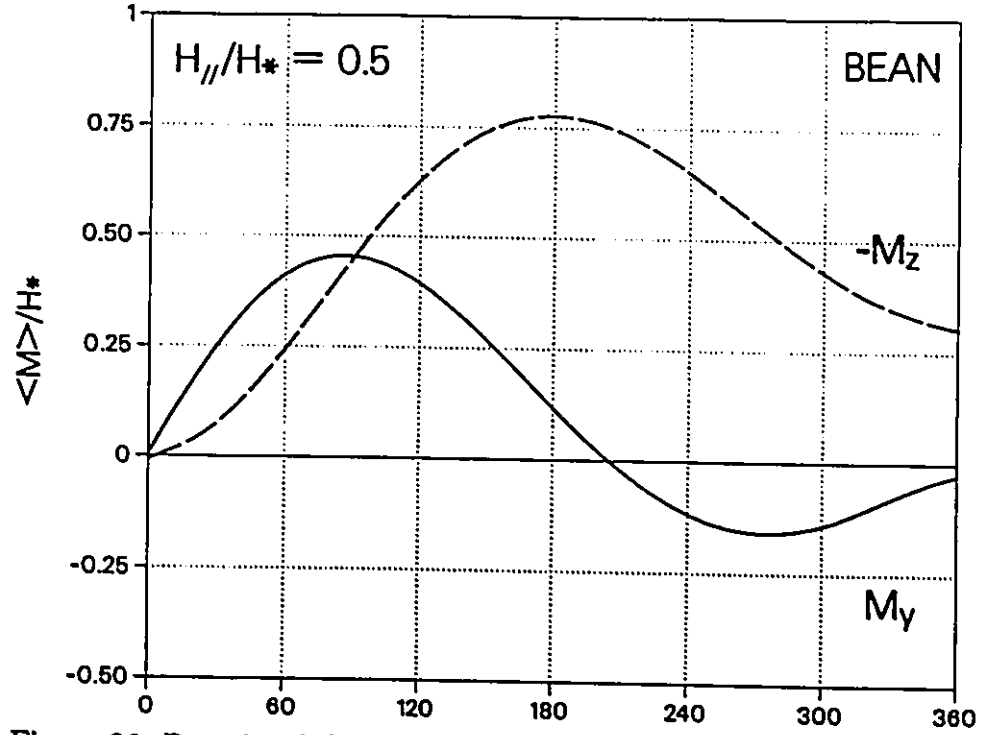

Figure 36: Rotational Curves for $H_a/H_* = 0.5$, $\gamma = 2.0$: Bean Approximation .

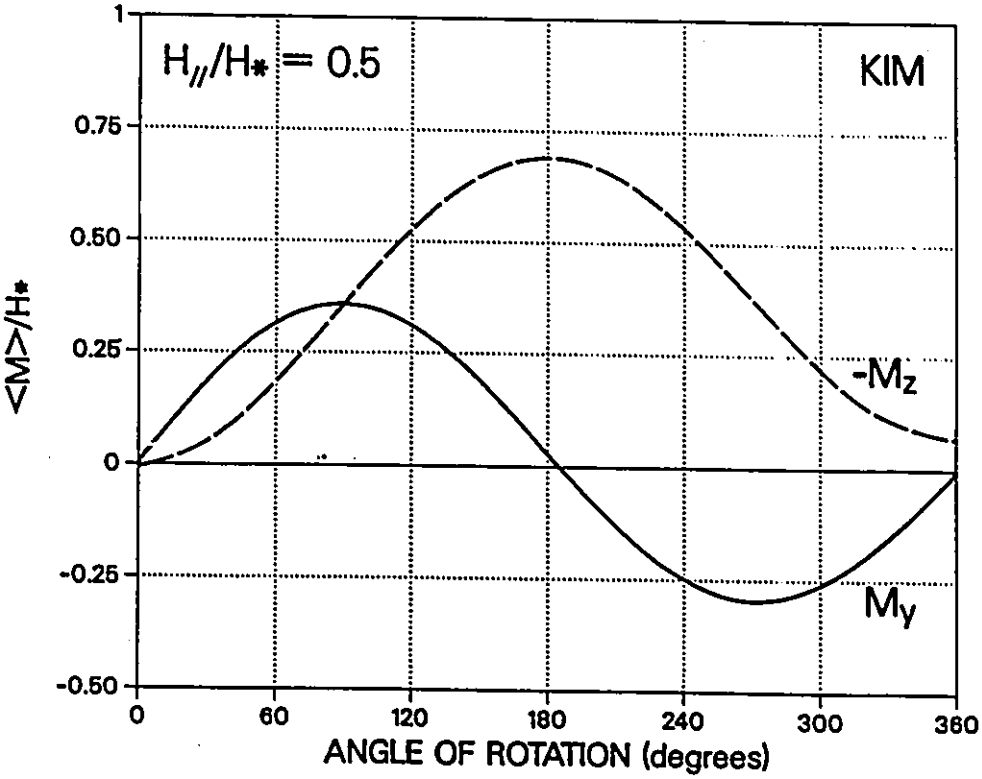

Figure 37: Rotational Curves for $H_a/H_* = 0.5$, $\gamma = 2.0$: Kim Approximation .

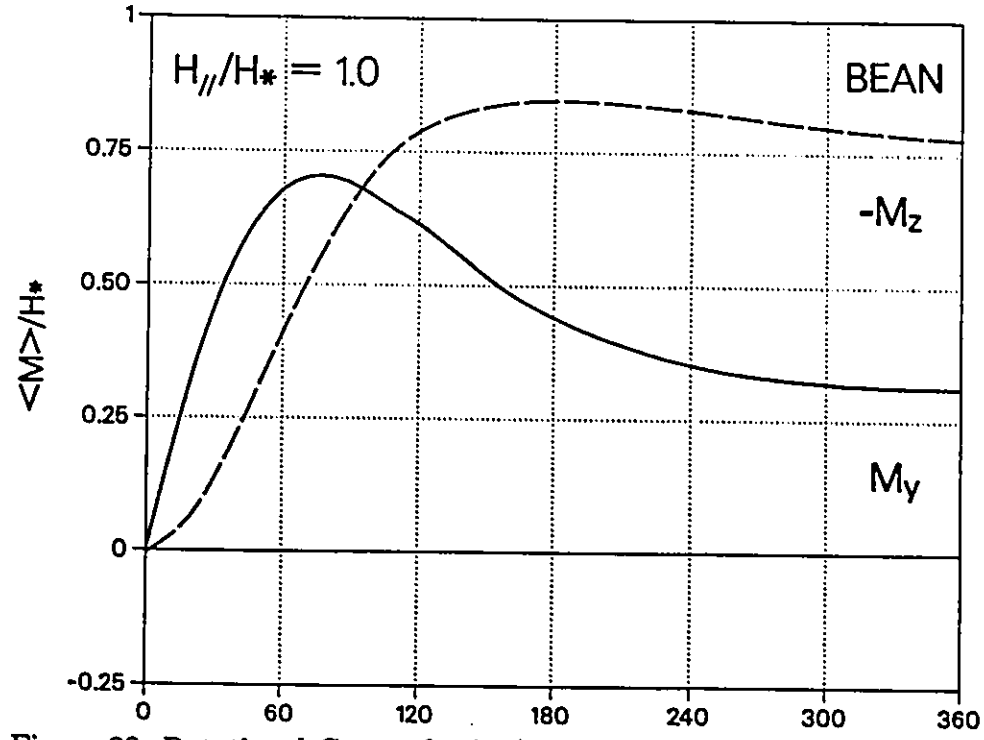

Figure 38: Rotational Curves for $H_a/H_* = 1.0$, $\gamma = 2.0$: Bean Approximation .

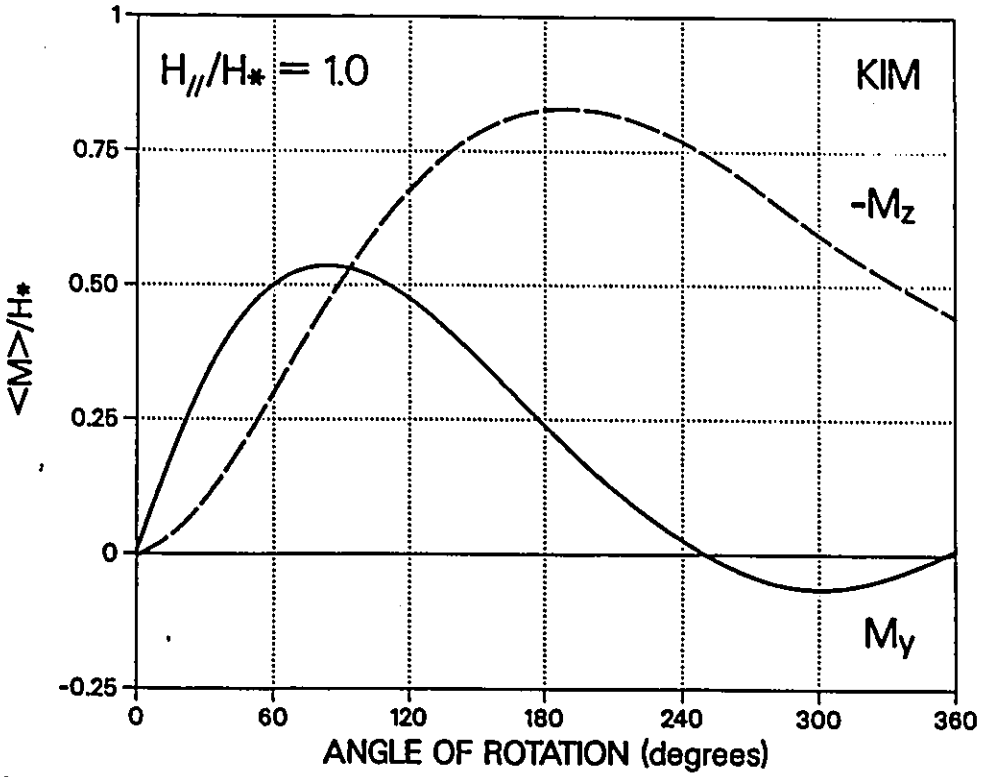

Figure 39: Rotational Curves for $H_a/H_* = 1.0$, $\gamma = 2.0$: Kim Approximation .

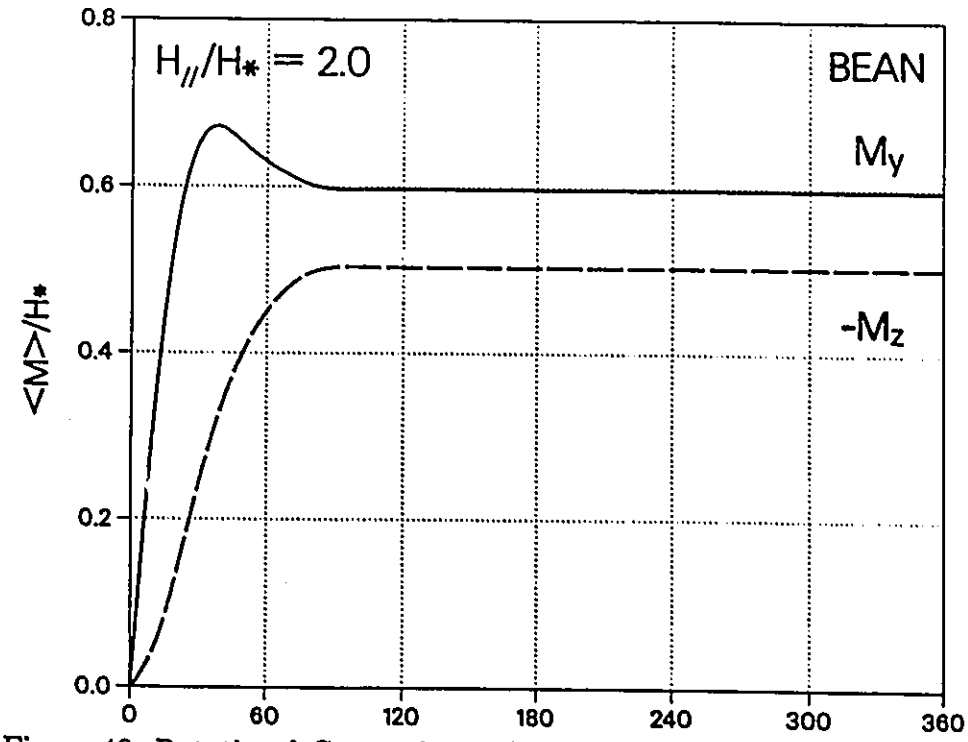

Figure 40: Rotational Curves for $H_a/H_* = 2.0$, $\gamma = 2.0$: Bean Approximation .

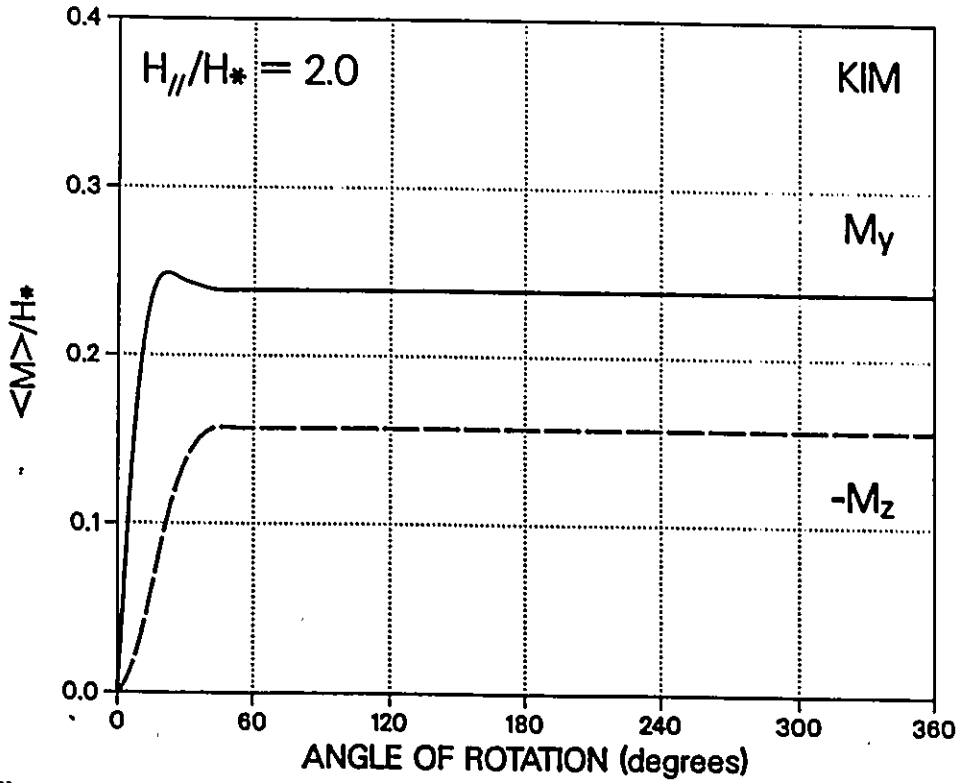

Figure 41: Rotational Curves for $H_a/H_* = 2.0$, $\gamma = 2.0$: Kim Approximation .

These theoretical curves should be compared with each other and with the corresponding experimental curves for $PbIn$ and $PbBi$ presented at the end of chapter 4. The correspondences between such a variety of intricate experimental and theoretical curves is encouraging.

5.12 $< M_y >$ and $< M_z >$ from B(x) and $\alpha(x)$ Profiles

The computational development of the model, whether it be the Clem, Boyer or our version, generates sequences of $B(x)$ and $\alpha(x)$ profiles vs θ for a chosen initial uniform distribution $B_i(x) = B_a$. However these sequences of profiles are not measured directly. The macroscopic quantities readily accessible to measurement are $< M_y >$ and $< M_z >$ vs θ. Consequently the calculated sequences of $B(x)$ and $\alpha(x)$ profiles are introduced in the definitions :

$$\mu_o < M_z >= \left(\frac{1}{X}\int_0^X B_z(x)dx\right) - H_a \tag{37}$$

$$\mu_o < M_y >= \left(\frac{1}{X}\int_0^X B_y(x)dx\right) \tag{38}$$

[where : $B_z(x) = B(x)\cos\alpha(x)$, and $B_y(x) = B(x)\sin\alpha(x)$]

and integrate numerically.

5.13 Theoretical H_*

As seen in chapter 3, the quantity denoted as H_* which could be readily determined by various experimental procedures and criteria, served as a useful measure of pinning strength. H_* is seen as the minimum applied magnetic field which causes the penetration of flux lines to the midplane of the virgin specimen. Figures 28 and 32 depicting the evolution of the Boyer valley show that the $B(x)$ profile visualized to exist at H_* emerges as an important configuration in the behaviour of rotating type II superconductors. Consequently it is not only convenient and useful, but also 'natural' to relate and normalize our theoretical results to this quantity.

It is a straightforward matter to compute H_* numerically for arbitrary dependences of $j_{c\perp}$ on B for planar geometry. For the Bean and Kim approximations H_* can also be readily developed in closed form as is now demonstrated. The critical state concept and Maxwell's equation for planar geometry provide the starting statement. For the Bean approximation :

$$\frac{dH}{dx} = -\alpha_B \left(1 - \frac{H}{H_{c2}}\right) \tag{39}$$

Since $H(x)$ is defined as H_* at $x = 0$ and zero at $x = X$ (or vice versa), the integral form of equation 39 reads :

$$\int_0^{H_*} \frac{dH}{\left(1 - \frac{H}{H_{c2}}\right)} = \alpha_B \int_0^X dx \tag{40}$$

Integrating and rearranging leads to :

$$\frac{H_*}{H_{c2}} = \left[1 - e^{-(\alpha_B X / H_{c2})}\right] \tag{41}$$

Consequently H_{c2} can be chosen relative to the factor $\alpha_B X$ which contains the pinning parameter α_B. In these computations $H_{c2} = 5\alpha_B X$ was arbitrarily chosen,

thus $H_*/\alpha_B X = 0.906$. For H_{c2} taken infinite, equation 40 yields :

$$H_{*\infty} = \alpha_B X \tag{42}$$

Consequently :

$$\frac{H_*}{H_{*\infty}} = 0.906. \tag{43}$$

Proceeding in similar fashion with the Kim approximation, the starting statement reads :

$$\frac{dH}{dx} = -\frac{\alpha_K}{H}\left(1 - \frac{H}{H_{c2}}\right) \tag{44}$$

and the integral reads :

$$\int_0^{H_*} \frac{H dH}{\left(1 - \frac{H}{H_{c2}}\right)} = \alpha_K \int_0^X dx \tag{45}$$

Integrating and rearranging leads to :

$$\frac{H_*}{H_{c2}} + \ln\left[1 - \frac{H_*}{H_{c2}}\right] + \frac{\alpha_K X}{H_{c2}^2} = 0 \tag{46}$$

Taking $H_{c2} = 5\sqrt{\alpha_K X}$ and solving numerically yields :

$$\frac{H_*}{\sqrt{\alpha_K X}} = 1.284. \tag{47}$$

For H_{c2} infinite, equation 44 leads to :

$$H_{*\infty} = \sqrt{2\alpha_K X} \tag{48}$$

Consequently :

$$\frac{H_*}{H_{*\infty}} = 1.284. \tag{49}$$

5.14 Closing Remarks on the Theoretical Curves

Figures 42 through 45 display the behaviour of $< M_z >_{Max}$, $< M_y >_{Max}$, $\theta_{z(Max)}$ and $\theta_{y(Max)}$ versus H_a/H_* for four selected ratios $\gamma\,(= j_{c//}/j_{c\perp}) = 0.5$, 1.0, 2.0 and 5.0, for both the Bean and the Kim combinations of $j_{c//}$ and $j_{c\perp}$. By normalizing the results to H_*, each curve in these graphs encompasses the full spectrum of pinning strength.

A comparison of the appropriate data on any material (normalized to the specific H_* for that specimen) with the theoretical curves displayed in figures 42 through 45 will enable the researcher, *(i)* to estimate the ratio of $j_{c//}$ to $j_{c\perp}$ of the specimen, and *(ii)* to assess where its behaviour falls between the extremes represented by the Bean and Kim approximations.

A comparison of the compilations of data for *PbIn* and *PbBi* displayed in figures 26 and 27 with these theoretical curves suggests that $j_{c//}/j_{c\perp}$ lies between 0.5 and 1.0 for the weak pinning *PbIn* and at approximately 2.0 for the stronger pinning *PbBi*. This indicates that $j_{c//}$ grows somewhat more slowly than the pinning strength in the range of weak to modest pinning since the ratio of H_* of the *PbBi* to that of the *PbIn* is ≈ 7.

It was also determined that the Bean approximations combination leads to a better correspondence with the observations for both the *PbIn* and *PbBi* samples, than the Kim approximation. The Yasukochi approximation, where $j_c = \alpha_Y/B^{1/2}$ (when B_{c2} is infinite), is intermediate in B dependence between the Bean and Kim limits and may therefore better represent the behaviour of the samples.

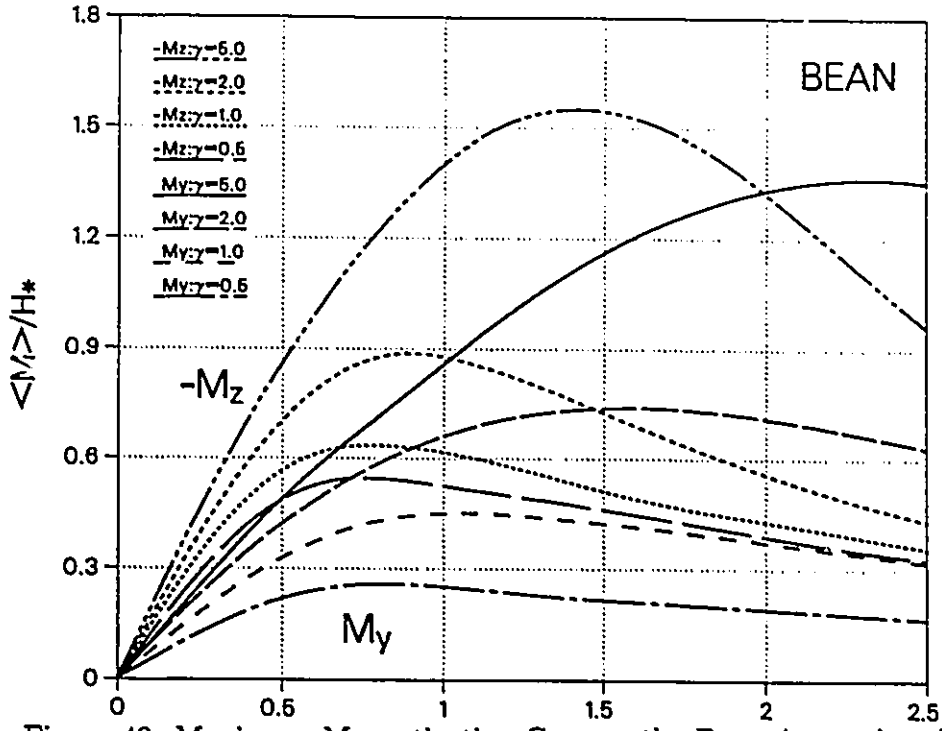

Figure 42: Maximum Magnetization Curves: the Bean Approximation.

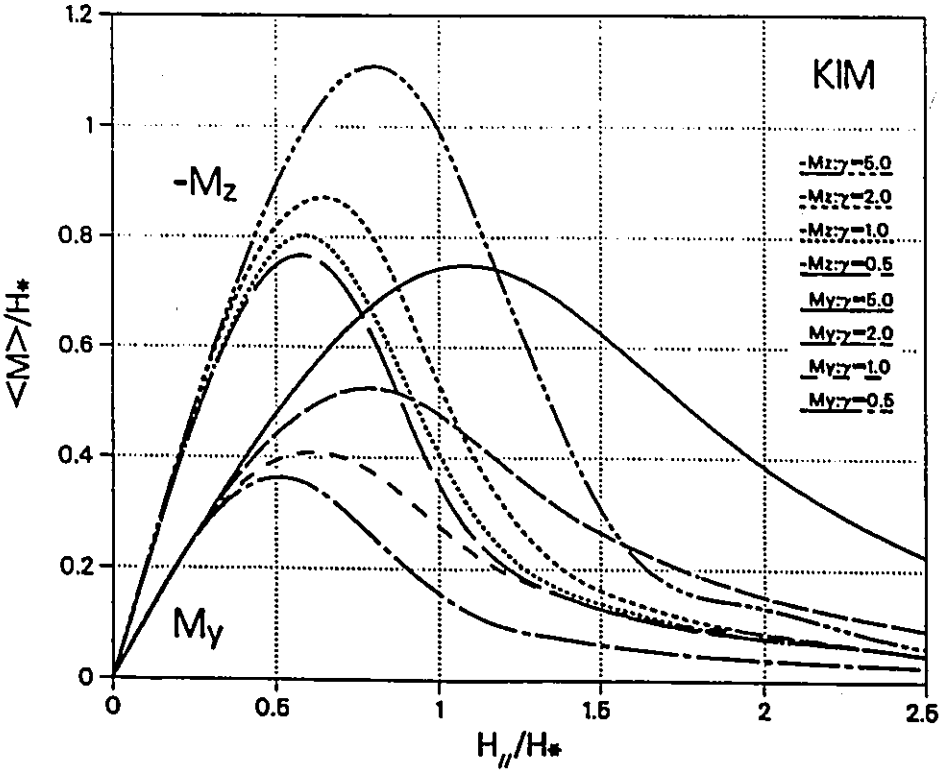

Figure 43: Maximum Magnetization Curves: the Kim Approximation.

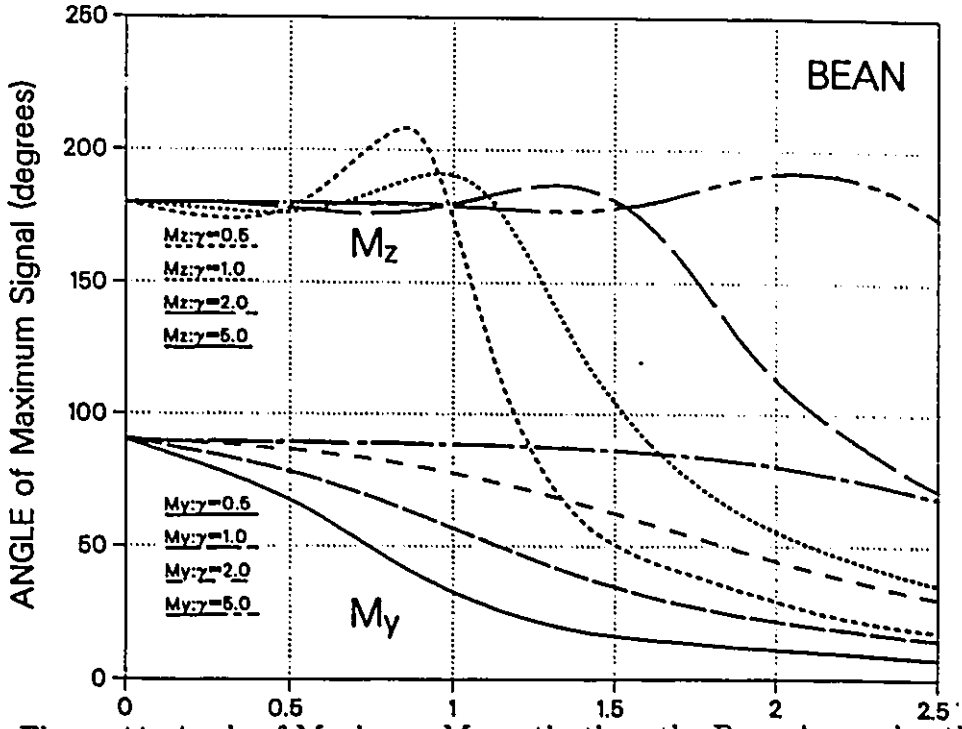

Figure 44: Angle of Maximum Magnetization: the Bean Approximation.

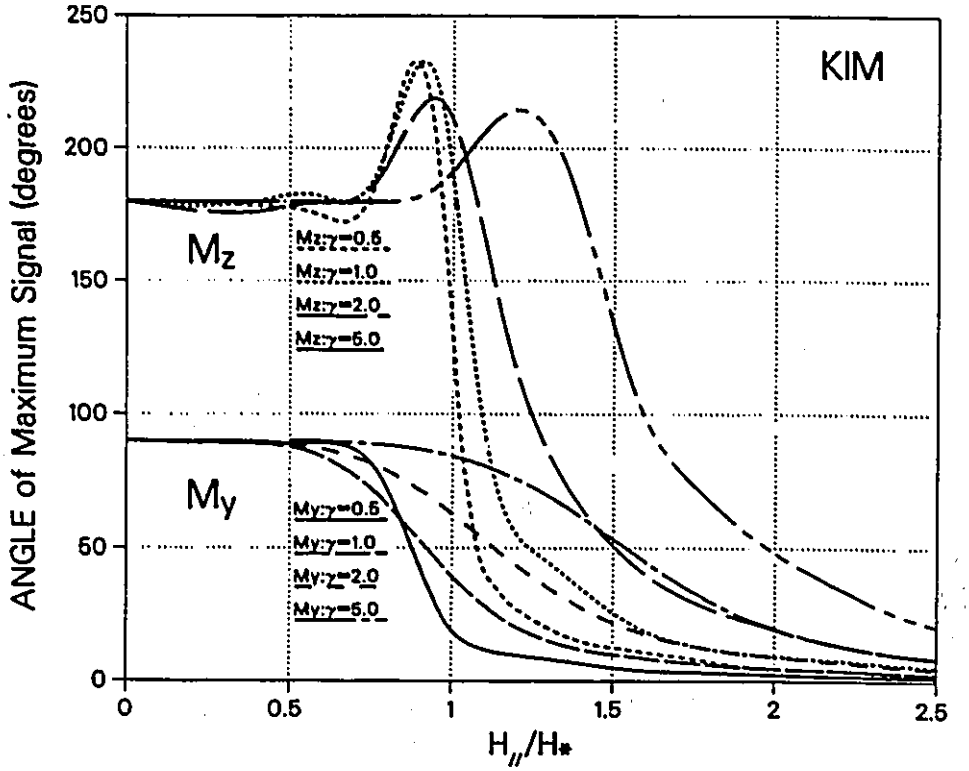

Figure 45: Angle of Maximum Magnetization: the Kim Approximation.

Finally it is noted that the Meissner effect appears to play only a subsidiary role in these phenomena and was ignored in the analysis. Good correspondence is found with observations, provided that the Meissner contribution to $< M_z >$ is simply subtracted from the data. This indicates that the Meissner shielding currents are unaffected by the rotation of the disk and retain their initial equilibrium (of magnitude and direction) with $\vec{H}_a$, as the adjacent flux line configuration is transformed by flux line cutting and migration. This conclusion is in accord with the observations of Cave [10], but sharply at odds with the picture recently put forward by Liu et al [38].

Chapter 6

INTERACTION OF TILTED FLUX LINES

6.1 Introduction

In chapters 4 and 5 we have investigated the evolution of configurations of initially parallel sheets of weakly or strongly pinned flux lines when they undergo rotation relative to a static magnetic field $\vec{H}_a$. The relative motion induces persistent currents to flow with a component directed along the flux lines. Flux cutting takes place when $j_{//}$ exceeds $j_{c//}$, allowing the flux lines to reorient, change their density and thus carve out the Boyer valley. In this chapter the behaviour when flux lines (of a fixed orientation) invade a lattice of parallel sheets of pinned flux lines directed at some chosen angle θ with respect to the invaders, is examined.

6.2 Framework of the Investigation

Sheets of parallel flux lines are trapped in a type II superconductor by subjecting it to a sweep of a magnetic field H_i which is then removed. To ensure that this cycle induces persistent currents to circulate in the same sense over the entire cross-section of the disk (hence that the magnetic density gradient is critical throughout the volume of the specimen), the excursion of H_i must exceed a threshold H_{sat} (discussed in chapter 3). Alternatively, the sample may be cooled from T_c to the ambient temperature in a magnetic field $H_i \geq H_{sat}$ which is then removed. In this work the first procedure was followed.

The procedures just described, magnetize the disk with a saturation residual moment, *i.e.* the specimen is permeated with the maximum amount of parallel flux lines it can hold in zero external magnetic field, by virtue of its pinning sites alone. The disk is rotated through a selected angle $0 < \theta < \pi$. In contrast to the situation encountered in chapter 4 where a static magnetic field was present during the disk rotation, in the circumstances now under consideration, there is no activity inside the specimen during the rotation since the external magnetic field is zero.

Once the disk has been rotated through a specified angle θ, a magnetic field $\vec{H}_a$ directed parallel to its flat surfaces is impressed. The application of $\vec{H}_a$ causes flux lines to nucleate and enter the disk, which is already filled by a lattice of parallel flux lines initially pointing at an angle θ relative to the invading flux lines. The disk and its content of magnetic flux, were rotated to achieve this objective. This situation enables the study of the phenomena occuring as a procession of flux lines of known orientation encroaches upon an array of flux lines, the two populations subtending an angle θ relative to each other. In this set up, the interaction between

the two sets of flux lines can easily be investigated over the entire range of θ between one extreme (where the two groups are parallel to each other) to the other limit (where they are anti-parallel).

The behaviour at the two extreme situations has been studied extensively. It is useful to describe the evolution of the $B(x)$ profiles which occur as $\vec{H}_a$ is applied. Figure 46 a) schematically displays the case where the new advancing flux lines are parallel to the existing population. An expanding T zone is generated comprising a region of compressed 'old' flux lines displaced by the invading 'new' flux lines. Eventually the entire volume is transformed into a T zone where the region of compressed 'old' flux lines diminishes but does not vanish.

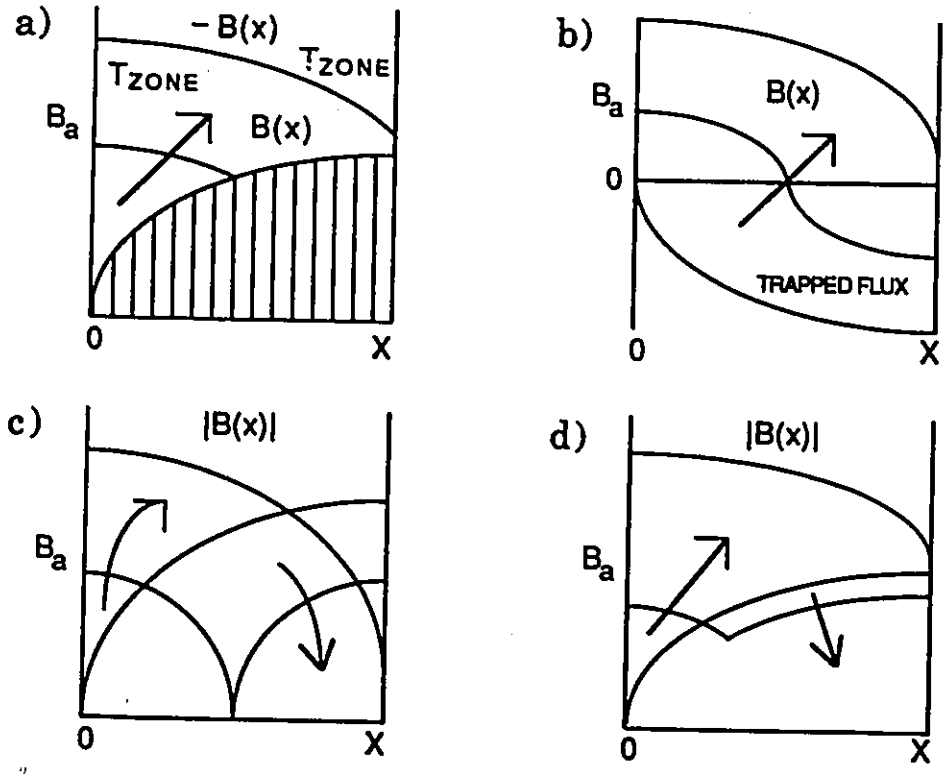

Figure 46: Flux line behaviour.

When the invading and invaded flux lines are anti parallel, the initial population is gradually decimated by flux annihilation which takes place at the migrating frontier between the two territories (see figures 46 b) and c)). The entire volume of the specimen exists as a T zone throughout this sequence of events.

For intermediate angles, the behaviour is considerably more complicated and requires the full force of Clem's general critical state phenomenological model for its description and analysis. Under these circumstances, CT as well as T zones develop when $\vec{H}_a$ is applied and pumps flux lines into the specimen which are tilted with respect to those already threading the disk. The delineation of the boundary between the CT and T zones and their progression as $\vec{H}_a$ is varied, are governed by the constraints of the model ($E_{//}j_{//} > 0$ and/or $E_{\perp}j_{\perp} > 0$).

A partial illustrative compilation of the behaviour observed in these situations on the *PbIn* and *PbBi* disks, is presented in this chapter. The results are confined to a display of typical data and some qualitative comments on a few salient features.

6.3 Comments on the Observations

As $\vec{H}_a$ is applied and subsequently cycled, the evolution of the magnetization both parallel and perpendicular to $\vec{H}_a$ (denoted as $< M_x >$ and $< M_y >$ respectively), are continuously monitored. Although measurements have been performed for several angles in the range $0 \leq \theta \leq \pi$, only data obtained when the trapped flux is orthogonal to the invading flux lines (*i.e.* $\theta = 90°$) is displayed. The behaviour of $< M_y >$ versus H_a is the choice of focus since the evolution of this component of the magnetization provides a direct witness on the fate of the trapped flux. Indeed, when $\theta = 90°$, $< M_y >$ and the trapped flux are initially identical.

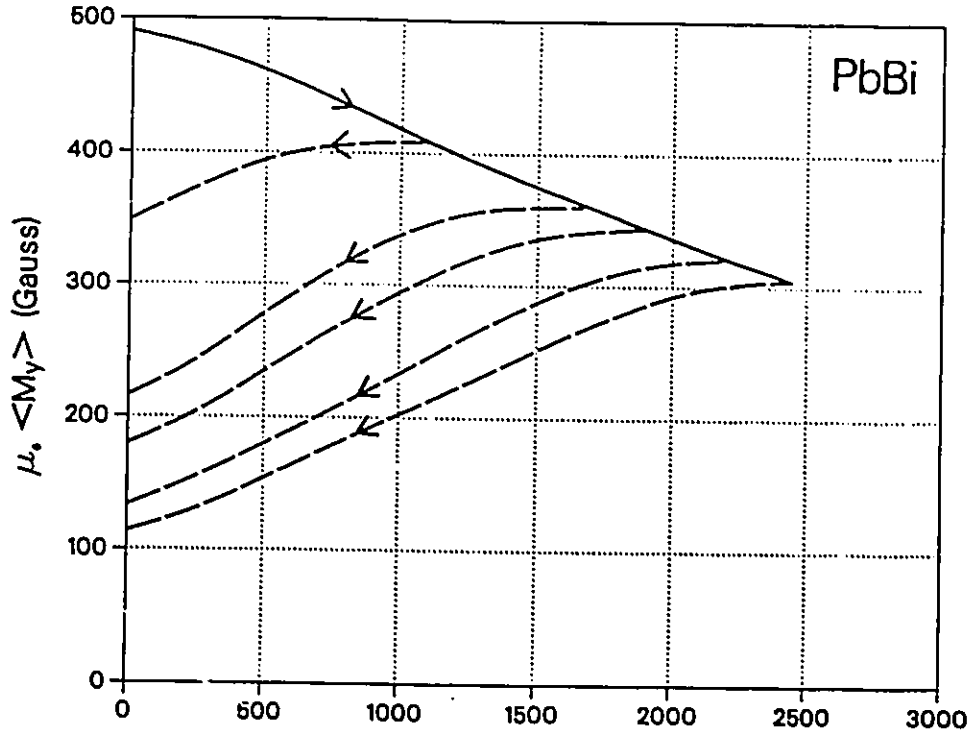

Figure 47: Trapped flux half cycle compilation curve for *PbBi*.

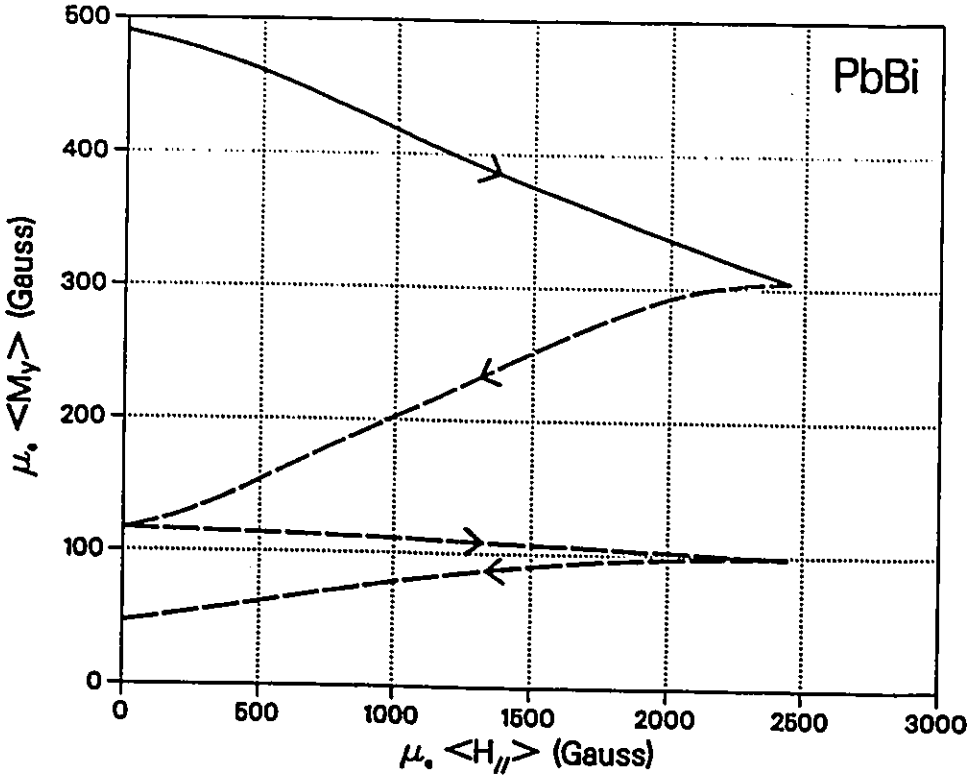

Figure 48: Selected individual case for *PbBi*.

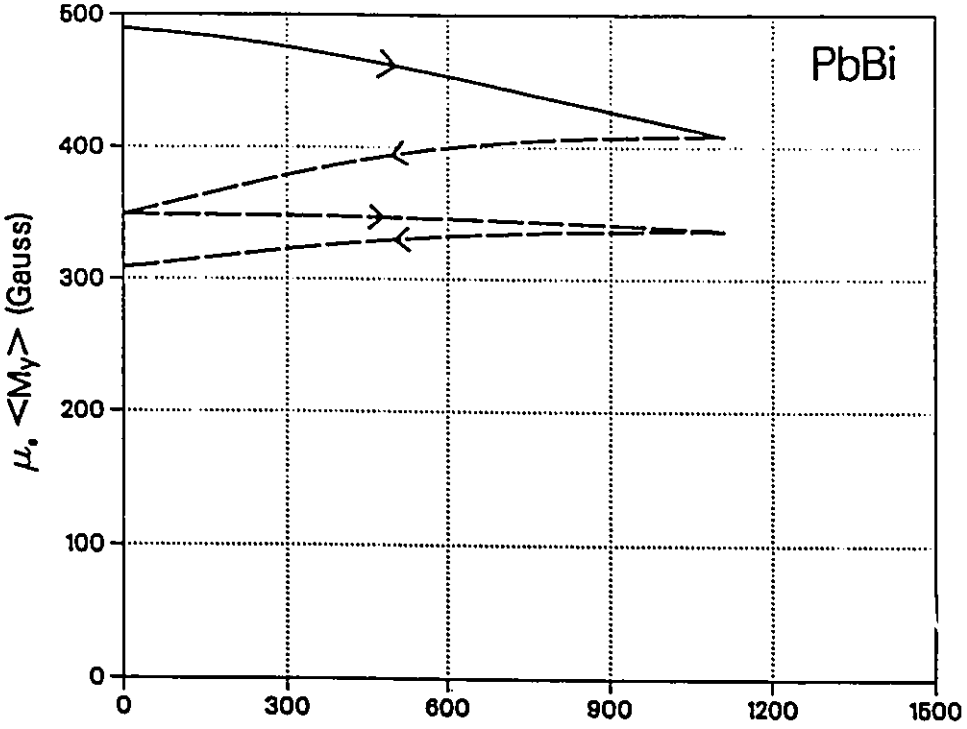

Figure 49: Selected individual case for *PbBi*.

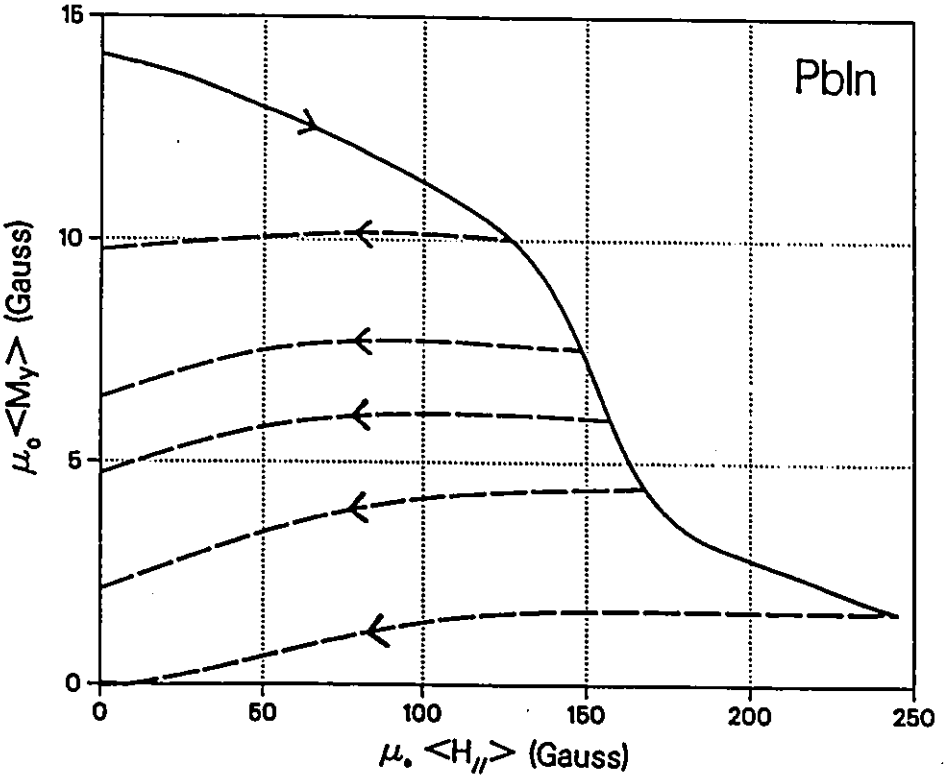

Figure 50: Trapped flux half cycle compilation curve for *PbIn*.

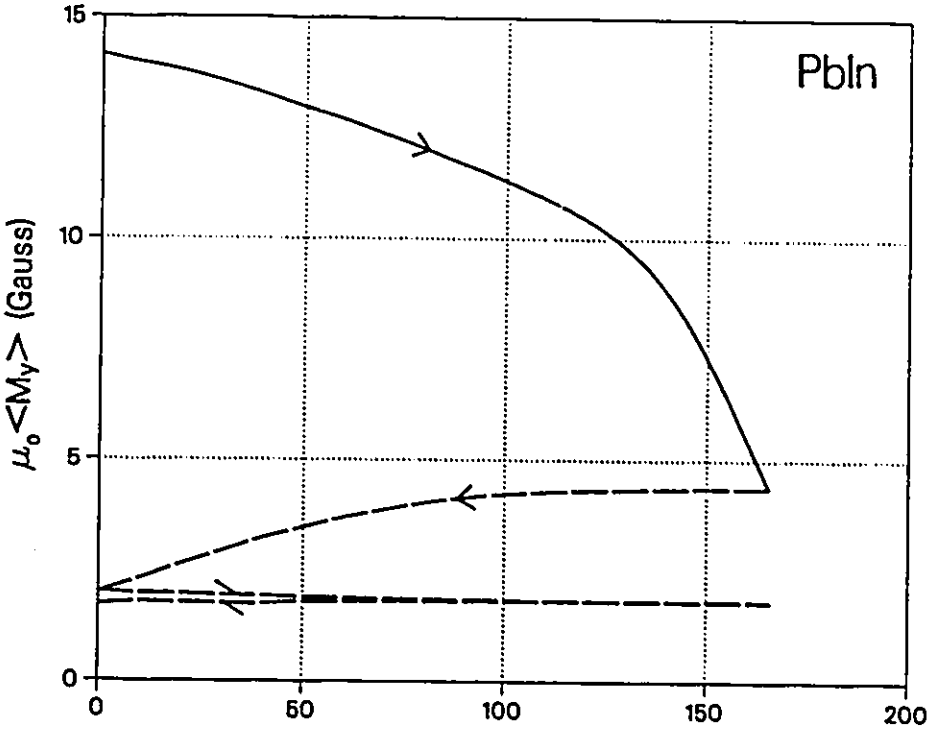

Figure 51: Selected individual case for *PbIn*.

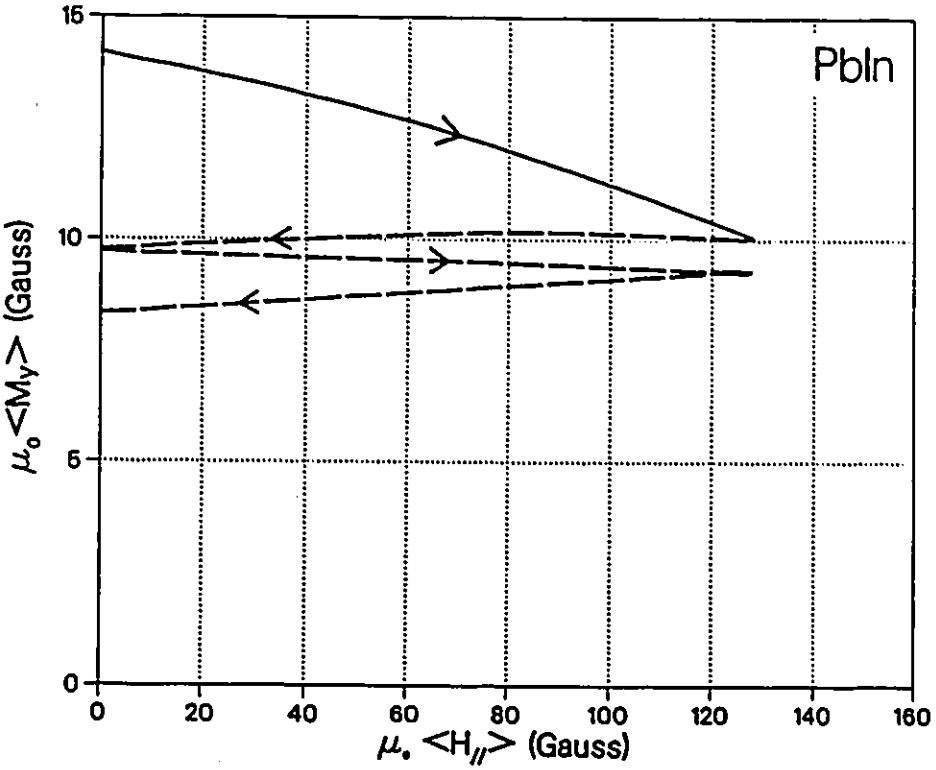

Figure 52: Selected individual case for *PbIn*.

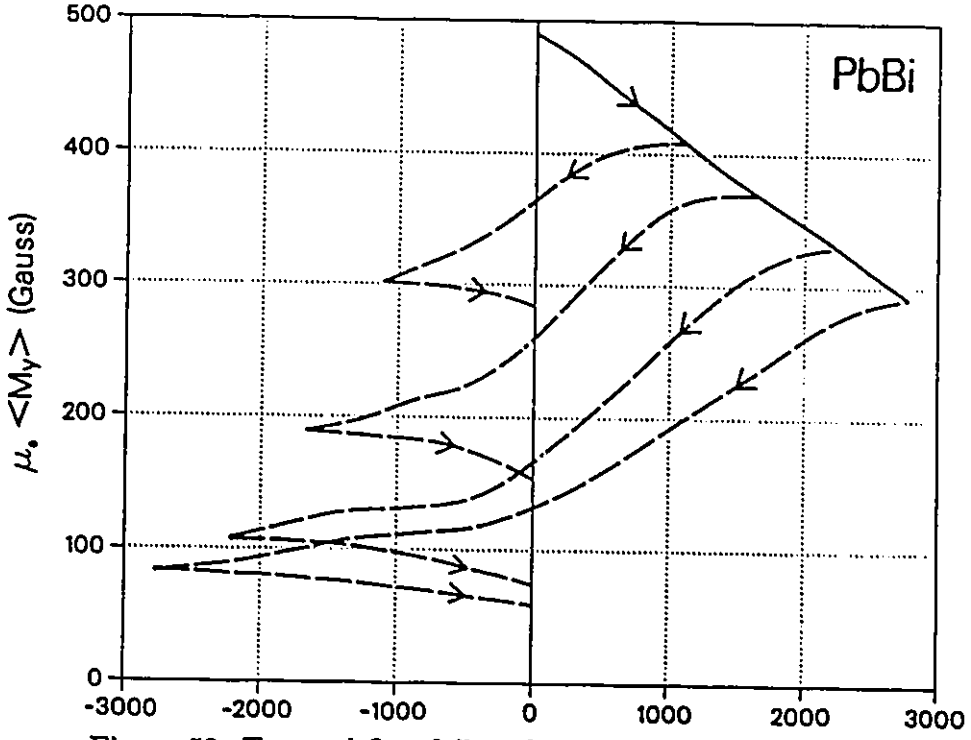

Figure 53: Trapped flux full cycle compilation curve for *PbBi*.

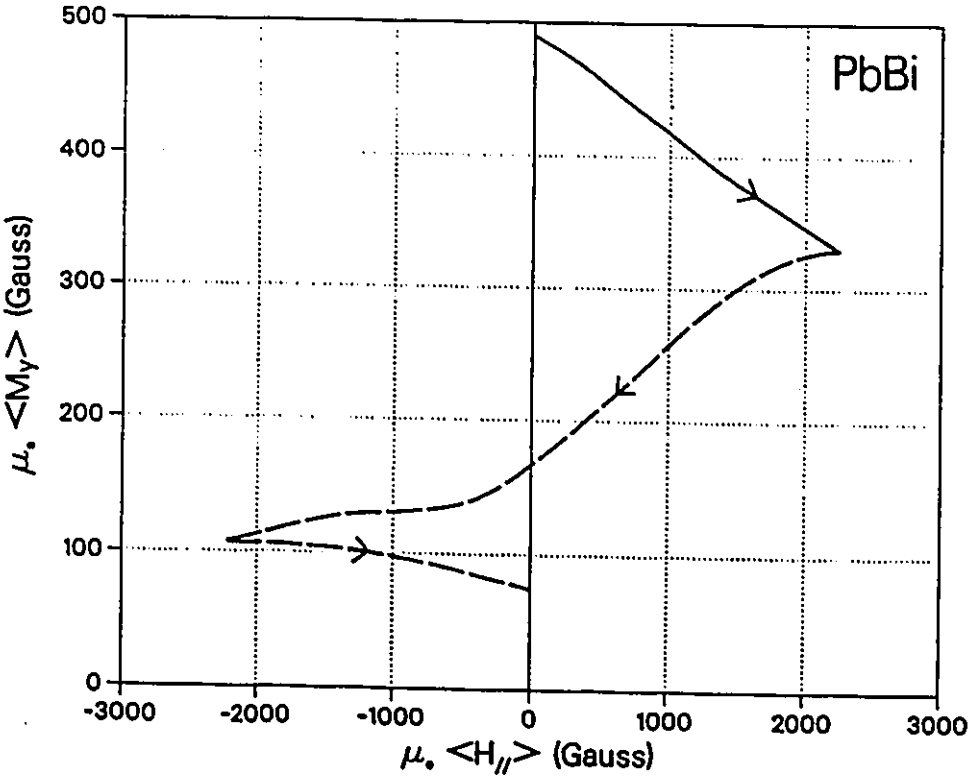

Figure 54: Selected individual case for *PbBi*.

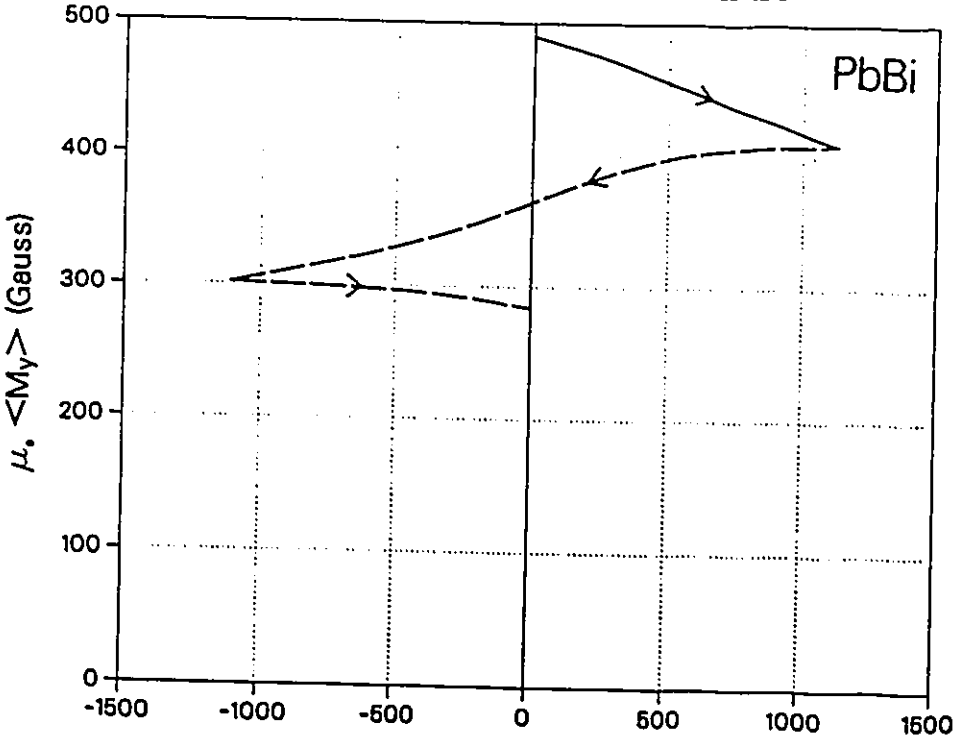

Figure 55: Selected individual case for *PbBi*.

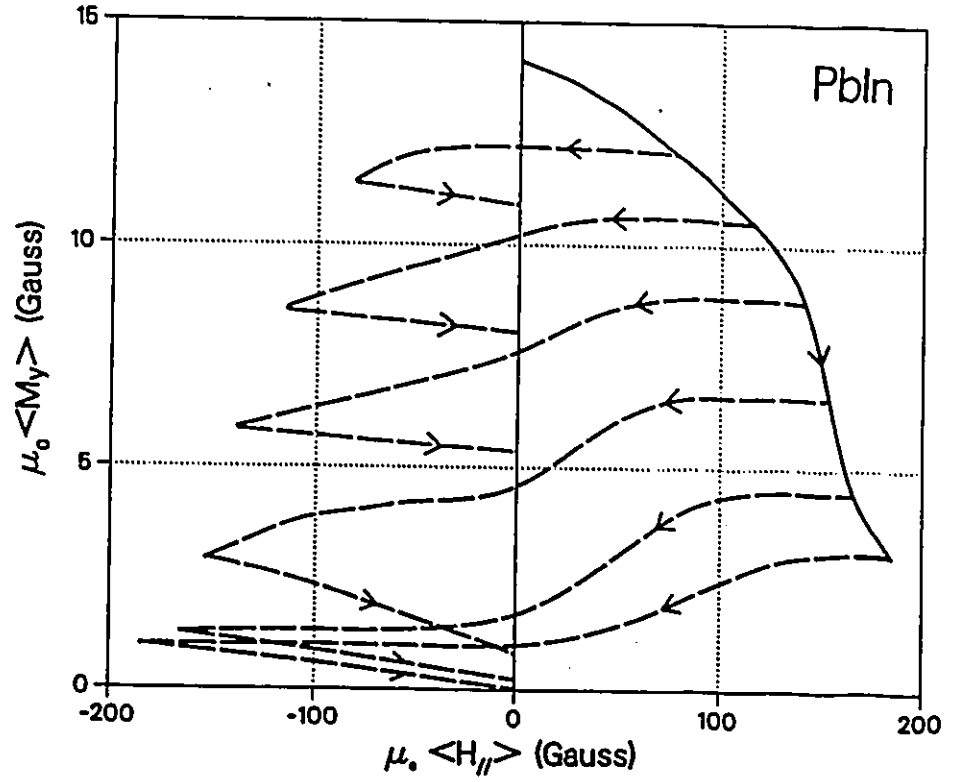

Figure 56: Trapped flux full cycle compilation curve for *PbIn*.

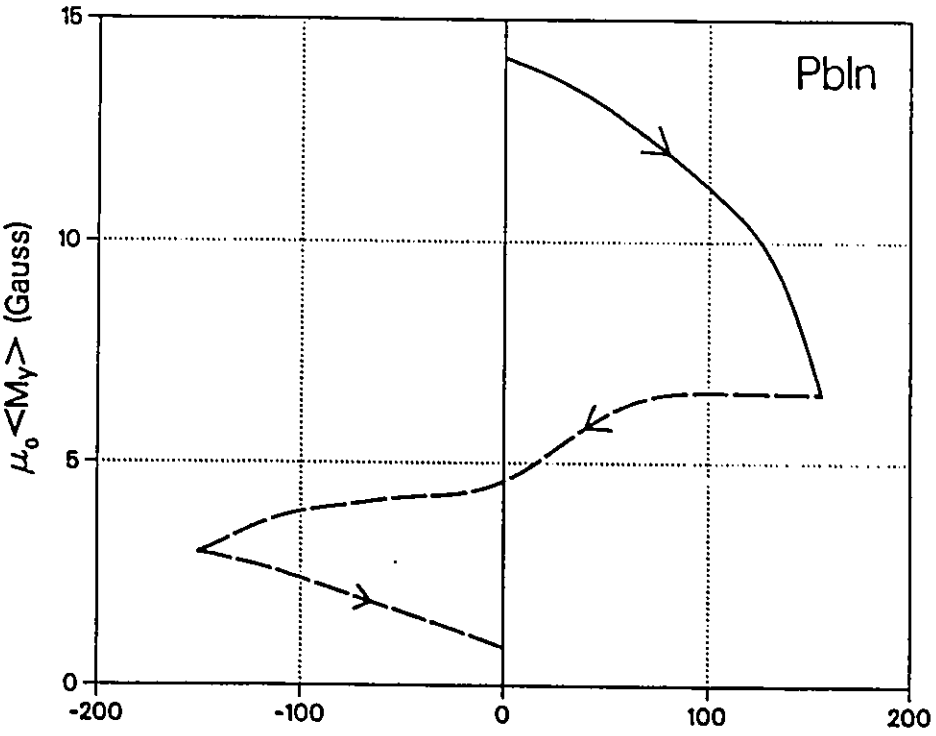

Figure 57: Selected individual case for *PbIn*.

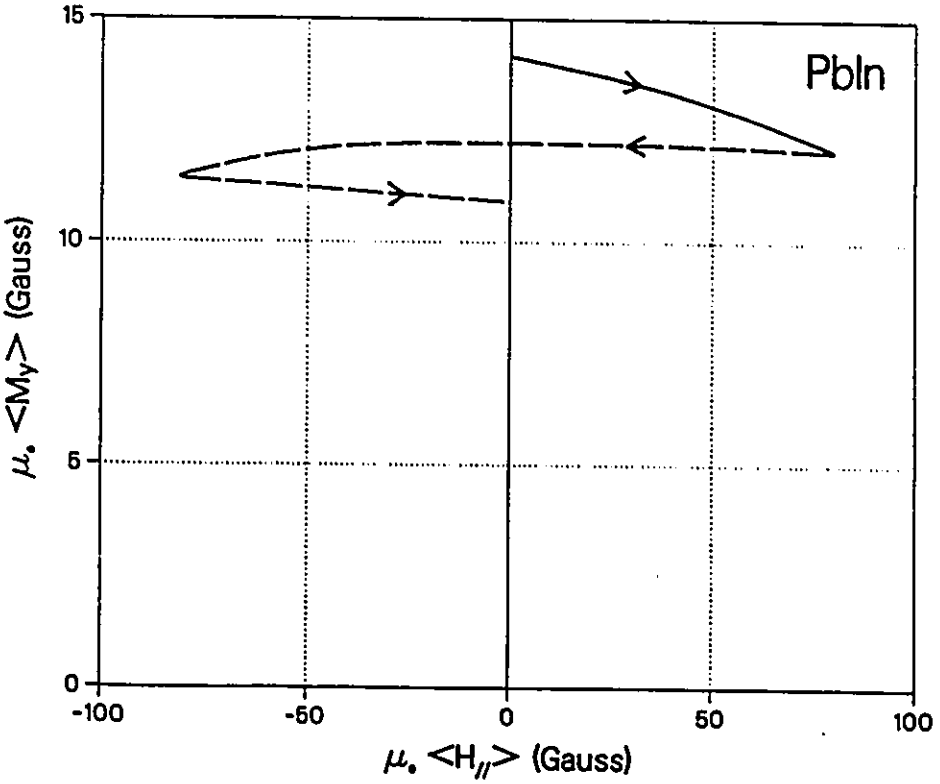

Figure 58: Selected individual case for *PbIn*.

A surprising feature is that an increase of H_a well beyond H_{**} is required in order that all vestiges of the trapped flux be eliminated. The observations of Lalonde on Nb indicate that a sweep of H_a up to H_{c2} is required to completely wipe out all traces of the trapped flux. In the context of the classical critical state picture, an increase of $H_a \geq H_{**}$ would be expected to suffice to erase the 'memory' of the trapped flux. It is noted that when $\theta = 180°$ an increase of $H_a = H_* < H_{**}$ accomplishes the total destruction of the trapped flux (see figure 46 b) and c)), while with $\theta = 0$ the envelope of the hysteresis curve is attained when $H_a = H_{*}$.

The trapped flux in the semi-reversible $PbIn$ sample shows a dramatic decline in the ranges $H_a \approx H_*$ or H_{**} (here H_* and H_{**} lie closer together) but subsequently the remaining trapped flux shows a very gradual diminution as H_a is increased further. By contrast, the trapped flux in the hysteretic $PbBi$, exhibits a very gradual decrease as H_a sweeps through H_* and H_{**}, and well beyond.

It is also of interest to follow the history of the remnants of the initial trapped flux as H_a is removed after a sweep to an arbitrary level above, or below H_*. The surprising feature here is that an appreciable change occurs in the configuration of the trapped flux as H_a traverses the final low range in its descent to zero, as witnessed by the substantial decrease in $< M_y >$ in this region. By contrast, $< M_y >$ stays nearly constant over the upper portion of the decrease in H_a. The opposite behaviour was expected in the classical perspective of persistent currents circulating in critical states and in the absence of flux cutting.

It is noteworthy that the configuration of the trapped flux continues to evolve when H_a is subsequently reapplied in the same direction as the initial cycle. Indeed each successive swing of H_a causes $< M_y >$ to diminish. The magnitude of each subsequent decrement in the series becomes smaller. The trends indicate that

eventually, a sufficiently large number of swings of H_a will cause $< M_y >$ to vanish. $< M_y > = 0$ is the only possible physical limit in these circumstances.

The novel feature is that instead of attaining a steady state or quasi steady state configuration after being subjected to the initial cycle, the response of the specimen containing trapped flux tilted at some angle $0 < \theta < 180°$ with respect to $\vec{H}_a$, exhibits aperiodic asymptotic behaviour. To the best of our knowledge, this is a rare, if not unique instance of such behaviour in type II superconductors. At the limits $\theta = 0$ and $\theta = \pi$, the response of the specimen is periodic after the initial cycle. Here however, $\vec{M} = < \vec{M}_z >$.

Once the novelty of the aperiodic behaviour is assimilated, it is then perhaps surprising to note that the size of the decrements in $< M_y >$ is dependent on *(i)* the amplitude of the swing of H_a, *(ii)* the magnitude of $< M_y >$ still remaining when a new cycle of H_a begins, and *(iii)* whether $\vec{H}_a$ changes polarity during a cycle or its sign is kept the same.

It is noted in chapter 5 that a simple empirical model provides a description of many intricate curves, which differ only slightly from those generated by the considerably more cumbersome (albeit correct) Clem phenomenological model. A serious attempt was made to exploit the empirical model to account for the observations described in this chapter. This model leads to a good description of the behaviour during the initial application of H_a and during the subsequent reduction of H_a to zero. This empirical model, however, fails to generate the subsequent aperiodic behaviour. The structure of the model in fact, leads to periodic responses. Lalonde [31] has shown that the Clem model produces the desired aperiodic behaviour. Our data, as well as his results, will be analyzed in his M.Sc. thesis.

Bibliography

[1] **P.W. Anderson and Y.B. Kim.** *Rev. Mod. Phys.*, **36**:39, (1964).

[2] **C.P. Bean.** *Rev. Mod. Phys.*, **36**:31, (1964).

[3] **C.P. Bean.** *Phys. Rev. Lett.*, 8:250, (1962).

[4] **M.G. Blamire and J.E. Evetts.** *Appl. Phys. Lett.*, **46**(12):1181–1183, (1985).

[5] **R. Boyer.** *PhD thesis, Physics Department, University of Ottawa*, (1977).

[6] **R. Boyer, G. Fillion and M.A.R. LeBlanc.** *J. Appl. Phys.*, **51**:1692–1701, (1980).

[7] **R. Boyer and M.A.R. LeBlanc.** *Sol. State Comm.*, 24:261, (1977).

[8] **E.H. Brandt, J.R. Clem, and D.J. Walmsley.** *Journal of Low Temperature Physics*, **37**:43–55, (1979).

[9] **A.M. Campbell and J.E. Evetts.** *Adv. Phys.*, **21**(1):199, (1972).

[10] **J.R. Cave and M.A.R. LeBlanc.** *J. Appl. Phys.*, **53**(3):1631–1648, (1982).

[11] **J.R. Cave and J.E.Evetts.** *Phil. Mag. B*, **37**(1):111–118, (1978).

[12] **J.R. Cave, J.E.Evetts, and A.M. Campbell.** *Journal de Physique (Colloque)*, 39(C6):614–616, (1978).

[13] **J.R. Clem.** *Physical Review*, 26(5):2463–2473, (1982).

[14] **J.R. Clem.** *Journal of Low Temperature Physics*, 38(3/4) :353–369, (1980).

[15] **J.R. Clem.** *Physica*, **107(B)**:453–454, (1981).,

[16] **J.R. Clem and A. Perez-Gonzalez.** *Proceedings of the International Symposium on Flux Pinning and Electromagnetic Properties of Superconductors*, 196-200, (1985).

[17] **J.R. Clem and S. Yeh.** *Journal of Low Temperature Physics*, **39**:173–189, (1980).

[18] **G.W. Cullen and G.D. Cody.** *J. Appl. Phys.*, 44:2838, (1973).

[19] **W.A. Fietz, M.R. Beasley, J. Silcox and W.W. Webb.** *Physical Review*, **136**(2A):A335–A345, (1964).

[20] **G. Fillion.** *PhD thesis, Physics Department, University of Ottawa*, (1986).

[21] **G. Fillion, R. Gauthier and M.A.R. LeBlanc** *Phys. Rev. Lett.*, **43**:86, (1979).

[22] **G. Gandolfini.** *MSc thesis, Physics Department, University of Ottawa*, (1989).

[23] **G. Gandolfini, M.A.R. LeBlanc and J. Sekerka.** *Cryogenics*, **29**(3A):373–378. (1989).

[24] **A. Golebiowski.** *MSc thesis, Physics Department, University of Ottawa,* (1988).

[25] **J.W. Heaton and A.C. Rose-Innes.** *Phys. Lett.*, 9:112, (1964).

[26] **J.W. Heaton and A.C. Rose-Innes.** *Cryogenics.*, 4:85, (1964).

[27] **V.R. Karasik and V.G. Vereschagin.** *Soviet Phys. JETP.*, 32:20, (1971).

[28] **Y.B. Kim, C.F. Hempstead and A.R. Strnad.** *Physical Review,* 129:528, (1963).

[29] **Y.B. Kim, C.F. Hempstead and A.R. Strnad.** *Physical Review,* 131:2486, (1963).

[30] **Y.B. Kim, C.F. Hempstead and A.R. Strnad.** *Physical Review,* (A)139:1163, (1965).

[31] **R. Lalonde, J. Sekerka and M.A.R. LeBlanc.** *Japanese J. Appl. Phys.*, 26:1507–1508, (1987).

[32] **M.A.R. LeBlanc.** *Physical Review*, 143:220–223, (1966).

[33] **M.A.R. LeBlanc, B.C. Belanger and R.M Fielding.** *Phys. Rev. Lett.*, 14:704, (1965).

[34] **M.A.R. LeBlanc and C.T.M. Chang.** *Sol. State Comm.*, 6:679–683, (1968).

[35] **M.A.R. LeBlanc, G. Fillion, and A. Golebiowski.** *Japanese J. Appl. Phys.*, 26:1509–1510, (1987).

[36] **M.A.R. LeBlanc, G. Fillion, W.E. Timms, A. Zahradnitsky, and J.R. Cave.** *Cryogenics*, 26:491–500, (1981).

[37] **M.A.R. LeBlanc, and J.P. Lorrain.** *J. Appl. Phys.*, 55:4035–4051, (1984).

[38] **L. Liu, J.S. Kouvel and T.O. Brun** *Physical Review B*, 38:11799–11801, (1988).

[39] **H. London.** *Phys. Lett.*, 6:162, (1963).

[40] **J.P. Lorrain, M.A.R. LeBlanc and A. Lachaine.** *Can. J. Phys.*, 57:1458–1477, (1979).

[41] **T.Matsushita.** *Physical Review B.,*, 38:820–824, (1988).

[42] **J.E. Nicholson and P.T. Sikora.** *J. Low Temp. Phys.*, 17:275, (1974).

[43] **A. Perez-Gonzalez and J.R. Clem.** *Physical Review B*, 31 (11):7048–7058, (1985).

[44] **A. Perez-Gonzalez and J.R. Clem.** *Physical Review B*, 32 (5):2909–2914, (1985).

[45] **A. Perez-Gonzalez and J.R. Clem.** *J. Appl. Phys.*, 58 (11) :4326–4335, (1985).

[46] **S.T. Sekula, R.W. Boom and C.J. Bergeron Jr.** *Appl. Phys. Lett.*, 2 :102, (1963).

[47] **W.E. Timms and M.A.R. LeBlanc.** *J. Phys. F: Metal Phys.*, 4 :136–153, (1974).

[48] **W.E. Timms and D.G. Wamsley.** *J. Phys.* F(5) :287, (1975).

[49] **W.E. Timms and D.G. Wamsley.** *J. Phys.* **F(6)** :2107, (1976).

[50] **D.J. Walmsley.** *J. Phys.*, **F(2)**:510-528, (1972).

[51] **D.J. Walmsley and W.E. Timms.** *J. Phys.*, **F(7)**:2373, (1977).

[52] **Y. Wolfus, Y. Yeshurun and I. Felner.** *Physical Review*, **B(37)**:3667-3670, (1988).